UC Berkeley
UC Berkeley Electronic Theses and Dissertations

Title
Anisotropies in discrete DNA-assembled gold nanoparticle structures

Permalink
https://escholarship.org/uc/item/5jg4x119

Author
Smith, Jessica Marie

Publication Date
2014

Peer reviewed|Thesis/dissertation

eScholarship.org Powered by the California Digital Library
University of California

Anisotropies in discrete DNA-assembled gold nanoparticle structures

by

Jessica Marie Smith

A dissertation submitted in partial satisfaction of the

requirements for the degree of

Doctor of Philosophy

in

Chemistry

in the

Graduate Division

of the

University of California, Berkeley

Committee in charge:

Professor A. Paul Alivisatos, Chair
Professor Matthew B. Francis
Professor Eva Nogales

Spring 2014

Anisotropies in discrete DNA-assembled gold nanoparticle structures

Copyright 2014

by

Jessica Marie Smith

Abstract

Anisotropies in discrete DNA-assembled gold nanoparticle structures

by

Jessica Marie Smith

Doctor of Philosophy in Chemistry

University of California, Berkeley

Professor A. Paul Alivisatos, Chair

Plasmon rulers consisting of optically coupled metal nanoparticles linked by biological macromolecules have provided a tool for bio-imaging and enzymology that is non-bleaching, non-blinking, and biocompatible. A pair of plasmonic nanoparticles couple when they are in spatial proximity, resulting in spectral shifts and increased scattering intensity. Previous research has developed synthetic techniques for precisely assembling gold nanoparticles using DNA. Two self-assembled plasmonic nanoparticles have been shown to be an enzyme-responsive material in one-dimension. In order to visualize the subtle conformational changes ubiquitous in biological systems, three-dimensional, anisotropic nanoparticle assemblies are required.

This dissertation reports two examples of next-generation plasmon rulers. DNA-assembled dimers of gold nanorods can act as a three-dimensional plasmon ruler only if the relative orientation of the particles can be controlled. By tuning the conditions of electrophoretic separation and the DNA structure, a sample of gold nanorod dimers that are attached side-by-side can be isolated from those attached end-to-end. TEM characterization of these oriented dimers shows a statistically significant deviation from randomly oriented nanorod pairs. Because of the high yield of oriented nanorod pairs, this colloidal sample can serve as an ensemble biosensor.

A three-dimensional plasmon ruler can also be synthesized by increasing the complexity of the underlying DNA structure. Four DNA strands, each attached to a gold nanoparticle, hybridize such that each strand folds into one face of a chiral pyramid. The sequence of the four strands was designed to maximize the yield of one enantiomer based on tertiary

structure of the double helices. This structure is a circular dichroism-based nanoparticle ruler for subtle biological events, such as the extension of DNA by a DNA-binding protein.

Additionally, the DNA-assembled gold nanoparticle system was characterized by state-of-the-art electron microscopy. A method called individual particle electron tomography can be used to image single macromolecules. By tuning the parameters of the negative stain, the transmission electron microscope (TEM), and the buffer conditions, this method has been extended for the reconstruction of a 3D density map of an individual DNA double helix labeled by two nanoparticles. Previous work on cryo-EM imaging of DNA nanostructures without gold nanoparticles has relied on averaging many images together to create a composite density map. This work represents an electron microscopy constructed density map of a DNA double helix.

Liquid-phase TEM can probe and visualize dynamic events with structural or functional details at the nanoscale in a liquid medium. The grapheme liquid cell was adopted to seal an aqueous sample solution containing DNA-assembled gold nanoparticle dimers against the high vacuum in TEM. Quantitative analysis of collected real time nanocrystal trajectories reveals the fidelity of the DNA in the presence of the electron beam as well as the reconstruction of the 3D configuration and motion of the nanostructure.

In memory of my father.

Contents

Contents **ii**

List of Figures **iv**

1 Introduction **1**

2 Synthesis and characterization of nanocrystal molecules **7**
2.1 Nanocrystal synthesis and bioconjugation 7
2.2 Separation and assembly of DNA-nanoparticle conjugates 11
2.3 Optical properties of metal nanoparticles 14

3 Controlling the orientation of DNA-assembled gold nanorods **20**
3.1 Introduction 20
3.2 Gold nanorod synthesis and assembly 22
3.3 Results and discussion 25
3.4 Conclusions 30

4 Symmetry breaking in chiral plasmonic nanocrystal assemblies **31**
4.1 Introduction 31
4.2 Design of chiral assemblies based on symmetry breaking 32
4.3 Synthesis and characterization of pyramids 41
4.4 Conclusions 44

5 Electron microscopy of DNA-assembled gold nanoparticle dimers **45**
5.1 Synthesis of gold nanoparticle dimers 46
5.2 In Situ graphene liquid cell 48
5.3 Electron tomography of single 84bp DNA 57

6 Conclusions **61**

References **62**

A Gold nanoparticle synthesis **75**

B Gold nanorod synthesis **78**

C DNA conjugation **81**

List of Figures

1.1 Relative sizes of micro- and nanoscale objects 1
1.2 Scheme of discrete DNA-nanocrystal molecules and part of an DNA-nanoparticle extended solid 3

2.1 Reaction of gold ions to produce gold nanoparticles 8
2.2 Scheme of seeded synthesis of gold nanorods 9
2.3 Reaction of thiolated DNA with gold nanoparticles 10
2.4 An example chromatogram. 13
2.5 Electrons oscillate in response to resonant light. 15
2.6 Extinction of various sizes of gold nanoparticles. 17
2.7 Circular dichroism of double stranded DNA 19

3.1 Nanorods synthesis shows monodisperse particles that show and longitudinal and transverse plasmon by UV-visible spectroscopy. 22
3.2 After CTAB is removed, particles are stabilized by BSPP. 23
3.3 HPLC of gold nanorods conjugated to DNA. 24
3.4 Nanorod dimers can be separated by gel electrophoresis. 26
3.5 TEMs of DNA-assembled gold nanorods 27
3.6 Scheme of DNA-assembled gold nanorods in agarose gel 28
3.7 Emsemble UV-vis of gold nanorod dimers 29

4.1 Substitutional (left) versus configurational (right) asymmetry in nanoparticle assemblies. 33
4.2 Scheme of symmetry breaking in pyramid structure 34
4.3 Extinction of pyramid calculated with circularly polarized light. 35
4.4 Circular dichroism spectra with increasing length of the symmetry-breaking arm. 38
4.5 Frequency of the positive and negative CD band changes with the length of the symmetry-breaking arm 39
4.6 Calculations of CD spectra with imperfect fabrication 40
4.7 Calculations of more complex pyramids with tunable chirality based on symmetry breaking 41
4.8 Agarose gel electrophoresis and TEM of dimers of 10nm and 20nm particles . . 42

4.9 Measured CD spectrum of pyramids including one shortened edge. TEMs show 2D projections of 3D structures. 43

5.1 Anion-exchange HPLC allows baseline separation of bare gold nanoparticles from those conjugated to a single strand of DNA. 47
5.2 Gold nanoparticle dimers can be separated from reaction products by gel electrophoresis. 48
5.3 Graphene liquid cell imaging of Au nanocrystal-dsDNA nanoconjugates 50
5.4 A collection of Au nanocrystal trajectories in the same liquid pocket 52
5.5 Diffusional statistics of Au-single strand DNA and Au-42 bp dsDNA trajectories 53
5.6 The 3D configuration and motion of a trimer 55
5.7 The iterative construction for the trimer 56
5.8 Electron micrographs of a number of DNA-nanoparticle conformations revealed by optimized negative stain. 58
5.9 An individual DNA-NG complex was imaged by OpNS-ET 60

Acknowledgments

I would neither have pursued science nor attended graduate school without the serendipitous intervention of several key figures in my life. I'm grateful to Prof. Mary Lidstrom and Dr. Janiece Hope for providing an opportunity for me to experience laboratory research at the University of Washington as a high school student. In addition to supervising my undergraduate research efforts, Prof. Beth Traxler and Prof. David Ginger provided me with different but equally valuable philosophies on the research endeavor.

My tenure in the Alivisatos lab has been rewarding and character-building. The global view of science that my advisor, Prof. Paul Alivisatos, allows his students to access is truly singular. Many lab members aided my progress, among them Dr. Alex Mastroianni, Dr. Sassan Sheikholeslami, Prof. Young-wook Jun, Prof. Prashant Jain, Dr. Charina Choi, Andrew Olson, Dr. Trevor Ewers, Dr. Katie Lutker, Prof. Somin Lee, Dr. Qian Chen, Dr. Jungwon Park and a special thanks to Prof. Vivian Ferry for her encouragement and friendship. My collaborators Dr. Gang Ren and Dr. Lei Zhang fearlessly attempted an experiment at my suggestion. My undergraduate students, Leslie Hamachi and Sarah Hull, renewed my excitement for science daily.

This document is a capstone of many years of education inside and outside of the classroom. For providing such a solid foundation I would like to thank all of the teachers at Assumption-St. Bridget School and Bishop Blanchet High School in Seattle, WA. I would also like to acknowledge Prof. Sarah Keller, Prof. Kenneth Clatterbaugh, and Prof. James Mayer at the University of Washington and Prof. Phil Geissler, Prof. Matthew Francis, Prof. Ron Cohen, Prof. Robert Harris, Prof. Jan Liphardt and Prof. Eva Nogales at UC Berkeley for their contributions to my research and education.

My friends and family are my light. Zoey Herm was my rock throughout graduate school and Karina Collins has been my rock throughout our lifelong friendship. Vanessa Palmer, Eric Sundstrom, Erica Shultz, and Stephen Elkind helped me find the fun in my studies. Thanks to my mother for being a fantastic role model and relentless supporter, my father for loving me and believing in me as long as he could, and my brother for challenging me and for his friendship.

Chapter 1

Introduction

Noble metal nanoparticles conjugated to biomolecules have increased spacial-temporal resolution in biological imaging of cells and tissues, improved sensitivity of biosensors, and exemplified a novel class of materials for diagnostics and therapeutics. These applications exploit the unique optical properties of metal nanoparticles. Conduction electrons, when confined to the surface of a nanoparticle smaller than the wavelength of visible light, oscillate coherently inducing a surface plasmon. The nanoparticle surface plasmon couples strongly to incident light inducing strong absorption, scattering, and local electric fields [1].

The frequency of the surface plasmon resonance can be tuned by changing the size, shape, aspect ratio, material, or surrounding dielectric (refractive index) of the nanoparticle. For

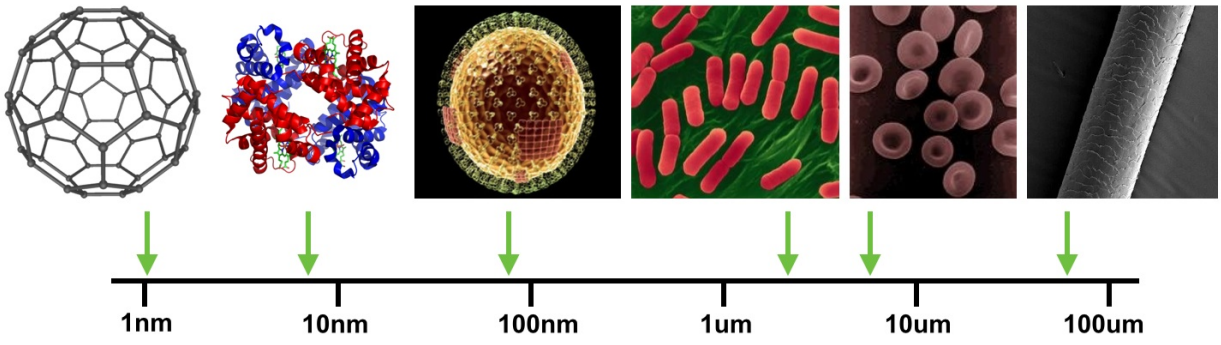

Figure 1.1: Relative sizes of micro- and nanoscale objects. Nanoscale materials (those with a dimension of 1-100nm), have unique, size-dependent optical, electronic, and catalytic properties. Gold nanoparticles can be synthesized to a variety of diameters across the nanoscale. DNA, with a diameter of roughly 2nm and pitch of 1nm per three base pairs, is suitable for organizing these materials on the nanoscale.

example, small spherical gold nanoparticles absorb and scatter light around 520nm while small silver particles are resonant at 400nm. Additionally, bringing metal nanoparticles in close proximity induces complex optical resonances. Many of these properties can be modeled using Mie theory [2] or a finite element method such as finite-difference time-domain (FDTD) [3] or discrete dipole approximation [4].

Metal nanoparticles of different sizes and morphologies can be chemically synthesized [5–7]. In the simplest case, gold nanospheres are formed when gold salt is quickly reduced in a vigorously stirred aqueous solution. The quality of nanoparticles can be improved by carefully controlling the temperature, pH and surface ligands present in the reaction. Anisotropic particles are generally formed by synthesizing a small (∼3-4nm) seed particle which is introduced to a growth solution containing additional metal salt, a slow reducing agent, and a structure-directing ligand [8].

These particles can be conjugated to short strands of DNA to create discrete artificial molecules [9] or extended solids [10]. DNA has proven to be useful to organize nanoparticles because it can be designed to fold into structures with nanoscale precision. Myriad tools exist in the molecular biology community for the design of nucleic acids and their rapid synthesis and modification. These tools have been adopted by the DNA nanotechnology community to utilize the base-pairing properties of DNA creating designed DNA structures to organize nanoparticles. Because metal nanoparticles optically couple when in proximity to one another, DNA nanotechnology which arranges metal nanoparticles can induce complex resonances for imaging, biosensing, and solution phase metamaterials [11]. Recently, anisotropic particles, such as nanorods and triangular nanoprisms, have been incorporated into these structures [12, 13].

Previous work in the Alivisatos group has demonstrated that metal nanoparticles linked by DNA can act as a biosensor. Gold and silver particles coupled by single-stranded DNA were observed by single particle darkfield microscopy [14]. The scattering intensity maximum single nanoparticles was shown to red-shift when an additional particle was connected via DNA. Further research showed that gold nanoparticles connected by double stranded DNA could serve as a sensor for a DNA-restriction enzyme [15]. Large gold nanoparticles connected by DNA containing a restriction site were immobilized in a flow cell; when EcoRV was introduced, the maximum scattering frequency of the dimers red-shifted as the particles were brought in close proximity. The EcoRV cofactor Mg^{2+} allowed the restriction enzyme to complete it's reaction, resulting a blue-shift as the particles decoupled. The plasmon ruler was used first in vivo when proteins were conjugated to metal nanoparticles [16]. Single capsace-3 cleavage events were observed in cells as the intensity of a plasmon ruler decreased, stepwise, over time.

Though these plasmon rulers allow for high spacial resolution of measuring biological events in one dimension over time, most complex phenomena involve relative movements in

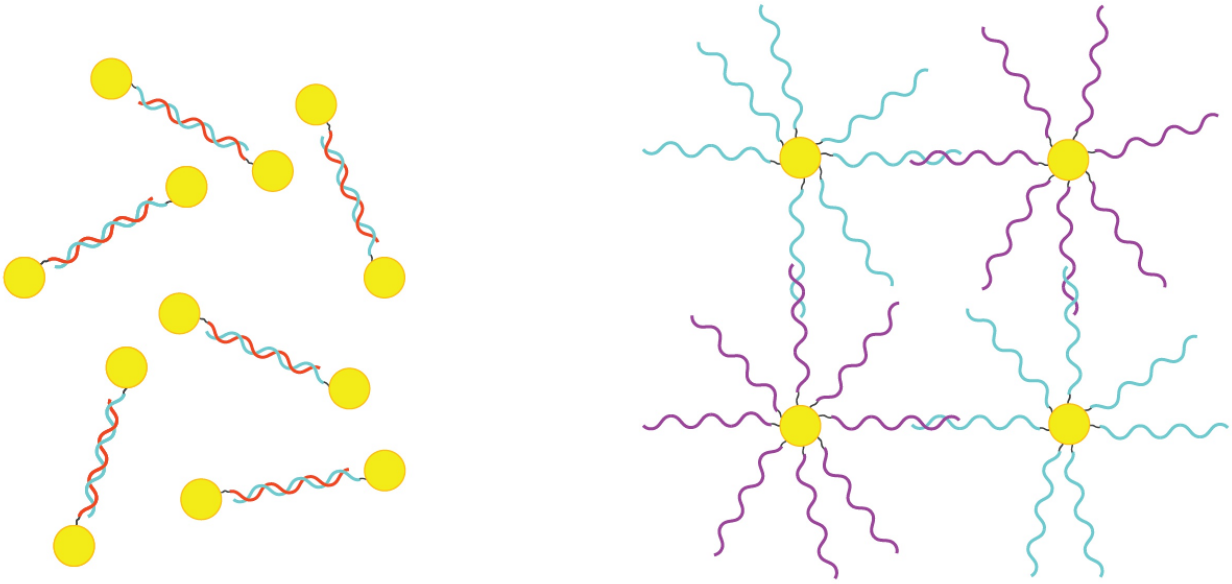

Figure 1.2: Scheme of discrete DNA-nanocrystal molecules (left) and part of an DNA-nanoparticle extended solid (right). Metal nanoparticles conjugated to one DNA strand can be coupled by complementary DNA strands to create DNA-assembled nanoparticle dimers. Similar particles conjugated to many strands will form a crystal structure.

three dimensions. A three-dimensional plasmon ruler was theorized based on pairs of plasmonic nanorods that exhibits sensitive spectral signatures in response to three-dimensional displacements [17]. In this ruler, a fifth nano rod breaks the symmetry between two pairs of stacked nanorods, creating narrow spectral resonances with tunable intensity and color. Typical plasmonic nanoparticles have broad resonances due to radiative coupling to incident light. The design presented here takes advantage of the quadrupolar resonances of dimers of nanorods to create a narrow resonance. As the position of the single nanorod changes, both laterally and vertically, the intensity and color of these two resonances shifts significantly. The specificity of this spectral response can be used to determine the three-dimensional position of the single nanorod. Additional conformational motions such as twisting and tilting also produce unique spectral signatures. These assemblies were designed theoretically using a finite element electrodynamic software package then fabricated using electron-beam lithography as a proof-of-concept construction.

To implement a three-dimensional plasmon ruler in a biological system, these complex resonances must be accessed using solution-phase nanoparticles and responsive, biocompatible materials. To that end, the research in this dissertation describes the synthesis and characterization of next-generation plasmon rulers creating by incorporating anisotropies

into DNA-assembled nanoparticle structures.

Most closely mimicking the theorized three-dimensional plasmon ruler, gold nanorods were arranged by DNA. Gold nanorods can be colloidally synthesized in high yield with different aspect ratios according to literature protocols. Controlling the sequence of DNA and tuning their can control the attachment and orientation of nanorods. As a preliminary step toward creating 3D plasmon rulers, DNA-assembled nanorod dimers have been synthesized in high yield. To functionalize these particles with DNA we must first exchange their surface ligands. Exchanging the bilayer ligand shell that?s left on the nanoparticle after synthesis is a necessary step towards allowing the thiol-functionalized DNA to attach to the particle surface. Emulsifying the positively charged, CTAB-coated nanorods in the presence of a negatively charged phosphine ligand modifies the surface chemistry sufficiently to allow thiolated oligonucleotides to attach to the surface. Before assembling gold nanorods into discrete structures, the nanorod-DNA conjugates are separated based on the number of attached oligonucleotides. Anion-exchnage high-performance liquid chromatography has allowed us to separate the nanorods by DNA valency. In the simplest case, the complementary separation products can be combined to create nanorods dimers. These dimers have been visualized by TEM and shown to optically couple in ensemble visible spectroscopy. Synthesizing DNA-assembled nanorod dimers in solution in high yield represents a first step toward the realization of a 3D plasmon ruler. This assembly is also unique among other reports of assembly of nanorods in that it allows for measurements of dynamic behavior based on the DNA connecting the two rods.

Anisotropies can be introduced into an artificial molecule containing only spherical nanoparticles by designing an asymmetric DNA structure. A second three-dimensional plasmon ruler is a stimuli-responsive chiral DNA-mediated nanoparticle assembly based on circular dichroism (CD) detection. This structure exhibits a sensitive optical response and provides a unique substrate for detecting handedness in biological events. A coupled dipole model to calculate the optical response of metal nanoparticle assemblies which takes into account parameters such as the polydispersity of colloidally synthesized nanoparticles and the flexibility of DNA was used to design a four nanoparticle asymmetric pyramidal structure. Four DNA strands, each attached to a gold nanoparticle, hybridize such that each strand folds into one face of the pyramid. The sequence of the four strands was designed to maximize the yield of one enantiomer based on tertiary structure of the double helices and to minimize thermodynamically favorable alternate structures. Taking into account design rules from the model and the constraints of our DNA template, we synthesized a distorted DNA tetrahedron of side length 26 base pairs (∼9nm), save one side, of 16 base pairs (∼5.5nm), decorated with two 10 nm and two 20 nm diameter gold nanoparticles. The shorter side breaks the mirror plane between the two sizes of nanoparticles, forming a chiral assembly. This structure can be synthesized in high yield in aqueous solution. Colloidal nanoparticles of 10 and 20 nm are reacted with 5' thiol modified oligonucleotides in a buffered solution of moderate ionic strength. Anion exchange high-performance liquid chromatography separates the mixture of

products to produce monoconjugated nanoparticles for assembly. Ensemble circular dichroism measurements show a bisignate feature near 520 nm, the absorbance maximum of gold nanoparticles. Calculations show that small changes in the length of the shorter, symmetry breaking arm of the DNA tetrahedron will change the intensity and spectral position of the CD. Our structure will find application as a nanoparticle ruler for subtle biological events, such as the extension of DNA by a DNA binding protein. Large changes in length of this arm can invert the handedness of the chiral structure completely, and therefore the sign of the bisignate curve. Thus, in addition to biomolecular recognition, this chiral nanoassembly represents the first of a category of switchable metamaterials which can change handedness as a response to external stimuli.

Characterizing three-dimensional DNA-nanoparticle structures by TEM involves visualizing a two-dimensional projection created by drying the substrate. To more accurately characterize DNA-nanoparticle structures, the final research described in this dissertation involves applying new methods in electron microscopy.

Imaging a single biomolecule, such as a protein or DNA double helix, has long been a goal of electron microscopy researchers. Typical cryo-EM density maps of biomolecules require hundreds or thousands of images to be averaged. Recently research [18] has combined cryo-EM, negative staining, and EM tomography to report the first example of an electron micrograph of a single protein. While their techniques work well for molecules like globular proteins, imaging a molecule such as a DNA double helix with a width below 2nm is beyond the resolution limit. Gold nanoparticle dimers attached with double stranded DNA are ideal substrate for the IPET method. Due to the atomic mass of gold, these nanoparticles are high contrast under TEM. Because the DNA double helix is synthesized with gold nanoparticles on either end, the DNA can be negative-stained and located on TEM. By tuning the parameters of the stain, the TEM, and the buffer conditions, we will be able to reconstruct a 3D density map of one DNA double helix. Previous work on cryo-EM imaging of DNA nanostructures without gold nanoparticles has relied on averaging many images together to create an average density map. This work represents the first electron microscopy constructed three-dimensional density map of a DNA double helix.

The recent invention of the graphene liquid cell is a breakthrough for in-situ liquid-phase transmission electron microscopy (TEM), and has allowed direct real-time atomic-resolution observation of the solution-phase growth and dynamics of nanocrystals and other atomic-scale structures. In a graphene liquid cell, the top and bottom membranes of an encapsulated bubble consist of relatively inert and ultra-strong single-atom-thick graphene sheets, which are filled with a liquid of interest. Previous studies [19] required the encapsulated liquid to be a high vapor pressure organic solvent. By adapting the liquid cell for aqueous environments, biological species can be studied in solution in real time. Gold nanoparticles were used as labels for short double stranded DNA in order to image its dynamics over an imaging time of minutes. Quantitative analysis of nanocrystal trajectories allowed the reconstruction of DNA

motion in three-dimensions. This technique, combined with the novel electron tomography technique described above, allows for highly detailed characterization of the building blocks of three-dimensional DNA-assembled nanoparticle plasmon rulers.

Chapter 2

Synthesis and characterization of nanocrystal molecules

Fabrication of nanocrystal molecules through the DNA-mediated assembly of colloidal metal nanoparticles provides numerous advantages over other techniques for producing sub-nanometer, optically coupled metal structures, such as lithographically. Large quantities of high quality metal nanoparticles can be synthesized quickly and inexpensively and chemically tuned to yield different sizes and aspect ratios of gold and silver rods, wires, spheres, prisms, and cubes. By changing the surface ligands, metal nanoparticles can be made stable in a variety of solvents and buffer conditions or the local dielectric environment can be tuned. Importantly, many assemblies can be synthesized in parallel in solution with high fidelity.

2.1 Nanocrystal synthesis and bioconjugation

Synthesis of gold nanoparticles

Gold colloids with nanoscale dimensions are typically synthesized in one of two way. The first method, originally discovered by Faraday in 1857 [20] and refined by Frens [21], involves reduction of gold salt in aqueous solution in the presence of citrate. In the other method, first described by Baughman and coworkers [22], gold nanoparticles are synthesized in a two phase system; nanoparticles are formed in inverse micelles. The latter method is limited in terms of particle size (generally less than 10nm) and monodispersity. Because uniform particle size is important to much of the research described in this thesis, gold nanoparticles were synthesized by the Frens method or obtained commercially.

In a typical Frens synthesis, a dilute aqueous solution of gold (III) chloride is heated and stirred vigorously. A solution of sodium citrate is injected. Particles form according to a diffusional growth process [23]. Gold ions are reduced forming clusters and atoms. Adatoms attach or detach from a particle surface depending on its size in relation to the so-called

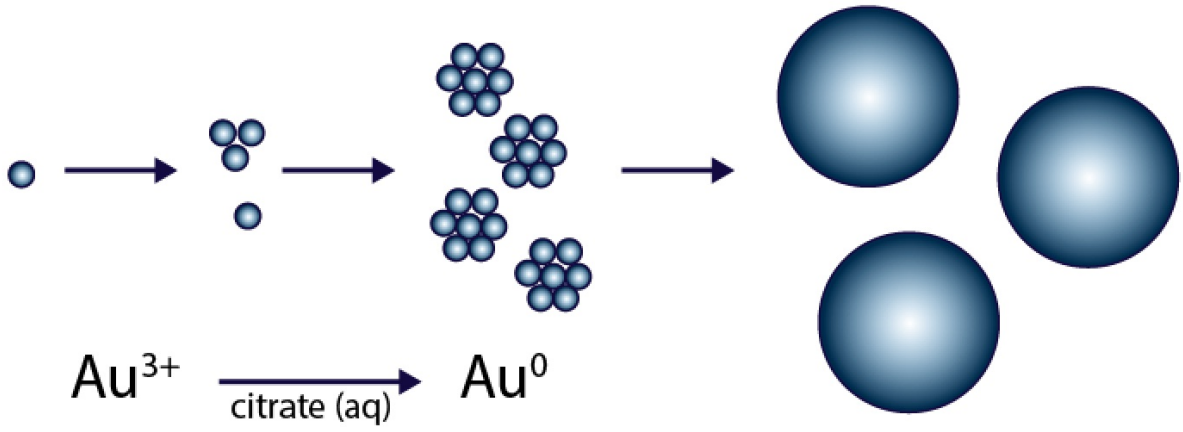

Figure 2.1: Gold ions are reduced in solution to form particle nuclei. As additional gold atoms are reduced, nuclei for to spherical nanoparticles.

critical size of the particle which is largely dependent on its surface energy. Due to the simplicity of this synthesis, the purity of the reagent used and the cleanliness of glassware is imperative to a high quality synthesis as defined by particle monodispersity and spherical particle morphology. An example synthesis is provided in Appendix A. Polydispersity of these particles can be monitored by small-angle x-ray scattering (SAXS) or dynamic light scattering (DLS). Morphology is characterized by electron microscopy.

Synthesis of gold nanorods

Nanoparticles with different morphologies have been produced using a variety of techniques. In solution, anisotropic particles are synthesized via etching, miceller process, or surface capping [24]. Gold nanorods are synthesized in the presence of cetyltrimethylammonium bromide (CTAB) which acts as a structure directing agent. This synthesis, originally developed by Murphy and coworkers [25, 26], relies on the differential binding of CTAB to different the different crystal faces of a gold nanoparticle. Gold, with face-centered cubic crystal structure, binds to CTAB with low affinity to {111} facets; the ends of a gold nanorod are thus {111}. The sides of the pentagonal rod are more poorly defined but are likely {110} or {100} [24, 27].

In the Murphy synthesis of gold nanorods, small gold seeds are synthesized and added to a growth solution to produce nanorods. Gold chloride is reduced by sodium borohydride in a saturated aqueous solution of CTAB. To control the morphology of the particle, the seed solution is diluted in a growth solution containing additional gold salt, a high concentration of CTAB, ascorbic acid serving as a weak reducing agent, and silver nitrate. The presence of silver ions has been shown [26] to increase the yield of nanorods with respect

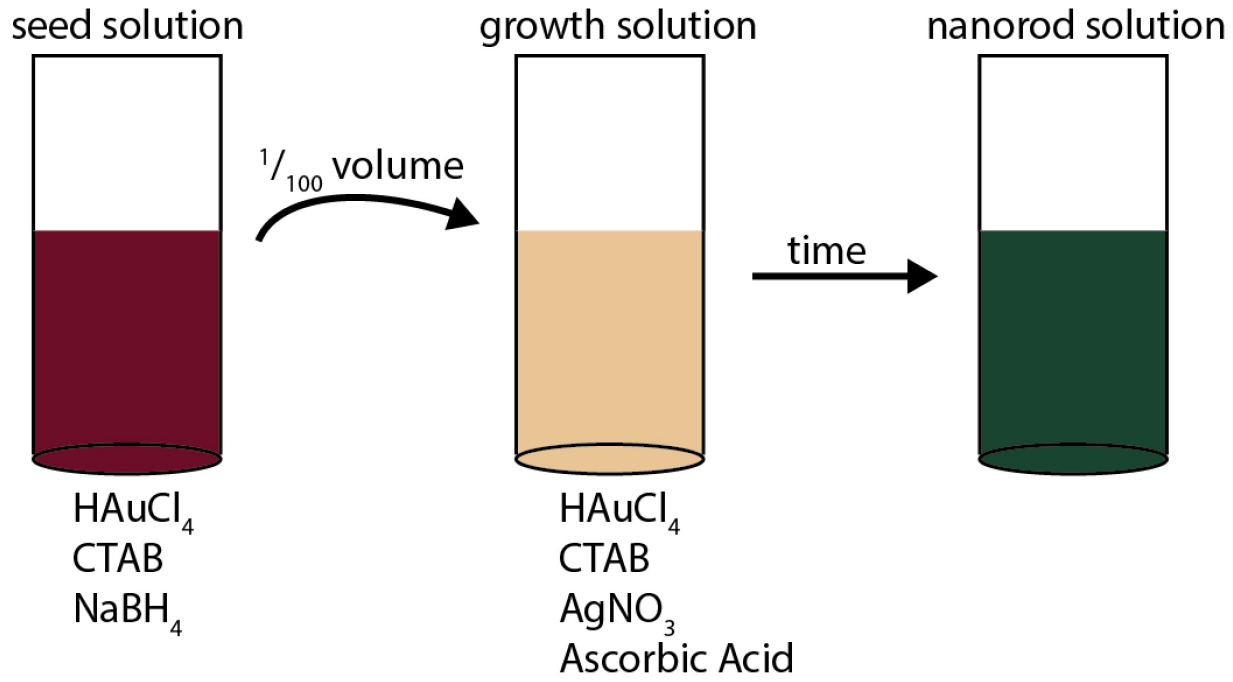

Figure 2.2: Gold nanorods are synthesized in a stepwise process. First, small seeds are formed by fast reduction. Then, a small volume of seeds is added to a growth solution. Over time, the surfactant acts as a structure directing agent and nanorods are formed.

to other particle morphologies, largely spheres. It's hypothesized that the silver ions were preferentially reduced on the {110} facet of the gold nanoparticle [28]. Because CTAB binds strongly to silver, the structure-directing properties of CTAB are enhanced for this system resulting in a higher yield of nanorods. As a result of the very subtle difference in affinity of CTAB for different FCC crystal facets, the success of a gold nanorod synthesis relies on the absence of significant impurities. In particular, iodide impurities in CTAB from different suppliers or different batches from the same supplier has been shown to prevent the formation of nanorods in high yield [29]. Interestingly, iodine has been shown to be necessary for the formation of gold nanoprisms which are synthesized by a similar procedure [30, 31]. An example synthesis is provided in Appendix B.

Conjugation of DNA to gold nanoparticles

In 1996, the Alivisatos group published an account of gold nanoparticles organized by DNA [9]. Subsequently, this method has been refined [32–34] in order to synthesized increasingly complex structures. These structures are created (shown in Figure 2.3) when gold nanoparticles are conjugated to single stranded DNA, separated by DNA valency (discussed

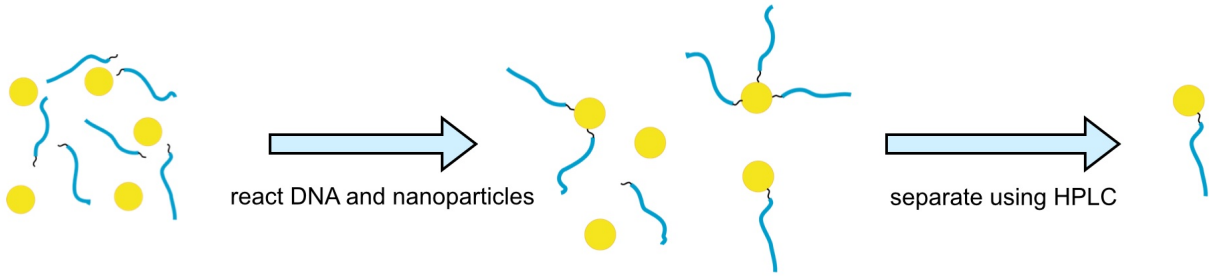

Figure 2.3: When thiolated DNA reacts with gold nanoparticles, a statistical mixture of products results. As a result, a separation step is necessary for a high yield of singly DNA-conjugated gold nanoparticles.

in Section 2.2), and combined to assemble into structures as programed by the DNA strands. Before they may be separated by gel electrophoresis or high performance liquid chromatography (HPLC), nanoparticles must be reacted with DNA specifically through a thiol bond such that the conjugates are stable to aggregation.

Nanoparticle surface chemistry is important to the success of a DNA-nanoparticle conjugation reaction. When synthesized as described above, spherical gold nanoparticles are capped by negatively charged citrate molecules as a surface ligand. This negatively charged coating is sufficient to stabilize the small gold particles against aggregation in pure water as the repulsive force between the particles is greater than the attractive Van der Waals force between them. When the ionic strength of the solution is increased, by the addition of an electrolyte like NaCl or in order to change the buffer conditions of solution, the double layer decreases resulting in aggregation. A number of of different passivating agents have been used to avoid aggregation of nanoparticles in high ionic strength solutions including small molecules, polymers, and biomolecules [35–39]. In the syntheses reported in this dissertation, citrate-capped gold nanoparticles are place exchanged with bis(p-sulfonatophenyl)phenyl phosphine dehydrate dipotassium salt (BSPP). The negatively charged tertiary phosphine surface ligand stabilizes the particles against aggregation in moderate ionic strength (5-100mM) solution, the conditions required for reaction with DNA.

The reaction conditions of conjugation of DNA to a gold nanoparticle surface must be carefully controlled to prevent non-specific binding of DNA. Nucleic acids have long been known to bind to gold surfaces [40]. With respect to gold nanoparticles, the non-specific binding of DNA has been demonstrated to depend on DNA length [41] and sequence [42]. Non-specific binding of DNA has also been shown to increase over time [43, 44] as well as with increasing nanoparticle size [45].

To specifically conjugate DNA to a gold nanoparticle surface, the DNA is chemically mod-

ified on the 5′ or 3′ end to include a thiol moiety. When synthesized on a solid support, DNA leaves an exposed [46] nucleoside phosphoramidites which readily reacts with nucleophiles. Through this mechanism a number of thiol modications have been made to oligonucleotides [46–48]. The covalent sulfur-gold bond has been measured to be robust [49]. To increase the strength of the interaction between the gold surface and the DNA, moieties containing multiple thiols have been used [47]. In particular, a branched trithiol modification, used in this dissertation, developed by Letsinger and coworkers [48] provides stability as a multipoint anchor when a solution contains reducing agents [38]. The experimental details of a typical gold nanoparticle bioconjugation reaction to DNA are found in Appendix C, including oligonucleotide vendors and purification parameters. A number of nanoparticles other than gold spheres have been incorporated into these assemblies, including semiconductor nanocrystals [50] and silver particles [51].

2.2 Separation and assembly of DNA-nanoparticle conjugates

Agarose gel electrophoresis

Gel electrophoresis has been used to separate biomolecules like DNA and proteins by molecular weight, charge, and other chemical properties. Molecules are separated as they're pulled through a porous matrix by an applied potential. Polyacrilimide gel is commonly used to separate proteins and short strand of DNA. Agarose has historically been used for gene-length DNA due to the comparatively large pore size of the carbohydrate matrix. It's also been shown to sieve nanoparticles according to the number of attached DNA strands [32, 52].

Mobility in agarose gel electrophoresis (Equation 2.1) depends on the free solution mobility (μ_0) as well as the radius of gyration (R_g) of the species and the pore size (a) [53]. Free solution mobility (Equation 2.2) depends on the charge (Q) and frictional coefficient (ξ) and is constant ($2 \cdot 10^{-4}\, cm^2/V \cdot s$) regardless of length for DNA.

$$\frac{\mu}{\mu_0} = \exp -\left(\frac{R_g}{a}\right)^2 \tag{2.1}$$

$$\mu_0 = \frac{Q}{\xi} \tag{2.2}$$

Average pore size for an agarose matrix depends on concentration. It's been empirically determined to decrease with increasing gel concentration by techniques including atomic force microscopy [54]. Equation 2.3 holds for .5-3% agarose gels by weight cast from the

standard tris-borate-EDTA running buffer. The pore diameter (in nanometers) relates to the weight percent (A) expressed in g/mL.

$$a \simeq \frac{89}{a^{2/3}} \tag{2.3}$$

At constant gel concentration, differentially analyte mobility is strongly dependent on the radius of gyration. For DNA, the radius of gyration is given by Equation 2.4 dependent on the length of the DNA (L) and the persistance length (p), about 2nm for single-stranded DNA. Treating DNA as a freely-joined-chain is valid in the limit of pore size greater than R_G; this condition holds for DNA shorter than 200bp. The radius of gyration of a solid sphere is given by Equation 2.5.

$$R_g^2 = \frac{1}{3}pL\Big(1 - \frac{p}{L} + \frac{p}{L}\exp\Big(-\frac{L}{p}\Big)\Big) \tag{2.4}$$

$$R_g^2 = \frac{3}{5}R^2 \tag{2.5}$$

The radii of gyration are additive; thus, each additional ssDNA conjugated to a nanoparticle will retard the DNA-nanoparticle conjugate in the gel. Agarose gel electrophoresis as described in this dissertation is performed according to an unexotic protocol: 1-3% agarose gels are cast from .5x TBE and run at 7.5 V/cm. Discrete bands corresponding to the number of attached DNA strands are routinely observed, but with fairly low resolution due to longitudinal diffusion and polydispersity of nanoparticle diameter. Gel electrophoresis continues to be an excellent method for the separation of assembled DNA-nanoparticle structures.

High performance liquid chromatography

High performance liquid chromatography (HPLC) has been shown to separate DNA-gold nanoparticle conjugates according to DNA valency [34]. Charged DNA-nanoparticle species adsorb to an anion-exchange column and elute as a salt gradient is applied. Using this technique, baseline resolution between singly-, doubly-, and un-conjugated nanoparticles has been achieved.

Like other forms of liquid chromatography, separation by HPLC requires a stationary phase past which a liquid phase is flowed. In anion-exchange chromatography, the column is packed with silica microbeads coated with 13μm particles of anion-exchange resin. The resin displays ammonium cations which interact with the negatively charged analyte. The equilibrium between the stationary phase, analyte, and counter-ion is described in Equation 2.6:

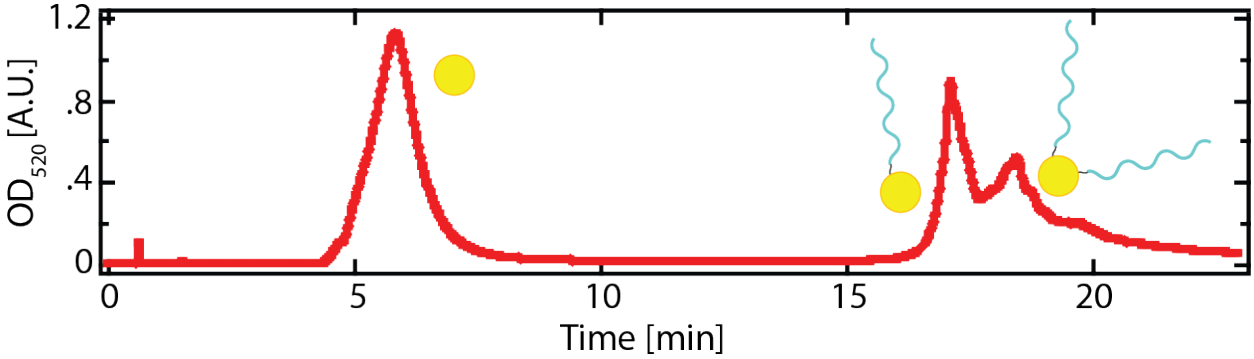

Figure 2.4: An example chromatogram.

$$K_{ex} = \frac{[sA][Cl^-]}{[sCl][A^-]} \tag{2.6}$$

Though the mechanism of interaction between the stationary phase and analyte is only partially understood [55], Strube and coworkers derived a relation between the charge of an analyte with respect to the charge of the stationary phase (Z_p/Z_s), the concentration of the counter-ion (C_m), and retention of the analyte [56]:

$$\log k \propto -\frac{Z_p}{Z_s} \log C_m \tag{2.7}$$

Thus for each additional strand of DNA conjugated to a nanoparticle, the retention (k) increases. Higher order conjugates have a smaller difference in retention than the difference between unconjugated nanoparticles and monoconjugtes. Also implied by this equation, longer strands of DNA will improve the separation.

A major experimental consideration is the surface charge of the nanoparticle. To avoid aggregation in the high salt conditions of HPLC, gold nanoparticles are modified with a short chain (6 unit) thiol-modified PEG molecule terminated with either a hydroxy or carboxyl functional group. The molecule forms a self-assembled monolayer on the surface of the particle protecting it from aggregation while the total charge of the particle can be changed by adjusting the ratio of hydroxy- versus carboxy- terminated PEG. Extrapollating from Equation 2.7, the more neutrally charged the particle, the better the separation which has been observed experimentally. By considering the particle size, DNA length, and surface ligand charge, a large variety monoconjugates can be produced in high yield using HPLC.

Assembling monoconjugates into structures

High purity monoconjugates are necessary for nanoparticle assembly by DNA. Once monoconjugates have been purified, they're combined in moderate ionic strength solution (50-150mM) and allowed to assemble for 2-48 hours at room temperature or at a temperature profile controlled by a thermal cycler. Simple structures, like dimers, may assemble in high yield without further purification. More complex structures are further purified, commonly by gel electrophoresis.

Nanoparticles assemble according to the programmed base-pairing of DNA. Many dissertations have been written about calculating the lowest energy secondary structure of DNA. The algorithm used for designing the DNA sequences used in this dissertation is calculated using nearest-neighbor empirical parameters as implemented by Pierce and coworkers [57].

Characterization of assembled DNA-nanoparticle nanostructures remains challenging. Structures are commonly analyzed by transmission electron microscopy (TEM). In order to image samples, they're dried on a carbon-coated copper gird. During this drying process, capillary forces pull the nanoparticles together, distorting DNA structure [58, 59]. Some image analysis has been done to confirm that particles are indeed dimers, for instance, rather than particles that happen to be near one another [52, 60]. Extracting additional structural information is difficult, particularly because DNA is electron transparent. State-of-the-art electron microscopy techniques are used in this dissertation (Chapter 5) to improve the characterization of DNA-gold nanoparticle assemblies. A powerful method for characterizing gold nanoparticle assemblies by their functional properties is by probing their surface plasmon coupling by ensemble or single particle spectroscopy.

2.3 Optical properties of metal nanoparticles

Nanoparticle surface plasmons

Metal nanoparticles owe their brilliant optical properties to their surface plasmon, or the collective oscillation of conduction electrons. Because nanoparticles are on the same order of magnitude as the penetration depth of electromagnetic radiation in metals, light can penetrate the particle shifting its charges. This charge concentration and the corresponding restoring force induces an oscillation which relaxes, scattering light from the particle.

The surface plasmon of a nanoparticle can be described by Mie theory, so named because Gustav Mie solved Maxwell's equations [61] for a sphere in 1908 [62]. The solution can be simplified for particles much smaller than the wavelength of incident light [1, 2]. For particles this small including those used in this dissertation, we may invoke the dipole approximation, discarding all higher order modes from Mie theory. An additional simplification, first noted by Lord Rayleigh [63], may be made by considering the particles' size relative to light. This

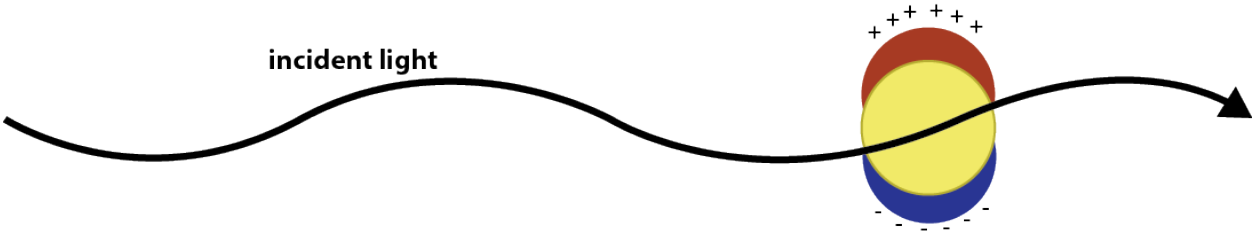

Figure 2.5: Electrons oscillate in response to resonant light.

quasi-static approximation allows the phase of light to be treated as constant. The result, the Classius-Mossotti relation [64], is the polarizability (α) of a sphere as a function of the dielectric (ϵ) of the metal:

$$\alpha = 3\epsilon_0 V \frac{\epsilon - \epsilon_m}{\epsilon + 2\epsilon_m} \tag{2.8}$$

In 2.8, V is the volume of the sphere, ϵ_0 is the permittivity of free space, and ϵ_m is the dielectric constant of the surrounding medium. From this equation, the polarizability has a strong maximum when the dielectric of the metal is twice the opposite of the dielectric of the medium (Equation 2.9). As the dielectric of the metal is the sum of its real and imaginary parts (Equation 2.10) and the imaginary part is small [65], Equation 2.9 can be simplified (Equation 2.11).

$$\epsilon = -2\epsilon_m \tag{2.9}$$

$$\epsilon = \epsilon - r + i\epsilon_i \tag{2.10}$$

$$\epsilon_r = -2\epsilon_m \tag{2.11}$$

Since this condition (Equation 2.11) is satisfied for noble metals like gold and silver in the visible frequency regime, gold and silver nanoparticles exhibit strong absorption and scattering in the visible. Some light that the particles absorb at the resonance frequency is dispersed non-radiatively rather than radiately scattered. Damping can occur through collisions with lattice phonons, the nanoparticle surface, or other defects resulting in the generation of heat. The extinction and scattering cross-sections of nanoparticles depend on their size, with larger particles scattering more light.

Mie theory nicely explains the resonant frequency of a small metal sphere, but does not account for phenomena such as the dependence of the resonant frequency on particle size. Nor does Mie theory account for variation in nanoparticle morphology.

When the diameter of a nanoparticle exceeds the penetration depth it can no longer be evenly polarized by the light, resulting in the excitation of higher-order oscillation modes [66]. Higher-order oscillations are resonant at higher frequencies, significantly broadening the plasmon resonance due to a reduction in the phase coherence [65]. As the particle diameter increases, the increase in radiative damping reduces the plasmon lifetime resulting in increased broadening [67]. This can be seen in Figure 2.6 showing extinction spectra of gold nanoparticle solutions ranging 10 to 150 nm in diameter. These factors broaden the plasmon band of a nanoparticle solution homogeneously. Inhomogeneous broadening occurs due to the distribution of sizes present in nanoparticle solutions.

The optical properties of a gold nanorod can be modeled as an extension of Mie theory by approximating the particle as an ellipsoid. Ellipsoidal particles are characterized by the three axes a, b, and c. A gold nanorod is a prolate spheroid with $a > b = c$; an analytical solution of Maxwell's equations exists for this geometry [2] which employs L_i as a geometrical factor. The polarizability along axis i is given in Equation 2.12:

$$\alpha_i = \frac{V\epsilon_0}{L_i} \frac{1-\epsilon_r}{(1/L_i - 1) + \epsilon_r} \tag{2.12}$$

For polarizability along the longitudinal axis of the ellipsoid, the geometry factor is given by equation 2.13:

$$L_a = \frac{1-f^2}{f^2}\Big(-1 + \frac{1}{2f} \ln\Big(\frac{1+f}{1-f}\Big)\Big) \; where \; f^2 = 1 - \frac{b^2}{a^2} \tag{2.13}$$

This approximation can be useful for short gold nanorods (aspect ratio <2). For longer nanorods, the more realistic geometry of a cylinder with spherical end-caps provides a more accurate model. No analytical solution to Maxwell's equations exists for this geometry, so finite element methods such as or finite-difference time-domain (FDTD) [3] or the discrete dipole approximation (DDA) [4] must be used. The ellipsoidal approximation can give a qualitative understanding of the optical behavior of these particles, particularly their coupling when brought into proximity.

Plasmon coupling in metal nanoparticles

The optical properties of metal nanoparticles have been shown to vary when the particles are brought into proximity [68–71]. In particular, the peak scattering frequency of nanoparticles

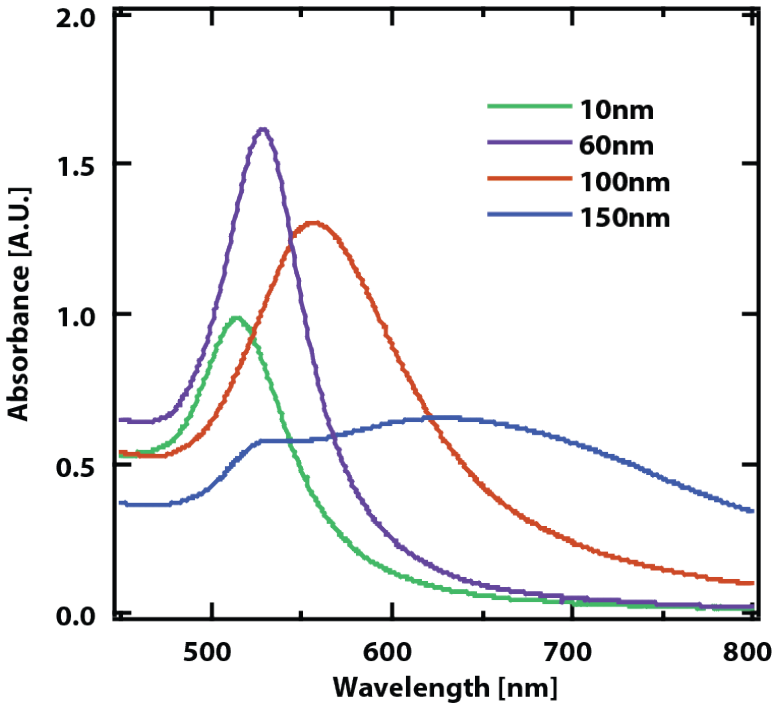

Figure 2.6: Extinction of various sizes of gold nanoparticles.

have been shown to red-shift. In addition to lithographically prepared substrates and random colloidal aggregates of spherical particles, gold nanorods [72] and nanoparticles assembled by DNA[14, 15, 73, 74] have exhibited spectral shift.

The optical properties of a metal nanoparticle are determined by its surface plasmon resonance which in turn is caused by an incident electromagnetic field. When two plasmonic nanoparticles are near one another, the oscillations of one plasmon can couple to another. The effective electric field a nanoparticle interacts with is perturbed by the electric field of the proximate particle. In the case where both particles can be modeled as point dipoles, the electric field felt by each particle is the sum of the incident light and the perturbation due to the presence of the electric dipole present on the neighboring particle [75]:

$$E' = E + \xi \frac{\mu}{4\pi\epsilon_m\epsilon_0 d^3} \tag{2.14}$$

where μ is the dipole moment due to the particle surface plasmon and d is the inter particle distance. Thus, the surface plasmon maximum is shifted for a particle near another particle with respect to an isolated particle. This effect decreases strongly with distance.

Nordlander and coworkers have described nanoparticle plasmon coupling in analogy to

molecular orbital theory [76]. Their analogy renders intuitive the concept that the surface plasmon frequency of a nanoparticle would shift when brought near another and that shift would depend on distance. This analogy becomes particularly useful when considering nanoparticles with different surface plasmon frequencies [51]. Coupling between nanoparticles can be measured using ensemble UV-visible spectroscopy or single particle darkfield microscopy. In darkfield microscopy, nanoparticles immobilized on a substrate are illuminated via a condenser which shines visible light at an oblique angle. The objective collects scattered light; thus, the background appears dark with points of light that result from a surface plasmon coupling into the far field. Single particle darkfield microscopy is a powerful tool that can eliminate effects from nanoparticle polydispersity and synthetic impurities. Some phenomena, however, cannot be measured on the single particle level. Included among these is circular dichroism, a typical technique for elucidating the chirality of an object.

Circular dichroism

Chiral arrangements of metal nanoparticles have been shown to exhibit optical activity as measured by circular dichroim [77–81]. This optical property of chiral nanoparticle clusters was predicted using finite element computational methods mentioned above [82, 83]. By understanding the origins of optical activity from a chiral arrangement, the measured circular dichroism of a chiral cluster of nanoparticles can be expected.

An object can be chiral in three dimensions if belongs to the point groups C_n, D_n, or T. Many chiral objects fit the common definition of a chiral molecule, one that is non-superimposable on its mirror image. Chiral molecules have long been known exhibit optical activity [84], defined as a differential absorption of chiral light (left-hand and right-handed circularly polarized light) as well as circular birefringence. This circular birefringence results in the rotation of plane polarized light which was used in the first experiments elucidating molecular chiral centers. Modern experiments on chiral molecules measure circular dichroism, the wavelength dependent difference in extinction between circular polarizations (Equation 2.15). Circular dichroism can be transformed to optical rotation by the Kramers-Kronig relation.

$$CD = \epsilon_{LCP} - \epsilon_{RCP} \tag{2.15}$$

In large molecules, it was determined that in addition to the effect of chiral centers, optically activity could be observed from a dipolar functional groups [85]. For example, the bases in a DNA double helix are strong dipoles arranged in a chiral helix [86] and a strong circular dichroism is observed for double stranded DNA. Since a chiral arrangement of dipoles in a molecule exhibits circular dichroism, we can expect the same from a chiral arrangement of nanoparticles.

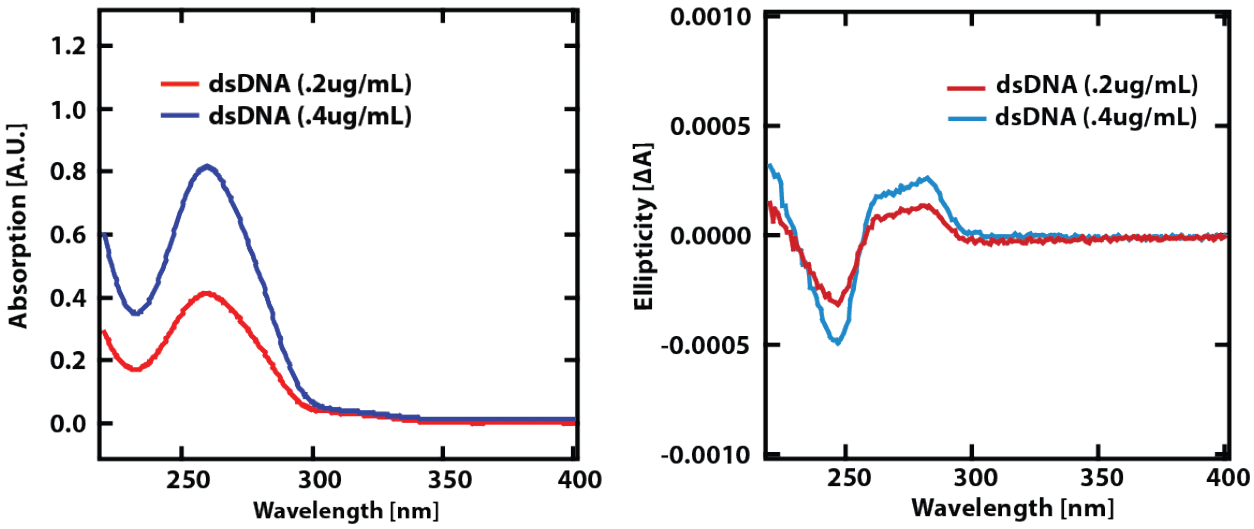

Figure 2.7: Circular dichroism occurs at the absorbance maximum and is proportional to concentration.

Optical activity in molecules, polymers, or nanoparticles can be measured by circular dichroism spectroscopy. This ensemble technique is similar to UV-visible spectroscopy. A high intensity, broadband light source is introduced to a monochromator. Rather than directed straight through the sample to a photomultiplier detector, the light passes through a photoelastic modulator. A birefrigent element can quickly change the phase of light from left- to right- handed circularly polarized light. To measure the difference between these signals, lock-in detection is used to improve signal to noise. Using DNA to assemble metal nanoparticles with the optical properties of surface plasmons in mind, solution-phase nanostructures can be designed which will exhibit circular dichroism under ensemble detection.

Chapter 3

Controlling the orientation of DNA-assembled gold nanorods

3.1 Introduction

Gold nanorods have found broad biological applicability [87–92] because of their strong absorption and scattering which is tunable into the infrared. The scattering frequency of a gold nanorod is commonly tuned by changing the size or aspect ratio of a nanorod which changes the resonant frequency of the nanoparticle surface plasmon, the collective oscillation of conduction electrons [65]. The resonant frequency of a nanoparticle surface plasmon is sensitive to particle-particle distance and surrounding medium, allowing nanorods to be used as sensitive biosensors [93–95]. Because the light scattered when surface plasmon couples to incident light is photostable, in contrast to most fluorophores, gold nanorods have been used as labels for the optical microscopy of tissues and cells [88]. Gold nanorods have been conjugated to biomolecules, such as antibodies, in order target specific cell types, such as cancer cells [87]. In addition to light scattering, absorption by gold nanoparticles is converted to photothermal energy which has been utilized by a number of applications. El Sayed and coworkers used antibody-tagged gold nanorods in the specific photothermal therapy of cancer cells [89] while Zharov and coworkers demonstrated the selective elimination of bacterial cells [90]. The local heating of irradiated nanorods has been used by Lee and coworkers to deliver DNA and RNA inside cells to selectively manipulate gene regulation [91, 92].

In addition to the conjugation of gold nanorods to peptides [96], antibodies[97, 98], glycoproteins [99], many applications rely on conjugating nucleic acids to the nanorod surface. Because gold nanorods are stabilized by cetyltrimethylammonium bromide (CTAB), a cationic surfactant, a major challenge of conjugating negatively charged DNA through a specific chemical modification is avoiding non-specific interaction. Studies to date [13, 100–107] have focused on maximizing DNA packing on the nanorod surface to for polyvalent functional conjugates. A common protocol for conjugating thiolated DNA to the surface of

a gold nanorod involves removing excess CTAB from solution then introducing DNA in the presence of a high concentration (.1-.2M) of NaCl and a negatively charged surfactant such as sodium dodecyl sulfate (SDS) to disrupt the surfactant layer at the surface of the rod [13, 100]. The resulting gold nanorod conjugates have high surface coverage of DNA, which has the ancillary benefit of stablizing gold nanorods against aggregation. Modifications on this procedure include the co-addition of thiolated polyethylene glycol (MW = 5000) to further stabilize the nanorods [101], using lower pH rather than SDS to disrupt the CTAB bilayer [102], round-trip phase transfer for the removal of CTAB [103], and the use of disrupting agents other that SDS [104].

These polyvalent DNA-gold nanorod conjugates have been assembled into a number of structures. By controlling the DNA sequences and reaction conditions, well-ordered extended solids have been synthesized and characterized by small-angle x-ray scattering [13] and circular dichroism [108]. These extended structured have found therapeutic [109] and biosensing [110] applications. Gold nanorods have been assembled with control over the number of particles and relative orientation with DNA-origami [105]. The regiospecificity of gold nanorod-nanosphere assemblies has been controlled by selectively removing the CTAB of the nanorod end caps to control the sequences of DNA on the sides of the nanorods [111].

Previous research in the Alivisatos group has shown that nanorods can be assembled into precise geometries when modified with a controlled number of oligonucleotides [9]. This method involves conjugating thiolated DNA with gold nanoparticles then separating the mixture of products by DNA valency using gel electrophoresis [32] or HPLC [34]. The resulting monoconjugates have been used to make dimers [32], trimers [33], pyramidal groupings[112], and satellite structures [113] as well as structures containing semiconductor quantum dots [50] and silver nanoparticles [51]. Optical coupling between the nanoparticles has resulted in a biosensor termed a "plasmon ruler"[14, 15]. DNA-assembled nanoparticles report changes interparticle distance through a shift in maximum scattering frequency. An adapted plasmon ruler has been used to image caspace-3 activity in live cells [16].

To create a plasmon ruler that senses the conformational changes ubiquitous in biological systems, anisotropic elements must be used. A three-dimensional plasmon ruler consisting of two stacked pairs of nanorods and a fifth, symmetry-breaking nanorod has been theorized [17]. This geometry has been calculated to be sensitive to small changes in the relative arrangement of the nanorods. In order to adapt the advantages of this plasmon ruler to biological systems, colloidal gold nanorods must assembled into discrete structures with defined relative orientation.

Herein we describe a method for the assembly of gold nanorods with defined orientation using DNA. Gold nanorods are synthesized, ligand-exchanged, and conjugated to thiolated oligonucleotides. Monoconjugates are separated from other products by HPLC and reacted to form dimers. Through TEM image analysis, it's shown that dimers can be separated by

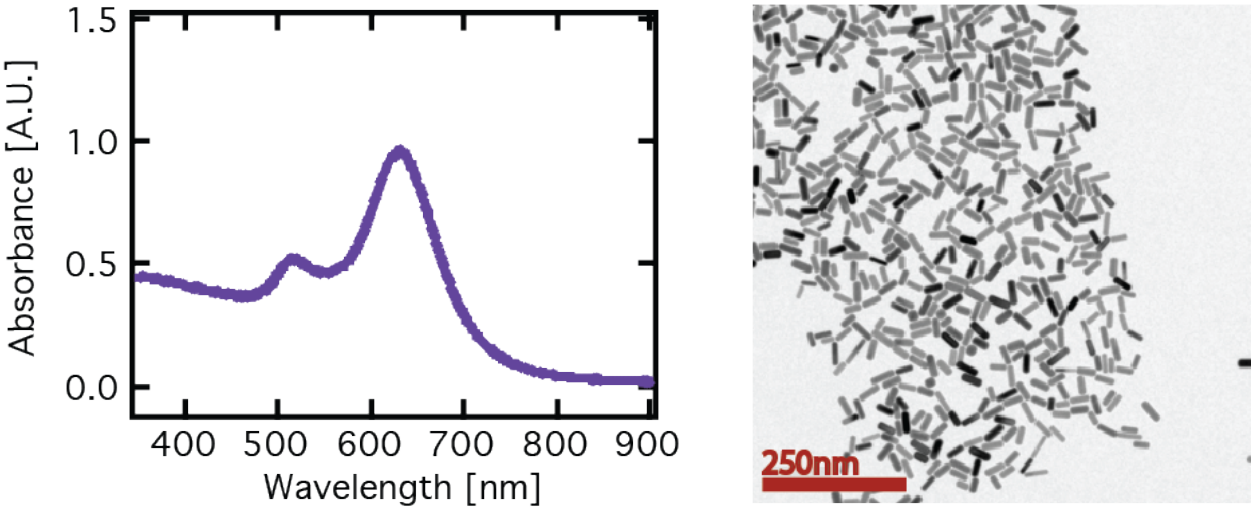

Figure 3.1: Nanorods synthesis shows monodisperse particles that show and longitudinal and transverse plasmon by UV-visible spectroscopy.

orientation by agarose gel electrophoresis. The resulting structures exhibit ensemble plasmon ruling-behavior.

3.2 Gold nanorod synthesis and assembly

Synthesis of gold nanorods

Gold nanorods were synthesized according to a procedure modified from the seed-mediated synthesis reported by Murphy and coworkers [25]. Reagents were purchased from Alfa Aesar (Ward Hill, MA) and used without further purification. All glassware was cleaned overnight in a base bath and rinsed copiously with MilliQ water. To ensure complete dissolution, CTAB solutions were prepared volumetrically then sonicated for 20 minutes at 30°C. To synthesize seeds, .6mL of .01 M $NaBH_4$ was added to a stirring solution of .1M CTAB and .25mM $HAuCl_4$ and allowed to stir for two minutes. To synthesize gold nanorods, 55μL 0.01 M $AgNO_3$, .5mL .01M $HAuCl_4$, 55μL .1M ascorbic acid was added to 9.5mL .1M CTAB. To this growth solution, 12μL seed solution was added. The solution was allowed to age for 24-48 hours without disruption for nanorods to form. Products were analyzed by TEM and UV-visible spectroscopy. Nanorods were stored in .05M CTAB for up to three weeks.

Removing CTAB from gold nanorods

Gold nanorods were purified from other reaction products by centrifugation. A 10mL reaction of gold was diluted to 50mL with MilliQ water and sonicated for 15 minutes at 30°C to

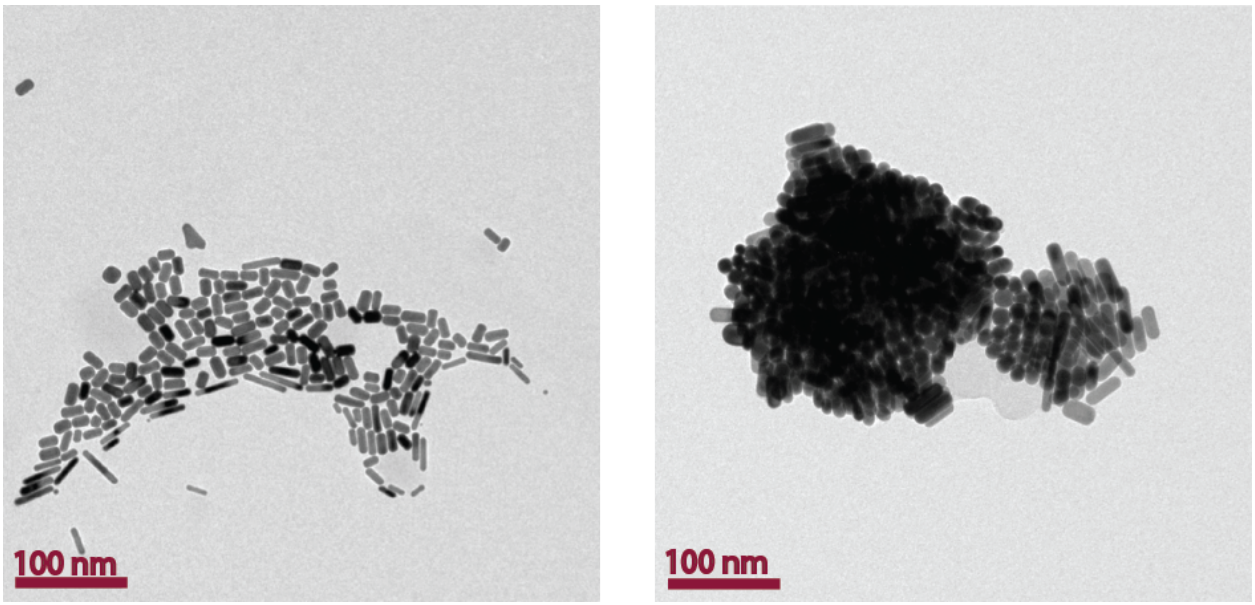

Figure 3.2: After CTAB is removed, particles are stabilized by BSPP.

dissolve CTAB crystals. Nanorods were washed three times with MilliQ water by centrifugation at 9,000rpm. After the third centrifugation, the pellet was resuspended in 10mg/mL bis(p-sulfonatophenyl)phenyl phosphine dehydrate dipotassium salt (BSPP) (Strem Chemicals, Inc, Newburyport, MA) to .5mL and added to .5mL phenol:chloroform:isoamyl (25:24:1) (Sigma-Aldrich, St Louis, MO) in a 2mL glass vial equipped with a magnetic stir bar. The size of the vial and volume of solution proved vital to the success of the ligand exchange, likely effecting the quality of the emulsion. The solution was allowed to stir overnight forming a milky emission. To remove BSPP-coated nanorods from the organic layer, the solution was transferred to a 1.5mL conical vial and allowed to rest for 1 hour. The aqueous layer was removed via pipet and filtered through a 2 micron PTFE string filter to remove aggregates. Characterizing the concentration of nanorods using UV-visible spectroscopy is an exercise in estimation. A qualitative measure of concentration was made by considering the optical density at 520nm related to the concentration through the extinction coefficient of 20nm gold nano sphere. TEM analysis indicates that nanorod morphology is unchanged by ligand exchange to BSPP. The net surface charge of the BSPP-nanorods was determined by agarose gel electrophoresis. BSPP-exchanged particles remained stable for up to two days when stored at room temperature.

Conjugating DNA to gold nanorods

DNA sequences with $5'$ branched trithiol modification were purchased from Fidelity Systems, Inc (Gaithersburg, MD). Prior to reaction with gold nanorods, oligonucleotides were deprotected by reducing the disulfides on immobilized Tris(2-carboxyethyl)phosphine (TCEP)

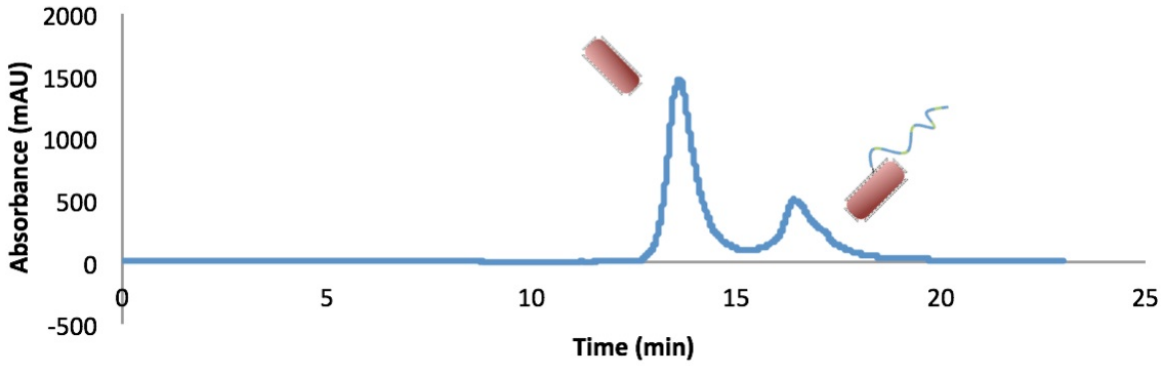

Figure 3.3: HPLC of gold nanorods conjugated to DNA.

(Pierce, Waltham, MA). Oligonucleotides were allowed to react with TCEP beads for 30 minutes then purified by centrifugation. DNA was added to BSPP-coated gold nanorods at a stoichiometric ratio of 10:1. The ionic strength of solution was increased by adding 200mM NaCl in 5μL aliquots to a final concentration of 25mM to a final reaction volume of 100μL. The solution was allowed to react, unperturbed, overnight at room temperature.

Separation of DNA-gold nanorod conjugated by HPLC

In order to be analyzed by HPLC, the nanoparticle surface must be modified by a highly-ordered self-assembled monolayer to prevent aggregation on the column. Previous studies of HPLC of gold nanoparticles [15, 34] have used short chain thiolated PEG ligands terminated with either a carboxyl or hydroxyl group. The PEG ligands used in this study also have an 11 carbon aliphatic spacer to increase packing efficiency on the nanoparticle surface, HS-$(CH_2)_{11}$-EG_6-COOH and HS-$(CH_2)_{11}$-EG_6-OH (Prochimia Surfaces, Sp.z, Sopot, Poland).

To prevent aggregation during the reaction with PEG, DNA-nanorod conjugates are diluted 10x to 1mL total reaction volume before 10μL of 20mM PEG solution is added. The conjugates react with PEG for one hour, then 5uL aliquots of 200mM NaCl are added to a final concentration of 25mM. After another hour, the nanorods can be anaylzed by HPLC.

Monoconjugated nanorods were separated from other reaction products by anion exchange HPLC. On an Agilent 1100 series HPLC, nanoparticles were applied to a a Dionex DNA-Pac PA100 anion exchange column (Sunnyvale, CA). Samples were eluted by NaCl gradient (40 mM to 900 mM over a period of 20 minutes), detected by absorption at 630nm. Collected fractions were diluted 5x and concentrated to 20uL by Amicon Ultra spin filter, MW 100,000 (EMD Millipore Corp, Billerica, MA).

Separation of dimers by gel electrophoresis

Conjugates were combined stoichiometrically as determined by optical density at 630nm and allowed to react overnight at room temperature. The dimers were purified from unreacted monoconjugates by agarose gel electrophoresis. Dimer solutions were applied to a slab agarose gel (3% w/w) in a running buffer of 45mM Tris-borate and .5mM EDTA and run at 7.5 V/cm along with appropriate monoconjugate controls. Dimer bands were extracted from the gel with a clean razor blade. DNA-assembled nano structures were extracted by inserting the excised gel into dialysis tubing (SnakeSkin dialysis tubing, MWKO 10K, Thermo Scientific) along with 1mL of running buffer. After extraction from the agarose matrix, the dimers were drop cast onto a carbon-coated copper grid and characterized by TEM.

3.3 Results and discussion

Through careful control of surface chemistry, gold nanorods were conjugated to oligonucleotides and separated by DNA valency using anion exchange HPLC. Thiolated oligonucleotides cannot be added to a gold nanorod solution as synthesized without disrupting the CTAB bilayer on the nanorod surface because the negatively charged DNA will bind nonspecifically with the positively charged CTAB. Previous reports of conjugating DNA to gold nanorods relied on creating a monolayer of close-packed DNA to stabilize the particle as the CTAB bilayer was disrupted by a negatively charged surfactant [13, 100]. In order to modify the particle surface with a small number of oligonucleotides, the CTAB ligand shell had to be removed and the nanoparticle stabilized in aqueous solution. The negatively charged phosphine BSPP was used for this purpose. If a positively charged surfactant is present in a solution of negatively charged gold particles, the particles are likely to aggregate. Thus, the solubility of CTAB is polar organic solvent was used to extract the place-exchanged CTAB into the phenyl:chloroform:isoamyl layer. Once the nanorods were coated in BSPP, they could be reacted with thiolated oligonucleotides and separated by HPLC, similar to published procedures [15, 34]. Purified monoconjugates were reacted stoichiometrically and separated by gel electrophoresis. Dimers of nanorods connected by 63bp double stranded DNA were resolved on a 1.5% gel in .5x TBE buffer run at 7.5 V/cm and extracted. TEM analysis indicates that of 243 rods imaged, 181 were in a dimer but that there was no orientation preference of the dimers.

Though some groups have found it possible to selectively remove the CTAB on the ends of the gold nanorods [111, 114], any amount of remaining CTAB would interfere with the DNA reaction scheme. Thus, to exercise control over the relative orientation of nanorod in these assemblies, regiospecificity must be obtained through separation of the final reaction products. Agarose gel electrophoresis is known to depend on the radius of gyration (Equation 3.1).

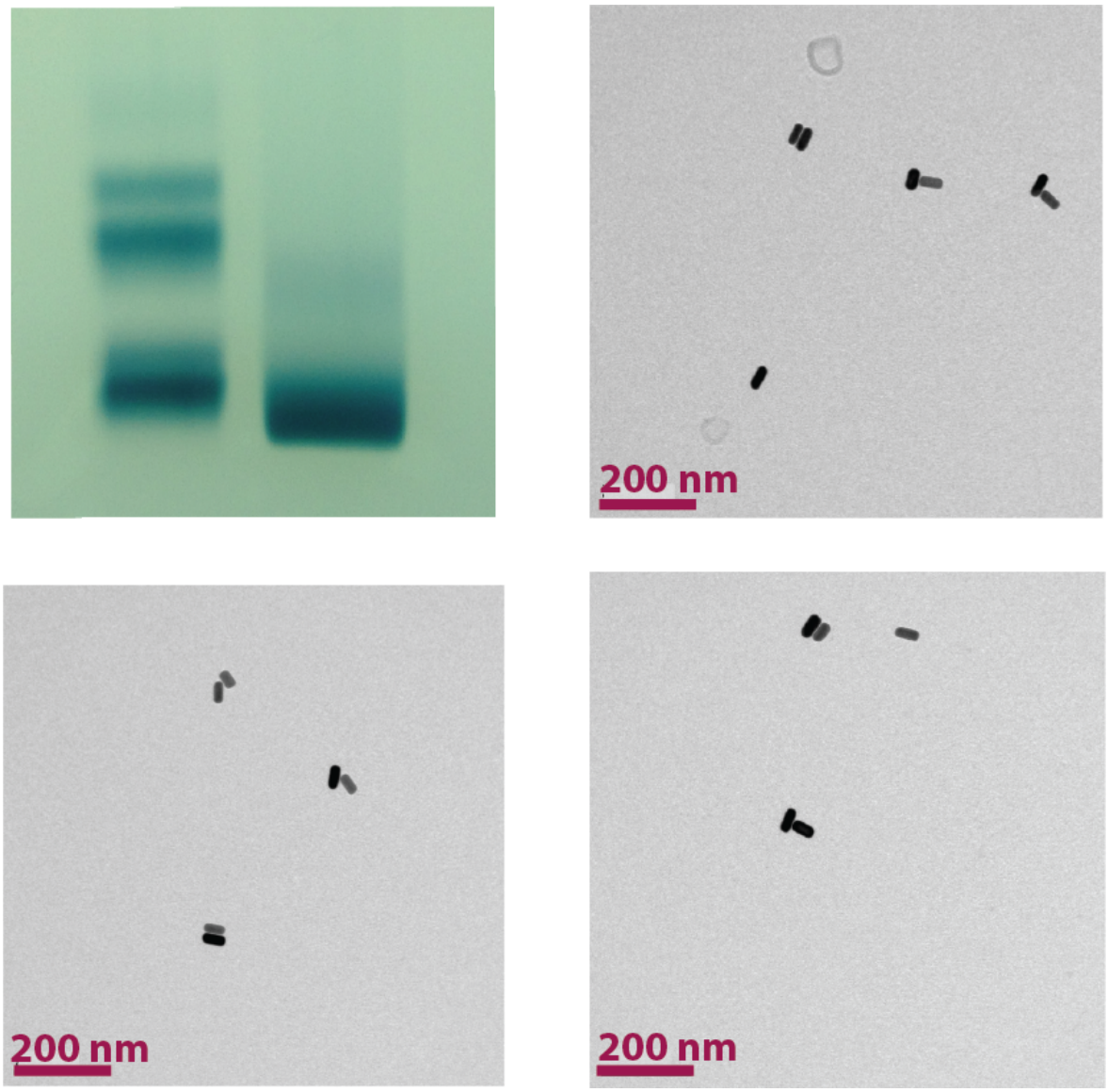

Figure 3.4: Nanorod dimers can be separated by gel electrophoresis.

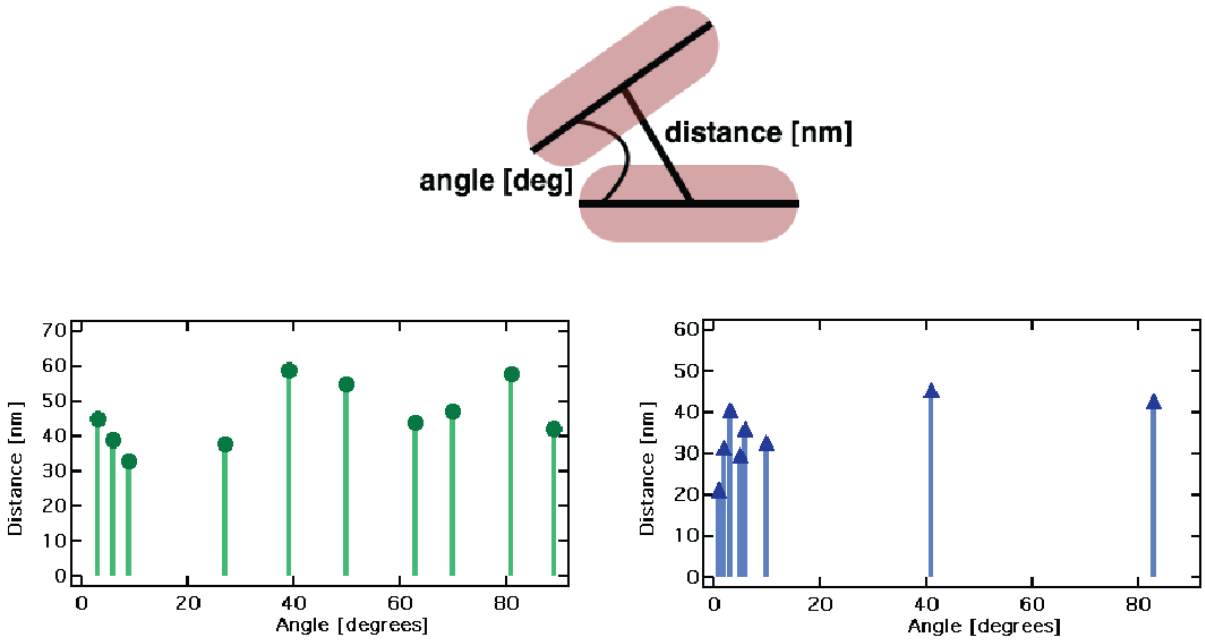

Figure 3.5: Nanorods connected with 63bp DNA (left) show no orientation preference by TEM analysis. Nanorods connected with 20bp DNA (right) show a highly enriched sample of side-by-side dimers.

$$\frac{\mu}{\mu_0} = \exp -\left(\frac{R_g}{a}\right)^2 \tag{3.1}$$

$$\mu_0 = \frac{Q}{\xi} \tag{3.2}$$

Mobility in agarose gel electrophoresis (Equation 2.1 depends on the free solution mobility (μ_0) as well as the radius of gyration (R_g) of the species and the pore size (a) [53]. Free solution mobility (Equation 2.2 depends on the charge (Q) and frictional coefficient (ξ) and is roughly constant ($2 \cdot 10^{-4}\, cm^2/V \cdot s$) regardless of length for DNA. Radius of gyration varies with the size and geometry of an object, as well as the object's flexibility or its ability to rearrange.

To separate gold nanorod structures the orientation of DNA attachment (side-by-side "isomers" from end-to-end "isomers"), DNA was designed to maximize the difference in radius of gyration of these assemblies. Double stranded DNA below the persistence length (50nm or 150bp) is considered a rigid rod. Prior research has shown [115], however, that the thiol attachment of oligonucleotides to nanoparticles provides significant rotational flex-

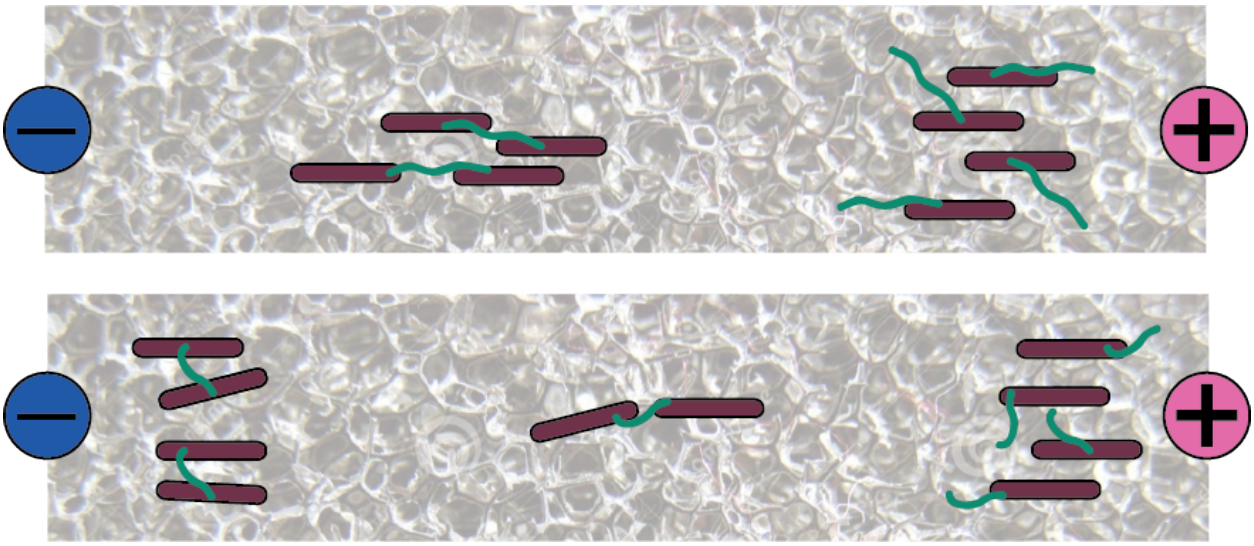

Figure 3.6: Particles move through gels with different mobility according to their radius of gyration.

ibility. Therefore, to limit the ability of DNA-assembled nanorods to rearrange in solution, the DNA linker should be shortened. To maintain the resolution of separation by HPLC, 60bp DNA strands were designed to overlap at 10, 20, and 30bp to decrease the distance between nanorods. Gel electrophoresis of the resulting structures reveals an additional band when compared with gels of nanorods connected by long (63bp) DNA. TEM analysis of this extracted band shows the population is highly enriched in side-by-side dimers (Figure 3.5).

A crude calculation of the radius of gyration of DNA-nanorod assemblies approximating the structures as completely rigid results in a larger R_g for end-to-end dimers, implying that isomer would be retained longer in a gel. However, in the limit of small pore size (estimated by Equation 3.3) and high electric field (7.5 V/cm), conditions are achieved for reptation in agarose gel electrophoresis. For a 2.5% agarose gel, the mean pore size is approximately 48nm in diameter, indicating that particles larger than this (R_g for a 20nm by 50nm cylinder is 50.1) are no longer separated by a sieving mechanism. Instead, DNA-nanorod assemblies are separated by their ability to move through the gel matrix in extended conformation, minimizing cross-sectional area. Side-by-side nanorods linked with very short DNA are unable to rearrange in this fashion, resulting in longer retention in the gel.

$$a \simeq \frac{89}{a^{2/3}} \tag{3.3}$$

To further characterize side-by-side nanorod dimers, UV-visible spectroscopy was used to probe their plasmon coupling. Nordlander's hybridization model predicts that side-by-side dimers will experience a blue shift of the longitudinal mode and a red-shift of the

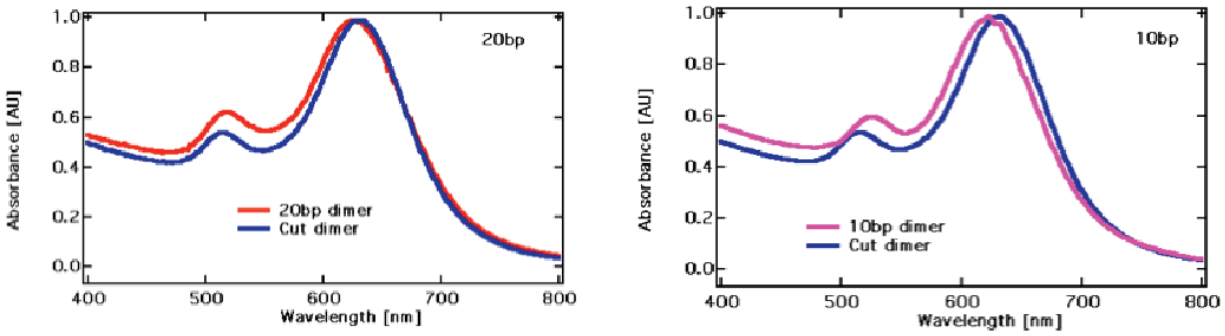

	transverse	longitudinal
20bp dimer	521nm	625nm
10bp dimer	525nm	621nm
monomer (cut)	513nm	631nm

Figure 3.7: Ensemble UV-visible spectroscopy of EcoRV cutting experiment demonstrates that nanorod dimers are a plasmon ruler.

transverse mode, while end-to-end dimers will experience the opposite [116]. Single particle darkfield spectroscopy of spin-coated nanorods correlated to SEM images has experimentally verified this predication [117, 118], as has single-particle spectroscopy on DNA origami-assembled structures [106] DNA oragami. Solution-phase coupling has been reported on electrostatically assembled arrays of nanorods [114, 119].

To ensure DNA was responsible for nanorod plasmon coupling, an EcoRV restriction site was programed into the DNA. This DNA cutting enzyme has been used previously in plasmon ruling experiments [15]. A purified sample of side-by-side DNA-assembled nanorods was transferred into a buffer containing 100mM NaCl, 50mM Tris-HCl, 10mM $MgCl_2$, and 100μg/mL BSA. Care was taken to remove EDTA from electrophoresis running buffer. After the acquisition of a UV-visible spectrum, one unit of EcoRV was added to solution and allowed to react at room temperature for one hour. An additional spectrum was acquired after one hour. As shown in Figure 3.7, DNA-mediated plasmon coupling was observed for 10bp and 20bp nanorod separations. Assemblies with longer DNA linkers did not demonstrate coupling.

3.4 Conclusions

Recent research has focused on the incorporation of anisotropic (non-spherical) nanoparticles to tailor more complex resonances in DNA-assembled structures. We recently demonstrated for the first time that gold nanorods can be assembled by the base pairing of single strands of DNA. We have control over the relative orientation of the nanorod pairs, creating a plasmon ruler in the IR for biosensing applications. To create orientation controlled DNA-assembled nanorods, oligonucleotides are conjugated to the gold surface of a nanorod via a $5'$ branched trithiol moiety. Singly conjugated nanorods are separated from other products using anion exchange HPLC. Complementary conjugates are reacted; dimers are separated using agarose gel electrophoresis. By carefully tuning the conditions of separation, a sample of gold nanorod dimers that are attached side-by-side can be isolated from those attached end-to-end. These oriented pairs can be cut using a DNA restriction enzyme, EcoRV, demonstrating their utility as an ensemble biosensor.

Chapter 4

Symmetry breaking in chiral plasmonic nanocrystal assemblies

4.1 Introduction

Self-assembly of nanostructures into three-dimensional entities creates nanoscale structures with unique properties that cannot be accessed lithographically [11, 120]. For nanophotonic applications, control of the shape and size of isolated nanoparticles produces a variety of building blocks with distinct optical signatures [24]. Control of the spacing and arrangement of these nanostructures relative to one another in turn produces collective effects with designable optical and electronic properties, including phenomena such as electronic coupling in cloaking devices, Fano resonances in plasmonic oligomers, and biochemical sensors based on aggregation [121–123]. Among the variety of possible molecular linkers to assemble these nanostructures, chemical linkers that reconfigure in response to specific external stimuli are intriguing as a route to tunable optical properties [124]. In self-assembled plasmon ruler structures, active changes in the distance between nanoparticles produce distinct spectra by modifying the coupling between nanoparticles, exploiting the sensitivity of plasmonic assemblies to spatial position for use as a sensor [14, 17]. The ability of specific three-dimensional, solution-phase assemblies to respond to external stimuli additionally lends itself to tunable and switchable optical metamaterial fluids.

Chirality is an attractive property for a number of nanophotonic applications, including negative index media, broadband circular polarizers, slow light applications, and enantioselective photochemistry [77, 78, 125–127]. In molecular systems, chirality is critical to many processes where only certain enantiomers perform specific functions. Many naturally occurring molecules such as amino acids and sugars possess handedness, and many synthetic pharmaceuticals are effective only as one enantiomer. Chiral molecules may also be used in asymmetric synthesis and catalysis [79]. Optically, chiral structures exhibit circular dichroism (CD), the differential absorption of left and right handed circularly polarized light.

Analogously to molecular systems, chiral plasmonic assemblies can be designed by controlling the spatial placement of nanoparticles in an assembly, as recently demonstrated in structures such as helices and pyramids [80–82, 128]. These nanophotonic chiral systems utilize plasmonic nanoparticles as artificial atoms with tunable resonances based on their size and shape. Unlike chiral plasmonic structures fabricated with substrate-based lithographic methods, these assemblies are freely rotating in solution and exhibit circular dichroism after integrating over all angles of incidence, similarly to molecules [83]. However, in contrast to molecular systems, these assemblies exhibit CD in the visible and near IR portion of the electromagnetic spectrum controlled by the resonant positions of the constituent nanoparticles. Furthermore, the figure of merit for chirality, defined as the ratio of the CD signal to the extinction, can be considerably larger than many molecules [129].

Here we discuss the design and synthesis of pyramidal assemblies of nanostructures with tunable and invertible CD by changing the distance between specific nanoparticle elements via symmetry breaking. Symmetry breaking reconfigures the structure of the assembly, producing a system that switches between enantiomers. Switchable chiral molecules based on temperature control, photoexcitation, and other mechanisms have been studied, and photoswitchable lithographic chiral metamaterials have recently been demonstrated [129–131]. In the self-assembled design presented here, plasmonic nanoparticles are assembled together using the programmable base-pairing of single DNA strands to create a pyramidal frame with plasmonic nanoparticles on the vertices [112]. As opposed to designs based on DNA origami, the distance between a pair of nanoparticles is controlled by the length of an individual double stranded DNA molecule that may be modified by specific external stimuli such as DNA-binding proteins. This design potentially allows for sensing of nanoscale distances by recording the handedness and peak positions of the CD spectrum while also describing a route toward metamaterial fluids with switchable handedness.

4.2 Design of chiral assemblies based on symmetry breaking

Chiral structures cannot be superimposed on their mirror image; consequently, chiral objects lack improper rotation symmetry. In pyramid assemblies as discussed here, asymmetry can be designed into the structure through the use of particles of different shapes, sizes, or compositions, or through the use of unequal interparticle distances [82]. A pyramid could be made chiral, for example, by placing four different size Au nanoparticles at the vertices of a pyramid with symmetric edge lengths (substitutional chirality), or by using four similarly sized particles with different pyramid edge lengths which break the mirror planes (configurational chirality) [80, 81]. It has recently been shown that in self-assembled pyramids the asymmetry induced by configurational asymmetry produces a more significant CD response than in substitutional designs due to more effective mirror-plane symmetry breaking [82].

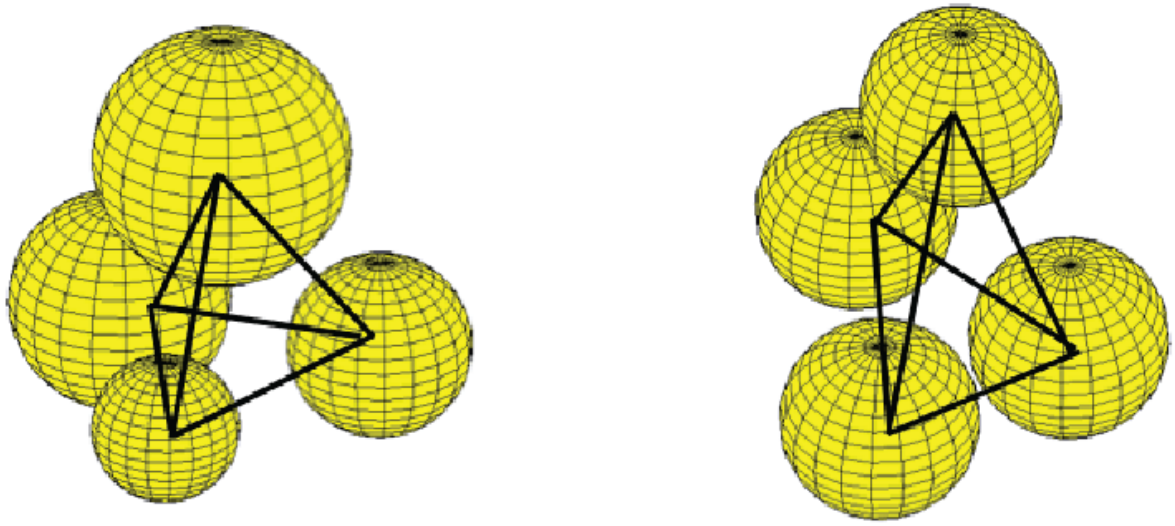

Figure 4.1: Substitutional (left) versus configurational (right) asymmetry in nanoparticle assemblies.

The design we present utilizes the principle of symmetry breaking to induce strong and tunable chirality in a pyramid assembly while simultaneously accounting for synthetic processibility. A schematic version of the chiral assemblies discussed here is shown in Figure 4.2, with straight lines depicting the DNA frame for clarity. On the left is an achiral pyramid where the pyramid frame is designed with equal edge lengths, and two different sizes of Au nanoparticles are attached to the vertices. This structure is not optically active as it contains mirror planes and therefore improper rotation axes. Chirality is induced by shortening one edge of the DNA frame to break the mirror planes, as depicted with the red arrow forming the middle schematic. Shortening the opposite arm creates the enantiomer, as shown in the second schematic of Figure 4.2. The magnitude of the CD signal is correlated to the degree of symmetry breaking: the greater the difference between the targeted edge length and the nontargeted edge lengths, the stronger the chiroptical effect.

To understand some of the advantages of this design, consider the synthetic process with more detail provided later. First Au nanoparticles of a given diameter (10 or 20 nm) are combined with thiol-modified DNA. This forms a statistical mixture of products, including unmodified Au nanoparticles, monoconjugated DNA-Au nanoparticles, and higher order oligonucleotide conjugates. The monoconjugated DNA-Au product is isolated from the solution using high performance liquid chromatography (HPLC) [34]. This procedure is repeated to create four distinct solutions of monoconjugated DNA-Au particles: two with 10 nm particles and two with 20 nm particles, each with a different DNA sequence. The solutions are combined in pairs (one 10 nm and one 20 nm fraction) and then into one mixture to form the final pyramidal structure. As depicted in Figure 4.2, each face of the pyramid is formed

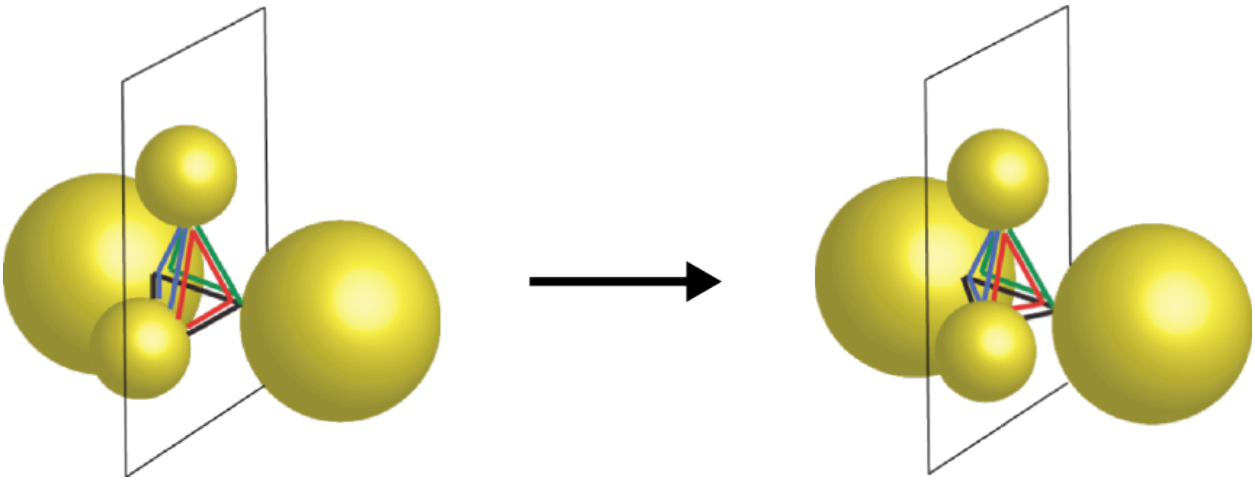

Figure 4.2: Left: achiral pyramid with two different sizes of nanoparticles and equal edge lengths. Shortening the blue-black edge produces the opposite enantiomer (right).

by one of the original DNA strands, which is complementary to a portion of the other three. The nanoparticles are located at the vertices of the pyramid, attached by a flexible thiolated linker.

The length of the base pairs is chosen to have an integral number of half helical turns per side. This makes the formation of pyramids with six unequal edge lengths challenging, as the structures must both be thermodynamically favorable and contain sufficiently small interparticle distances for effective plasmonic coupling. In the design presented here, only one edge of the pyramid frame needs to be of a different length from the other five, permitting the formation of more stable structures while preserving strong optical activity. This simple hybrid design thus accounts for both synthetic ease and functional optical response. Moreover, this design exhibits a straightforward and elegant method for tuning and inverting the chirality of the assembly. In the last section we show other pyramid designs which achieve tunability via symmetry breaking.

Sensitivity of Pyramids to Symmetry Breaking

To study the effect of symmetry breaking on this pyramid design, we first utilized a coupled dipole approximation simulation method with realistic parameters dictated by experiment, similar to the methods reported elsewhere [82, 132, 133]. The model fixes the dimensions of the DNA frame (10 nm on all edges except for the symmetry-breaking edge) and positions the nanoparticles off of the vertices of the pyramid as though they were attached by a linker molecule. As the distance is changed along the targeted edge it is kept fixed on the nontargeted edges, and the positions of the nanoparticles in space are recalculated for each new configuration. The nanoparticles are 10 nm and 20 nm in diameter, and the polarizability

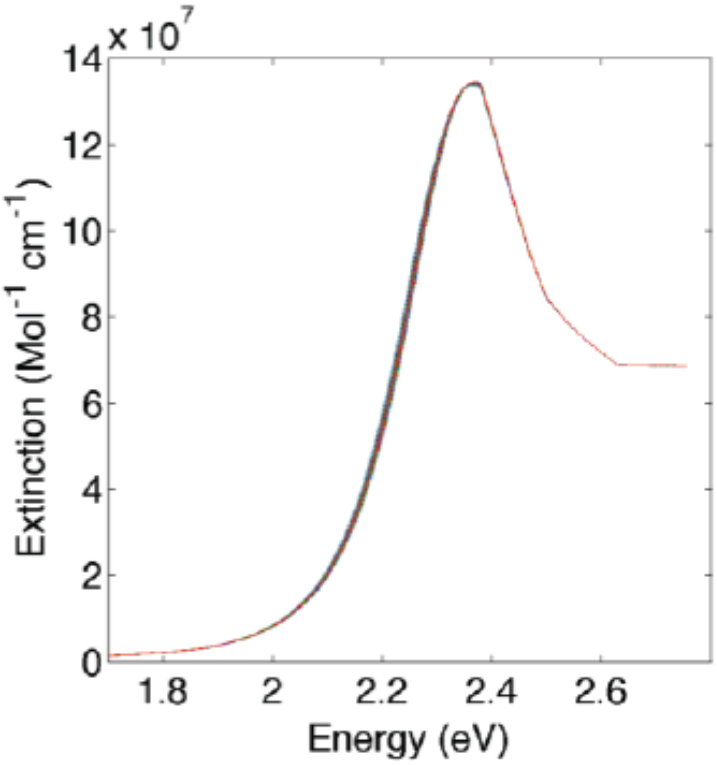

Figure 4.3: Extinction of pyramid calculated with circularly polarized light.

of each Au nanoparticle is modeled as a perfect sphere using Johnson and Christy data for the wavelength-dependent complex permittivity. The assemblies are assumed to be the wavelength-dependent complex permittivity [134]. The assemblies are assumed to be in water, as the refractive index of a low concentration tris buffer is not significantly different. We calculate the circular dichroism of the system as the difference in molar extinction under left and right handed circularly polarized light, integrated over all angles of incidence.

$$\sigma CD \propto \sigma LH - \sigma RH$$

The calculations account for the freely rotating pyramid in solution by rotating the direction of illumination over all of the possible angles, since this is mathematically equivalent to rotating the structure. We note that this is a significant design difference between self-assembled chiral assemblies and lithographically designed chiral structures, as the latter's handedness is typically dependent on the direction of illumination [83].

Figures 4.3 and 4.4 show the result of calculations of the extinction and circular dichroism of this pyramid design as the distance on the symmetry-breaking arm is changed. This is analogous to an experiment where an external stimulus such as a DNA binding protein

is targeted to a specific sequence on one edge of the pyramid, altering the length of that DNA linker. Given the small diameter of the nanoparticles used here, chosen for their synthetic purification ease, there is no significant degree of plasmon resonance coupling when monitoring extinction under circularly polarized illumination. There is a slight change in the intensity of the shoulder around 2.2 eV as the distance changes, but this difference would not be reliably detectable in experiment.

In contrast, Figure 4.4 shows the CD spectrum as the distance along the symmetry-breaking arm varies. Significant plasmon coupling as visible in extinction is therefore not a necessary prerequisite for plasmonic CD response: by detecting the difference between polarizations, CD is a more sensitive technique over this length scale than extinction. The CD spectrum exhibits a characteristic bisignate shape, falling mainly to the red of the plasmon resonance visible in Figure 4.3. The intensity of the CD spectrum increases as the distance of the symmetry-breaking arm is modified from the symmetric length of 10 nm, with the most intensity at the shortest distance considered here (6 nm). As plasmonic coupling scales with the distance between elements, it is expected that bringing the plasmonic nanoparticles closer together will produce a stronger response. Notably, the CD spectrum of the assembly switches sign when the targeted arm is shorter/longer than the symmetry length of 10 nm. Control calculations where the edge between nanoparticles of the same size is shortened, which does not break the mirror planes of the assembly, do not exhibit CD.

The spectral positions of the peaks in the CD spectrum are strongly dependent on distance, with the greatest shift in the spectral position occurring at distances close to the symmetric length of 10 nm. Changing the length of the symmetry-breaking arm from 10 nm to 11 nm, for example, changes the CD spectral peak position by 0.04 eV. As the edge becomes significantly shorter (or longer) than 10 nm, the spectral position dependence is weaker; changing the distance from 7 nm to 6 nm changes the CD spectral peak position by 0.08 eV. The structure therefore functions as a chiral plasmon ruler where the spectroscopic CD signal provides information about the nanoscale distances in the assembly.

The sign of the CD spectrum provides additional information about the nanoscale structure. Shortening the other symmetry-breaking edge of the pyramid to form the opposite enantiomer. The intensity and spectral position dependence on distance is identical, but here the sign of the CD spectrum is reversed. Interactions on different sides of the pyramid can be distinguished by the sign of the resulting CD spectrum. Thus by monitoring the intensity, peak spectral position, and sign of the CD spectrum, nanoscale information about the three-dimensional configuration of the pyramid can be determined.

Moreover, this pyramid design offers two simple routes to switchable chirality for application in sensing or designer metamaterials. In the first scheme, a pyramid could be designed with one long edge with a specific targeted sequence constructed into the DNA strand. In the presence of a targeted interaction, such as a DNA binding protein, the strand bends and

pulls the nanoparticles closer together than the nanoparticles on the nontargeted edges. In this fashion the chirality switches from one sign to the opposite, as shown in Figure 4.4. In the second scheme, an achiral pyramid with equal edge lengths could be constructed with different targeted sequences designed into the two arms highlighted in Figure 4.2. A targeted interaction which shortens one arm (red-black in Figure 4.2) produces one handedness, while a targeted interaction with the other arm (blue-black in Figure 4.2) produces the opposite. As the distances get shorter in both cases, both enantiomers will have strong CD response. This pyramid design thus represents a simple and flexible platform for both sensing of nanoscale structural information and switchable metamaterial fluids.

Tolerance to Structural Variations

The ideal self-assembled, tunable structure is one that shows dramatic changes in response to the desirable external stimulus, but is stable against small fluctuations in solution or fabrication imperfections. Here we consider the effects of a few common issues in colloidal self-assembly: polydispersity in the diameter of the metal nanoparticles, and distance fluctuations in the nontargeted arms. Stability against both of these parameters will be critical for application either as a three-dimensional sensor or as a switchable chiral metamaterial [133].

Figure 4.6 shows calculated CD spectra under different conditions that could affect experimental viability. Figure 4.6a shows the CD spectrum of a perfect pyramid, represented as a color map with length of the symmetry-breaking arm along the x-axis and energy along the y-axis. The bisignate nature of the spectrum is visible in the different colors, and the sign of the CD spectrum switches as the length of the targeted arm increases.

Figure 4.6b shows the same calculation considering polydispersity of the nanoparticle diameters. For each simulation, nanoparticle diameters were chosen from a normal distribution assuming 10% standard deviation and a mean size of either 10 nm or 20 nm. This distribution is comparable or larger than we observe experimentally in our nanoparticles. Experimentally, the position of each nanoparticle within the assembly is determined by the initial DNA conjugation step, so smaller particles and larger particles will occupy the same positions on the pyramid without mixing. Each indvidual pyramid will form with a particular set of nanoparticles and then undergo changes in the arm length. Therefore for each set of nanoparticles chosen from the distribution, the full calculation with varying distance along the targeted edge and integration over all angles of incidence was performed. This procedure was repeated 50 times and averaged to produce Figure 4.5b.

As can be seen by comparing Figure 4.5a and 4.5b, polydispersity of nanoparticle diameters does not have a significant effect on the CD tunability with symmetry breaking. The intensity of the CD spectrum depends strongly on the diameter of the nanoparticles at these distances, increasing substantially with larger particles. Even if the nanoparticle diameters

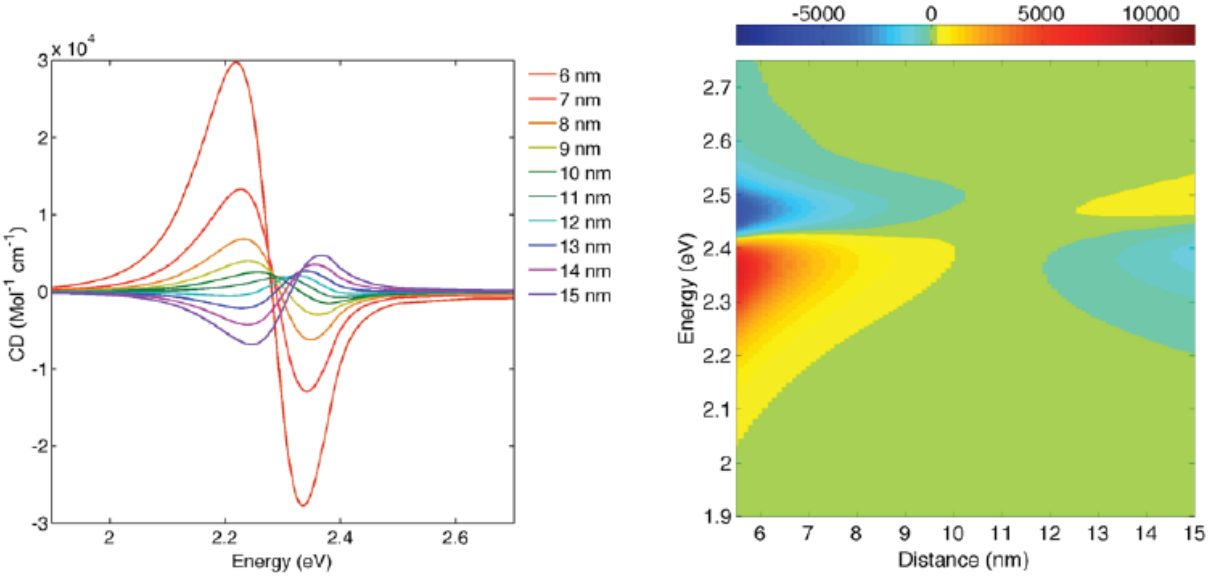

Figure 4.4: Circular dichroism spectra with increasing length of the symmetry-breaking arm.

are chosen to be closer together with some overlap in their distributions, such as 10 nm and 15 nm, a sufficient number of pyramids in the set have the correct handedness and the CD spectra are not significantly noisier. Polydispersity of nanoparticle diameter is thus not expected to significantly impact the optical design.

The distance along the nontargeted arms, and particularly the flexible linker between the DNA and the Au nanoparticle, will also vary, and Figure 4.6c shows the result of calculations considering these fluctuations. The distances on the nontargeted sides are chosen from a normal distribution with a mean length of 10 nm and a standard deviation of 1 nm. In this calculation, a single pyramid is assumed to be constantly fluctuating while the distance on the targeted arm is modified in response to the stimulus. Therefore at each specified distance of the targeted arm, five different edge lengths are chosen randomly from this distribution. This procedure is repeated 50 times and averaged in Figure 4.6c. The main features of the symmetry breaking pyramid design are preserved when considering distance fluctuations, although there is more variation than in the polydispersity calculations. The sign of the handedness inverts as the targeted arm's length is changed, the peak spectral positions of the CD spectrum shift similarly to those in Figure 4.6a, and the intensity of the CD spectrum is highest for the shortest edge length. Since in a realistic experiment these fluctuations will occur rapidly and will include many more than 50 variations, we conclude that this design is relatively stable against nonspecific modifications.

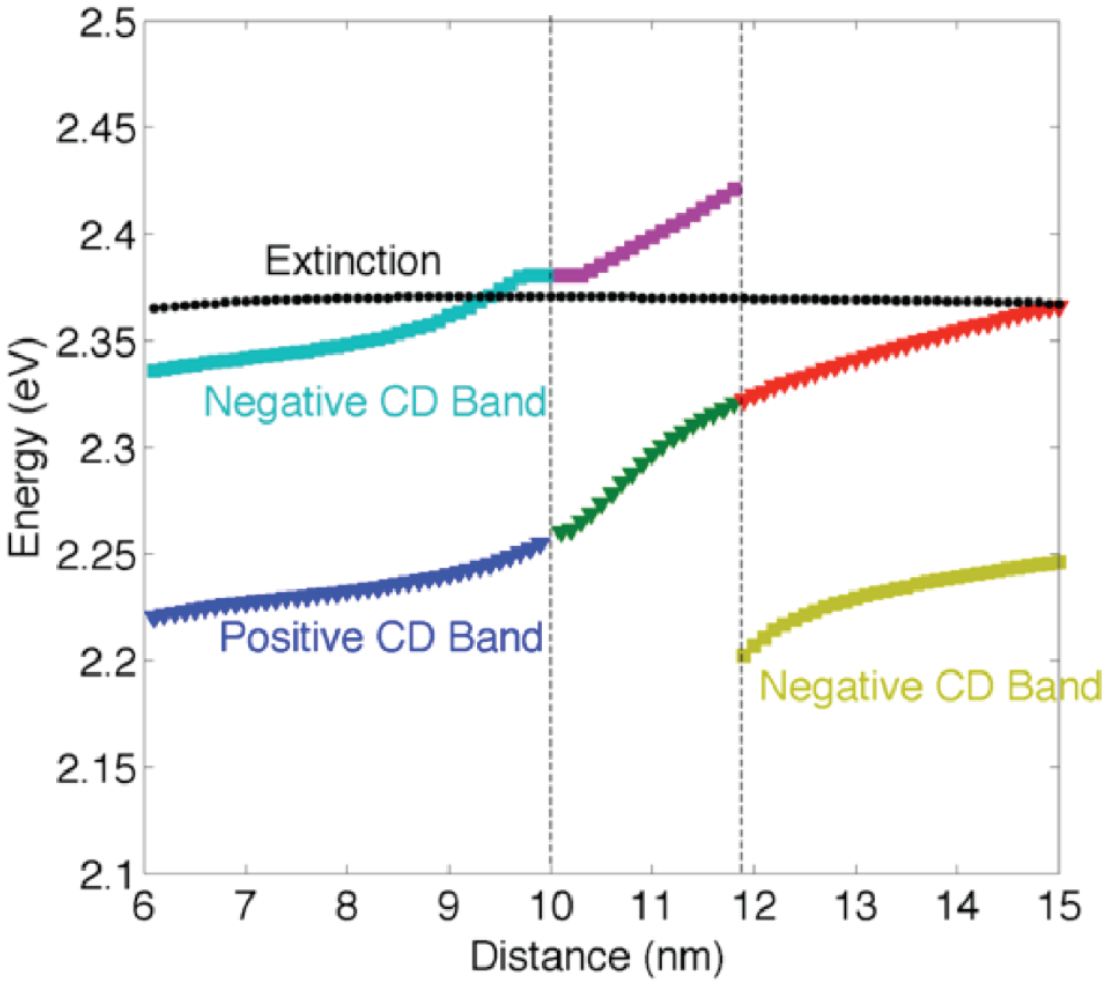

Figure 4.5: The frequency of the positive and negative CD band changes along with the intensity. The extinction doesn't change dramatically.

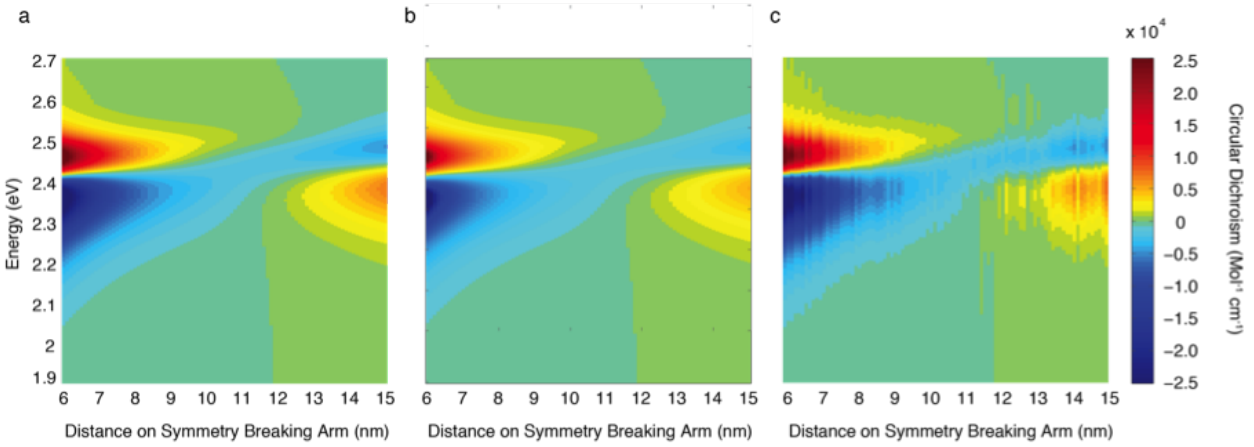

Figure 4.6: Calculations of CD spectra with imperfect fabrication. a: "perfect" pyramid with 10 nm and 20 nm particle sizes and all non-targeted arms fixed at 10 nm. b: pyramid including polydispersity in nanoparticle diameters. c: pyramid including fluctuating distances on nontargeted arms. The calculations in b and c are averaged over 50 iterations.

Symmetry Breaking with Other Geometries

There are other symmetry-breaking geometries that may be designed to produce tunable and invertible CD spectra with other advantages such as higher figures of merit and broad spectral response. The structure designed and fabricated above uses two different sizes of Au nanoparticles to break the mirror planes as the distance on one targeted edge is changed. The symmetry could also be broken using two different shapes of particles such as solids and core-shell particles, or two different metals such as Ag and Au as depicted in the inset of Figure 4.7a. While the surface chemistry techniques utilized here are primarily designed for Au, it is also possible to conjugate discrete numbers of oligonucleotides to Ag nanoparticles [51]. Figure 4.7 shows the calculated spectra for this assembly with distance changing along one targeted edge and the nontargeted edge lengths fixed at 10 nm. The resulting CD spectrum exhibits bisignate shapes around both the Au nanoparticle resonance at 2.4 eV and the Ag nanoparticle resonance at 3.1 eV. The chiral features around the Ag resonance are more intense, as has been observed in plated Ag assembled structures [128]. This structure also exhibits broad spectral tunability as the distance changes along the symmetry breaking arm, tuning the chirality and changing handedness at several different spectral positions.

The second part of Figure 4.7 shows another chiral pyramid based exclusively on configurational asymmetry. The framework of the pyramids are shown as schematics for clarity; the actual calculation includes 20 nm gold particles attached at each vertex. The chirality in this system derives from the unequal edge lengths. Side a is the targeted edge of the pyramid and is the only side to change length. Here we chose three of the non-targeted lengths to be

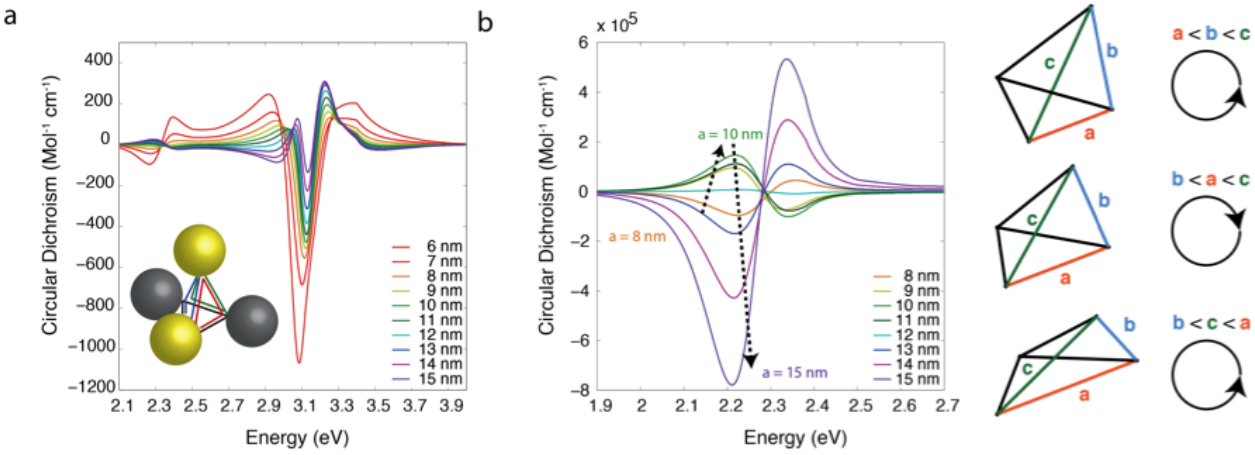

Figure 4.7: Calculations of more complex pyramids with tunable chirality based on symmetry breaking. a: Symmetry breaking pyramid design with Au and Ag nanoparticles. The distance between one Au particle and one Ag particle is shortened (red-black edge) while the others are fixed at 10 nm. b: Configurational pyramid where all the particles are 20 nm in diameter. The edge labeled a changes distance, three edges (black) are 10 nm, one edge (b) is 8 nm, and one edge (c) is 12 nm. As a changes length, the sign of the CD signal inverts and then inverts back again, as depicted in the schematics and with the arrows in the calculated data.

10 nm (black lines), one edge to be shorter by approximately one half helical turn (8 nm, labeled b), and one edge to be longer by a half helical turn (12 nm, labeled c). As the length of side a changes from a ¡ b to a ¿ b, the sign of the CD spectrum switches, with the order of increasing length on one face of the pyramid changing from counter-clockwise to clockwise as depicted in the figure. As edge a increases further in length such that a ¿ d, then the sign of the CD signal switches back to the original sign.

4.3 Synthesis and characterization of pyramids

To verify the predictions of our model, we synthesized nanoparticle pyramids on a DNA scaffold. Programmed strands of DNA have been previously shown to fold into tetrahedral pyramids [135]. By taking into account the sterics of the three DNA double helices that converge at each vertex, one diasteriomer of the DNA tetrahedron can be produced in large excess over the other. DNA structures with distorted tetrahedral geometries have also been synthesized. Confirmation of the stereoselectivity of this assembly process was achieved through molecular biology techniques as well as cryo electron microscopy [136, 137].

By this principle, a tetrahedral DNA scaffold comprised of four oligonucleotides, each

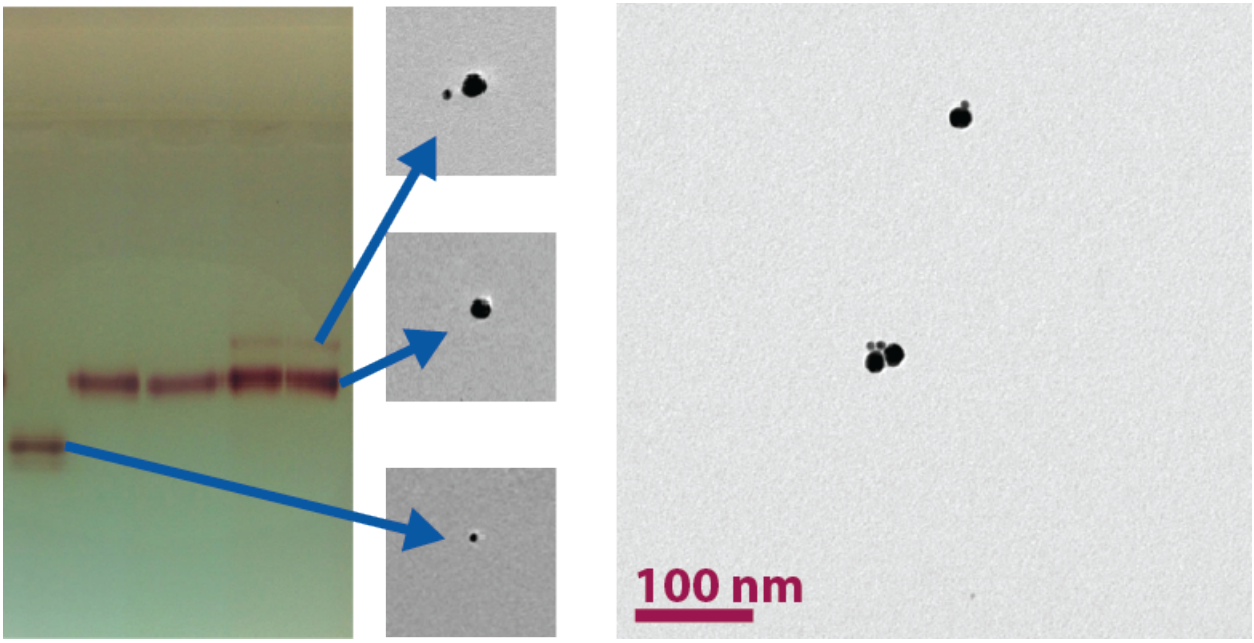

Figure 4.8: Agarose gel electrophoresis separation of dimers formed by ten nm and twenty nm pairwise reactions. The TEM images show the makeup of each band. (left) Large area TEM image showing formation of four-nanoparticle assemblies. (right)

tracing a face of the pyramid, was conceived to create chiral assemblies of gold nanoparticles. DNA structures incorporating one shortened side were designed using the same methods as previously reported [112]. Sequences were designed such that each side of the tetrahedron was sufficiently long and GC-rich to remain stable, to prevent DNA fraying at room temperature, and to minimize undesirable secondary structures. Between each side of the pyramid, three thymine bases are included to allow sufficient flexibility for the three double helices to converge at each vertex. All oligonucelotides were modified with a 5' branched tri-thiol moiety and were purchased from Fidelity Systems, Inc. The sequences are provided in Appendix 4.

Gold nanoparticles of 10 and 20 nm diameter were then ligand exchanged, combined with the oligonucleotides, and ligand exchanged with PEG to provide stability at high ionic strength conditions as has been described previously [51]. Key to the formation of discrete pyramids is the ability to separate nanoparticle-DNA conjugates by the number of conjugated oligonucleotides, which we accomplish through anion exchange HPLC [34]. The column packing contains polymer beads displaying a quaternary ammonium moiety. When nanoparticle-DNA conjugates pass through the column, the strength of their interaction with the beads is enhanced substantially by the addition of a single oligonucleotide. As a result, the separation between a nanoparticle attached to no DNA (the first peak to elute) and a

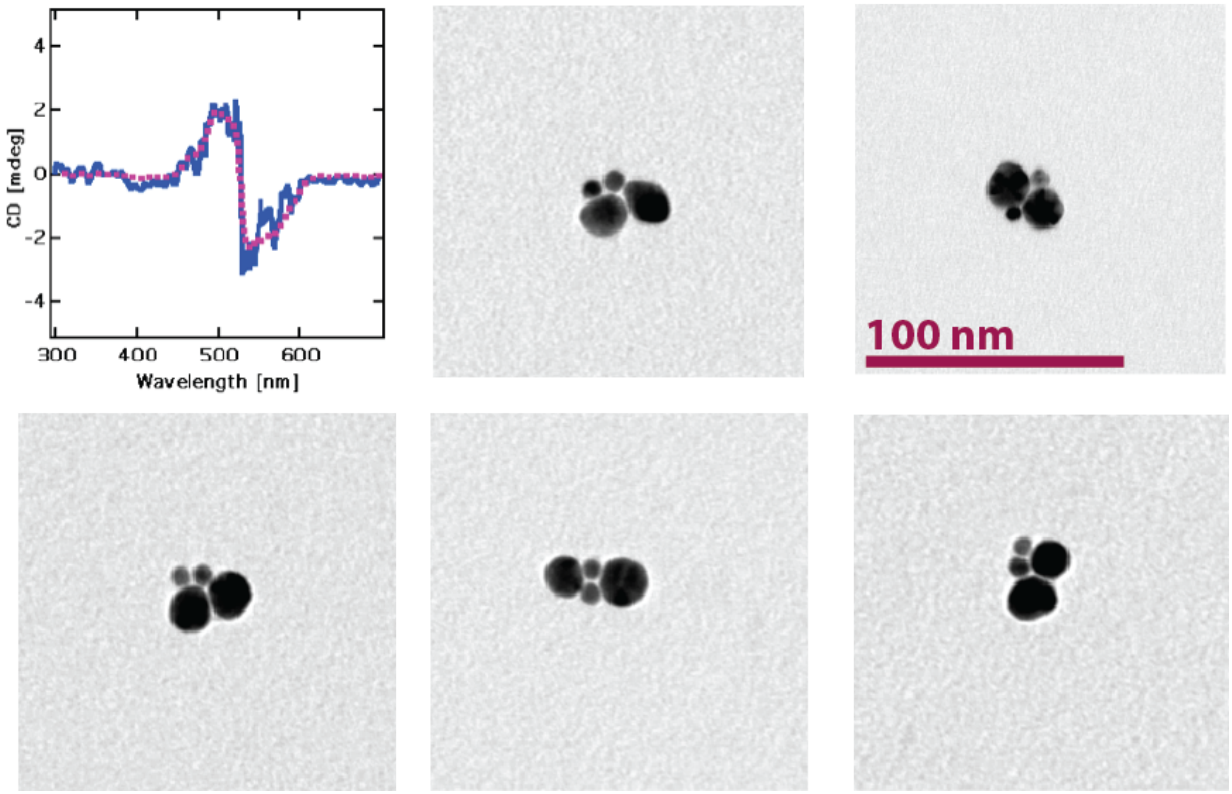

Figure 4.9: Measured CD spectrum of pyramids including one shortened edge. TEMs show 2D projections of 3D structures.

nanoparticle attached to one DNA molecule (the second peak) can approach baseline. Particles attached to two or more DNA molecules have higher mobility on the column, but with a decreasing effect, causing a shoulder on the monoconjugate peak of the chromatogram.

To create pyramid assemblies in high yield, the purified conjugates were combined in a stepwise scheme. The 10 nm and 20 nm conjugates were paired, allowed to react overnight, and separated electrophoretically as shown in Figure 4.8. On the gel above, the 10 nm-20 nm dimers correspond to the band that's furthest retained in the agarose gel matrix. TEM images extracted from each band are shown next to the photograph in Figure 4.8, indicating that the other bands consist of single nanoparticles. The extracted 10 nm-20 nm dimers were combined stochiometrically as determined by their extinction at 520 nm and allowed to react for 48 hours. Assemblies were characterized using UV-Vis, TEM, and CD spectroscopy. A representative TEM from the final assembly step is shown in Figure 4.8, indicating that groups of four nanoparticles formed via assembly.

We then characterized the ensemble chiroptical response of these assemblies using circular dichroism spectroscopy, shown in Figure 4.9. These pyramids exhibit the characteristic

bisignate shape of CD with the primary activity in the spectral range from 2.3-2.4 eV near the Au nanoparticle resonance. To achieve sufficient product volume for measurement, the pyramids were not purified from the lower order structures after the dimers were combined. The noise in the spectrum is thus possibly due to lower-order, achiral structures present in the solution that attenuate the source. The data is shown as change in extinction in cm-1 rather than molar extinction, converting to molar extinction requires the concentration of the solution. We know from UV-Vis measurements that the total concentration of the solution is approximately 0.1 M, but the concentration of the chiral pyramids within the solution is not known. If 100% of the solution consisted of pyramids, then the measured CD is lower than the predicted CD by two orders of magnitude. However, it is likely that the fraction of pyramids within the measurement solution is actually considerably lower, reducing the differences between experiment and simulation. We note that the lower magnitude of experimental CD compared to predictions has been observed by others[81].

Experimental

Gold nanoparticles with 10 and 20 nm diameter were purchased from Ted Pella. Before DNA conjugation, the particles were ligand exchanged overnight with .25mg/mL Bis(p-sulfonatophenyl)phenylphosphine (Aldrich) then centrifuged to a concentration of 1 uM as determined by extinction at 520 nm. The four oligonucleotides were allowed to react with nanoparticles overnight in a high ionic strength solution. Three hours prior to separation, nanoparticle-DNA conjugates were ligand exchanged with a short chain PEG (Polypure) solution to a final concentration of 1 mM. This thiolated PEG molecule forms a dense self-assembled monolayer on the surface of the nanoparticles, allowing nanoparticle solutions to remain stable at the high ionic strength conditions required for separation. Nanoparticles were separated according to the number of conjugated oligonucleotides by anion exchange HPLC on a Dionex DNAPac PA-100 nucleic acid column. All gels were 2% agarose run in .5x tris-borate-EDTA (TBE) buffer at 15.6V/cm. CD spectra were measured on a Jasco J-815 circular dichroism spectropolarimeter.

4.4 Conclusions

The chiral plasmonic assemblies described here are designed using symmetry breaking principles to tune and invert the CD signal. We have shown that through a simple design, the spectral position, intensity, and sign of the CD signal may be tuned or switched as one edge of the pyramid is shortened, as occurs in the presence of specific targeting external stimuli. This makes the chiral pyramid an effective plasmon ruler, capable of detecting small changes in nanoscale structure at longer distances than are observable in extinction. Moreover, this design provides a simple route to switchable fluid metamaterials, where the reconfigurability of the assembly switches the handedness.

Chapter 5

Electron microscopy of DNA-assembled gold nanoparticle dimers

Gold nanoparticles assembled by double stranded DNA have long been characterized by transmission electron microscopy (TEM) [9, 33, 112]. Through image analysis, TEM can reveal information about DNA-assembled nanostructure yield and morphology [60, 138]. Practitioners of nanoscience have largely characterized DNA-nanoparticle structures by drying samples out on TEM grids. When TEM is performed on these samples, the structural information has been shown to be significantly distorted from their native conformation due to the presence of capillary forces between the nanoparticles [138]. Additionally, since DNA is electron transparent under these conditions, connectivity has largely been determined statistically, not by direct observation. In order to glean more information about these assemblies, they were observed by the grapheme TEM liquid cell developed by the Alivisatos lab and by the individual particle electron tomography (IPET) technique developed by Ren and coworkers.

5.1 Synthesis of gold nanoparticle dimers

Gold nanoparticle-DNA assemblies were synthesized by a similar procedure for both electron microscopy experiments. Single stranded DNA was conjugated to gold nanoparticles and the particle surface was passivated with a neutral short chain PEG ligand. Monoconjugates were separated by HPLC, reacted overnight, then dimers were separated by gel electrophoresis. To achieve maximum yield, dimers were stored at 4^oC and used within 48 hours.

Preparation of gold nanoparticles.

Gold nanoparticles were purchased from Ted Pella, Inc (Redding, CA) with average diameter 5.5nm with less than 10% deviation. These stabilizing citrate ligands on these particles were exchanged with bis-(p-sulfonatophenyl) phenylphosphine (BSPP) from Strem Chemicals, Inc (Newburyport, MA). To a flask of 100mL of nanoparticles, .25mg/mL BSPP was added and allowed to stir at room temperature overnight. The nanoparticles were aggregated with .02g/mL NaCl and centrifuged at 4,000rpm for 15 minutes. After removal of the supernatant, the nanoparticle pellet was resuspended in approximately a milliliter of a 5mg/mL aqueous BSPP solution. The concentration of the nanoparticles was determined by absorption at the gold nanoparticle plasmon coupling maximum of 520nm.

Conjugation of DNA to gold nanoparticles.

DNA thiolated at the 5' end was purchased from Fidelity Systems, Inc (Gaithersburg, MD) was resuspended in buffer (10mM Tris pH 8, .5mM EDTA). Nanoparticles and DNA were reacted at a stoichiometric ratio of 1:2. In a typical reaction, an appropriate volume of 100uM DNA was added to 90uL of nanoparticles in the presence of 50mM NaCl and 2mM BSPP. This reaction incubated for 24 hours at room temperature, then 1/10 volume PEG solution (1 μL hydroxy-terminated thiolated PEG, MW 356.6 (Polypure, Oslo, Norway) in 50 μL ddH2O) was added and incubated for an additional 3 hours. The result is a statistical mixture of products from which monoconjugates can be purified.

Separation of DNA-Au monoconjugates.

Monoconjugates were separated from other reaction products by anion exchange HPLC. On an Agilent 1100 series HPLC, nanoparticles were applied to a a Dionex DNA-Pac PA100 anion exchange column (Sunnyvale, CA). Samples were eluted by NaCl gradient (40 mM to 900 mM over a period of 20 minutes), detected by absorption at 520nm. Collected fractions were diluted 5x and concentrated to 20uL by Amicon Ultra spin filter, MW 100,000 (EMD Millipore Corp, Billerica, MA).

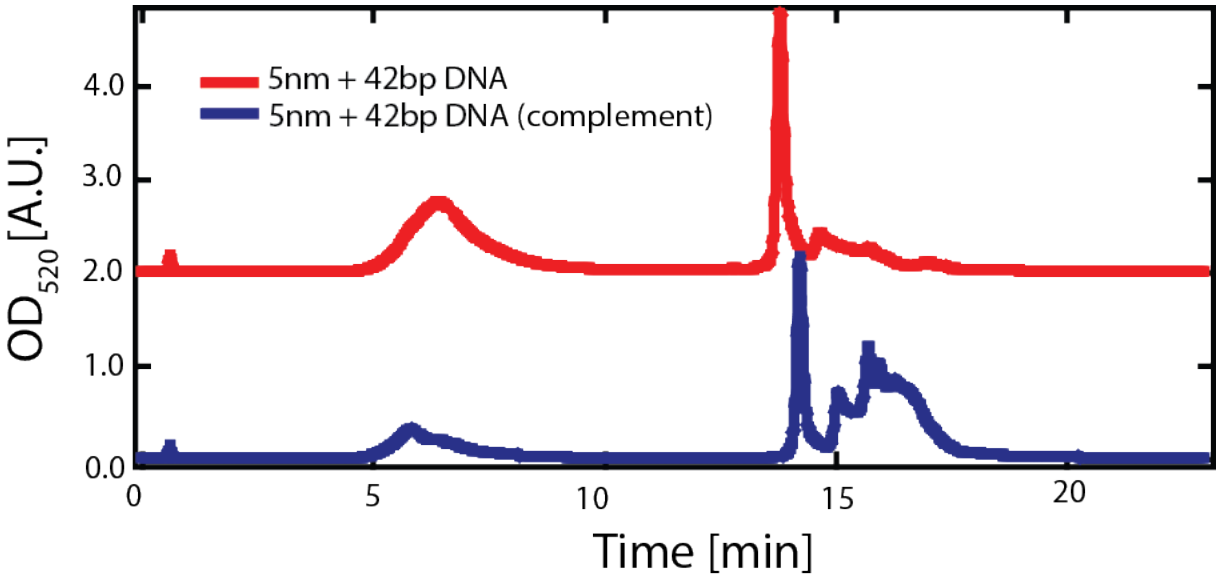

Figure 5.1: Anion-exchange HPLC allows baseline separation of bare gold nanoparticles from those conjugated to a single strand of DNA. In these example chromatograms, the small peak that elutes before 1 minute is the solvent front, the peak at 6 minutes is unconjugated gold nanoparticles, the sharp peak at 14 minutes corresponds to gold nanoparticles conjugated to a single strand of DNA, and the following peaks indicate higher order conjugates.

Preparation of dimers from monoconjugates.

Conjugates were combined stoichiometrically as determined by optical density at 520nm and allowed to react overnight at room temperature. The dimers were purified from unreacted monoconjugates by agarose gel electrophoresis. Briefly, dimers solutions were applied to a slab agarose gel (3% w/w) in a running buffer of 45mM Tris-borate and .5mM EDTA and run at 7.5 V/cm along with appropriate monoconjugate controls. Dimer bands were extracted from the gel with a clean razor blade. DNA-assembled nano structures were extracted by inserting the excised gel into dialysis tubing (SnakeSkin dialysis tubing, MWKO 10K, Thermo Scientific) along with 1mL of running buffer. After extraction from the agarose matrix, the dimers were characterized by TEM.

DNA sequences.

DNA sequences obtained from Fidelity Systems, Inc (Gaithersburg, MD) were 5′ thiol modified and PAGE purified.

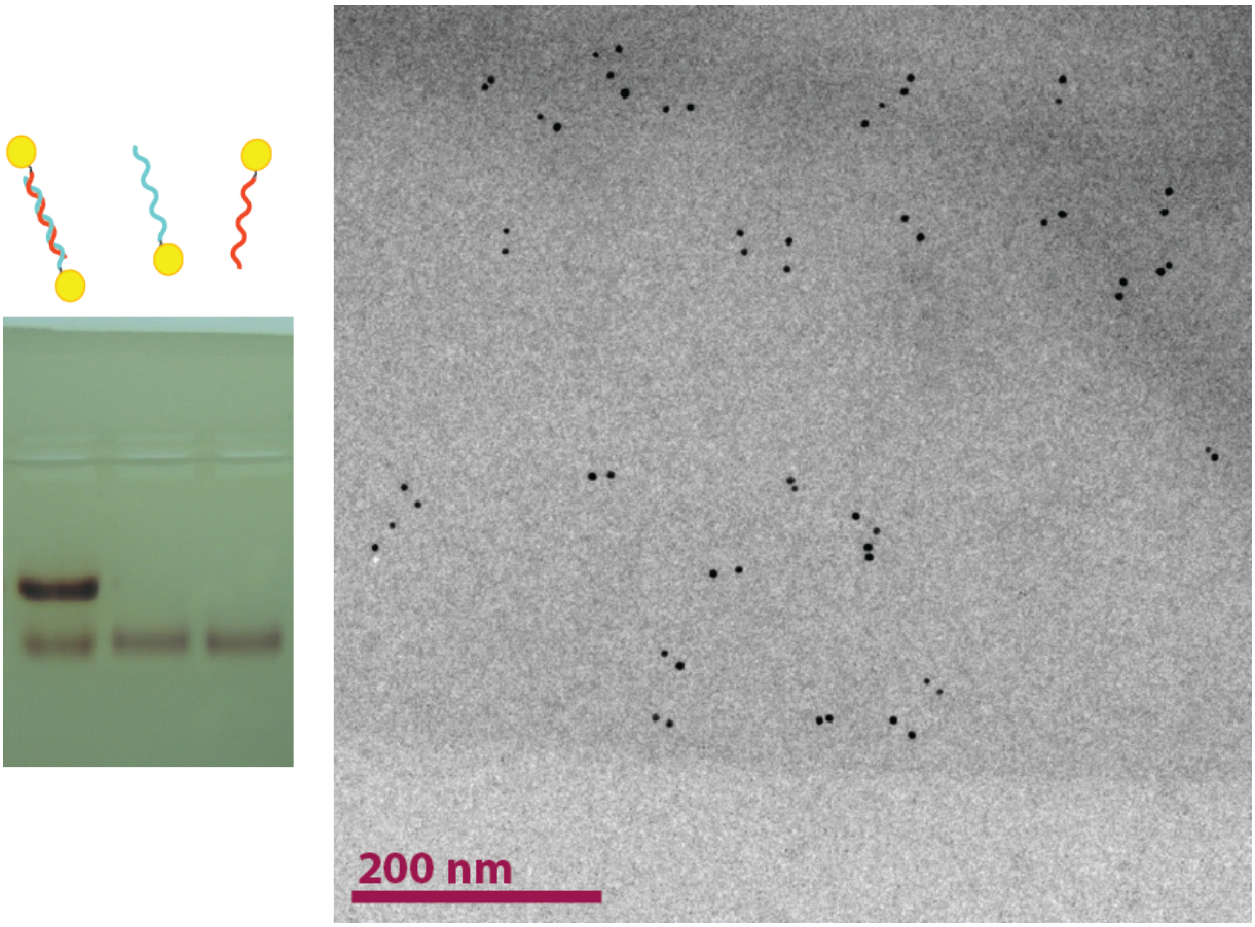

Figure 5.2: Gold nanoparticle dimers can be separated from reaction products by gel electrophoresis. These samples are drop cast on a carbon-coated copper grid and characterized by TEM for yield. When dried and imaged at an acceleration voltage of 200KV, the DNA connecting these nanoparticle dimers is not observed.

5.2 In Situ graphene liquid cell

A significant challenge in microscopy has been to visualize the dynamics of soft materials, in particular biological systems [139–145], at the nanoscale in order to confirm or extend the extensive insights predicted by molecular theory and simulation [146–148]. One strategy followed in the electron microscopy community is to obtain high spatial resolution snapshots from distinct members of an ensemble of artificially fixated samples in their native liquid environment, each sample exhibiting one stage in a dynamic process [140, 146]. Later these snapshots are assigned by the observer to a proposed sequence, and then merged into a continuous dynamic movie. TEM achieves highly resolved structural details from the laborious sample preparations of a system frozen in vitrified ice [140]. Super resolution optical

microscopy can either obtain such stationary snapshots or continuous frames of images with a record resolution of approximately 15 nm [145, 148], but for solely the spatial distribution but not structural and morphology details. Emerging liquid cell TEM techniques [19, 149–157] have the potential to capture dynamic events in real -time by interfacing ultra-thin specimens in their native liquid phase with the high-resolution capabilities of EM. Previous studies using different versions of such liquid cells have not yet provided a real time trajectory of aqueous bio-molecules due to many challenges [139–143]: the poor contrast of the low atomic number elements abundant in biological samples, the sensitivity to radiation damage, and the leaking of low vapor pressure solvent from the liquid cells. Because of these challenges, previous studies of biological systems using different versions of these liquid cells emphasize maintaining a hydrated environment during the imaging [158–164].

Here we use a novel graphene liquid cell for transmission electron microscopy recently developed in this laboratory [19]. The unique design and materials property of the graphene liquid cell [19, 163, 165] promise to tackle the previously identified challenges. The single atom thick graphene layer, the strongest and thinnest possible membrane, minimizes unwanted loss of the imaging electrons by a window material and provides superior contrast and resolution compared to the conventional Si_3N_4 windows used in other liquid cell techniques [19]. In the graphene liquid cell, a pocket of approximately 100 nm peak height [19] and 1 micron diameter is trapped between two extended graphene sheets which are bonded to each other by their van der Waals attraction in the region where the liquid is not trapped. Unlike the artificial adhesion from the spacers in other liquid cells [150–158], this strong native attraction minimizes potential contaminations and leakage during sample preparation procedures. The high electron and thermal conductivities of graphene enable fast transfer of accumulated charges or heat from electron beam, and is therefore a promising system to lower radiation damage to a biological sample. Note that this experiment can be done on a conventional TEM microscope without modification or customization of the TEM itself or the TEM holder.

We choose to study real-time dynamics of dsDNA conjugated with Au nanocrystals using a graphene liquid cell TEM for two reasons. Au-DNA nanoconjugates have been widely used as dynamic plasmonic probes [16, 17, 112, 115, 166] correlating an optical shift to a change in configuration due to a localized environmental stimulus. The direct imaging of their 3D configuration and the transformative process will enable on-demand design of such assembled sensors. This DNA assembled nanostructure incorporates both a biological molecule (the linker dsDNA) and a hard inorganic material (the high contrast Au nanocrystal) in TEM imaging. The presence of dsDNA molecules incorporates the major challenges of studying the dynamics of biological samples with TEM, and in our experiment demonstrates the potential of the graphene liquid cell technique for studying the dynamics of biological samples with liquid phase TEM. The high-contrast Au nanocrystals, on the other hand, facilitate tracking of our specimens. In addition, their motions at the single particle level shown below allow us to infer the configuration and status of DNA molecules under the electron beam.

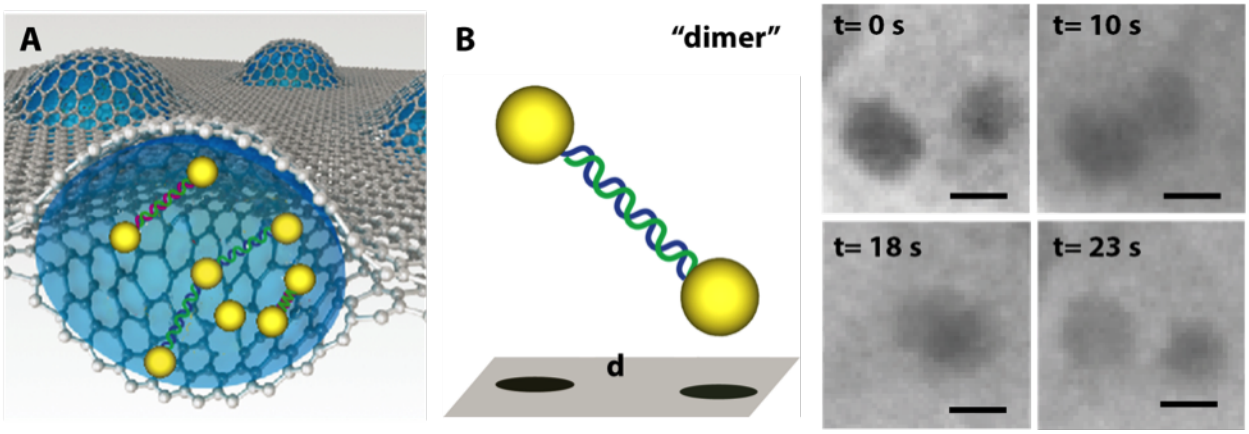

Figure 5.3: Graphene liquid cell imaging of Au nanocrystal-dsDNA nanoconjugates. (A) Schematic of a graphene liquid cell with multiple liquid pockets, containing dimers composed of dsDNA bridges in different lengths, and trimers. (B) Schematic of a dimer and its projection as two dark circular shapes onto a planar TEM imaging surface. (C) TEM images (center positions aligned) of a rotating dimer. At t= 18s, the two projected particles overlap with each other, indicating the dimer is almost perpendicular to the viewing screen. Scale bar is 5 nm.

In particular, we observe dimers (pairs of gold nanoparticles tethered by a single piece of dsDNA), and trimers (three gold nanoparticles connected into a linear configuration by two single piece of dsDNA bridges).

Experimental strategy to probing the motion of Au-ds DNA nanoconjugates

In our previous report of graphene liquid cell EM (12), we encapsulated an ultrathin layer of organic nanocrystal growth solution and achieved ultra-high resolution of in-situ Pt nanocrystal growth TEM imaging. Here, we use an aqueous solution which is more evaporative. The strong van der Waals attraction between two graphene membranes successfully seals specimens in aqueous phase while capillary force induced by its evaporation brings the top and bottom graphene layers in conformal contact. Stable aqueous solution pockets around one micrometer in size are rendered from this sealing mechanism, allowing for continuous imaging of the motion dynamics up to 2 minutes when exposed to the imaging electron beam accelerated by 200 kV.

The moving Au-dsDNA nanoconjugates in liquid are captured, under optimized imaging conditions (see Materials and Methods), as clusters of dark circular shapes projected onto the camera mounted in the TEM. For example, the projections of two component Au

nanocrystals of a dimer fluctuate in their distance; at certain instances, they even overlap and then diffuse slightly apart (Scheme 1C). The transient overlapping of two close nanocrystals indicates that the 3D rotation of the dimer is a significant component in the fluctuation of the distances between projections of particles in addition to a possible contribution from the linker DNA length fluctuation. This 3D rotation of the dimer demonstrates the thickness of the liquid pockets allows sufficient space for such rotation of 20 nm size clusters, and the graphene membrane does not perturb dynamics of Au-dsDNA conjugates by substrate-nanocrystal attraction. It is noteworthy that localized substrate attractions with nanocrystal from other types of window materials such as Si_3N_4 (17) have confined the particle motion in liquid and render little observation of 3D dynamics.

The correlated motions

First, we observed the motion of various types of Au-dsDNA conjugates, in the same liquid pocket to maintain the same physical condition for reliable quantitative analysis. The liquid pocket encapsulates differently designed configurations: Au-single strand DNA, short Au-dsDNA-Au (42 base pair DNA), and long Au-dsDNA-Au (84 base pair DNA), resulting in different dynamic features. Figure 5.4A shows a collection of 2D projected trajectories for those nanoconjugates in one liquid pocket with rainbow color scaled according to elapsed time. Trajectories of free and single Au nanoparticles are visually distinguishable from clusters of two roughly parallel trajectories.

A series of quantitative analysis of the clustered trajectories indicates that the dsDNA linkers remain holding adjacent nanocrystals over prolonged period of imaging time. First, the projected inter-particle distances, though fluctuating, are consistently measured to be smaller than the estimated length of bridging dsDNA linkers (12 nm for 42 bp DNA) over 100 sec. In comparison, in the same liquid pocket with the same liquid environment, free Au nanoparticles not connecting to adjacent particles are measured to have a diffusivity of 1.7 nm^2/s, and thus can diffuse 25 nm on average during 100 sec, much larger than the linker length. Second, the projected inter-particle distance between Au nanocrystals fluctuates in a dimension determined by the length of dsDNA bridges. Not only do the projected inter-particle distances from independent trajectories in each group exhibit the same maximum value, the maximum value of the 42 bp sample is also consistently half of that of the 84 bp one. The consistency between the linker length and observed inter-particle distance demonstrates the structural integrity of the dsDNA in the dimer throughout the observation period. Third, the Pearson's correlation coefficients (defined as $r_{a,b} = \Sigma_{i=1}^{n}(a_i - \bar{a})(b_i - \bar{b})/\sqrt{(\Sigma_{i=1}^{n}(a_i - \bar{a})^2\Sigma_{i=1}^{n}(b_i - \bar{b})^2)}$ for vectors a, b of the same dimension) for the x ($r_{x,x}$) and y ($r_{y,y}$) components of each clustered pair of trajectories all show a high positive correlation, but low or even negative correlation for that of two free particles. These three features were reproduced across many samples of nanoconjugates. Taken together, the observations described here indicate that bridging dsDNAs are able to hold the component nanocrystal of the nanoconjugates during the imaging process.

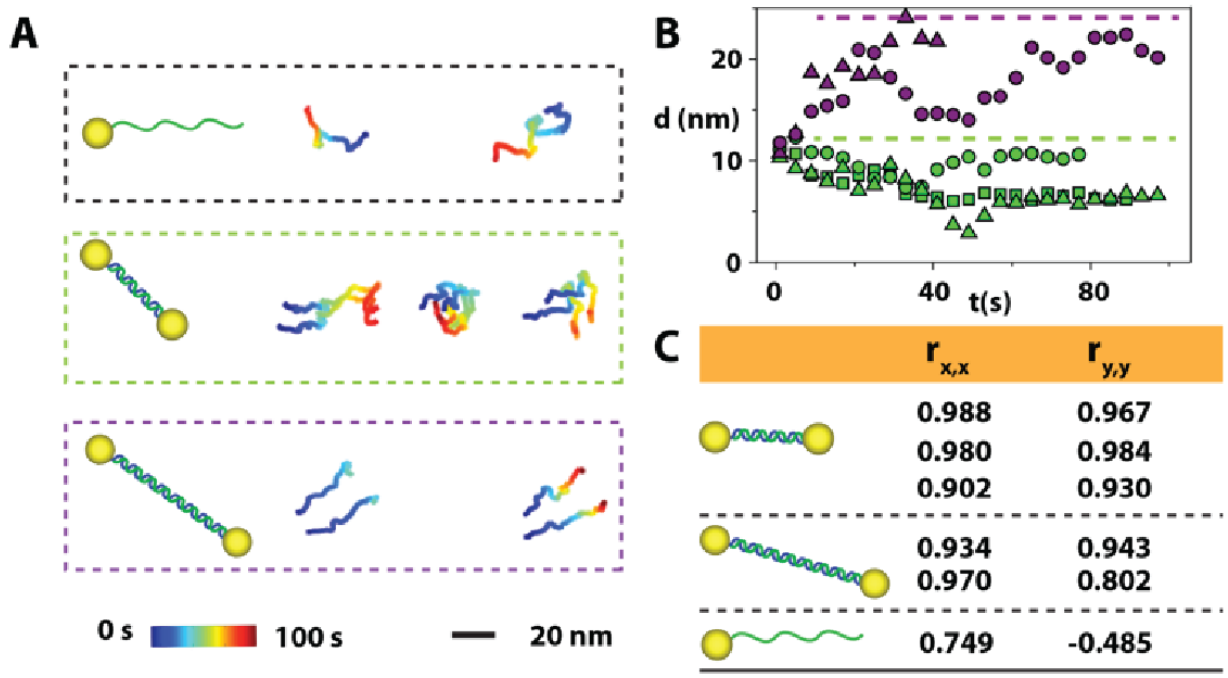

Figure 5.4: A collection of Au nanocrystal trajectories in the same liquid pocket. (A) An overview of the different trajectories color coded with time: individual particles, dimers linked by 42 base pair dsDNA (boxed in green), and dimers linked by 84 base pair dsDNA (boxed in purple). (B) The fluctuation of projected inter-particle distance d with time for three 42 bp dimers (green data points) and two 84 bp dimers (purple data points). The dotted lines highlight the maximuz of inter-particle distances (C) A table of the Pearson correlation of x and y components of two trajectories.

dsDNA bridge of a constant length

Earlier reports show that short dsDNA attached to gold nanoparticles can still fluctuate below its persistence length of around 50 nm due to the flexibility of the DNA (33). Here we look into the nature of diffusional statistics of the Au nanocrystal trajectories, since the projected inter-particle distance alone is complicated by nanoconjugate rotations. The bridge length between the dimers is shown to be regarded constant, or its fluctuation not differentiable within our resolved temporal window (1 frame per second).

The diffusional dynamics of both dimers and free nanocrystals are compared for trajectories observed in the same liquid pocket. The mean square displacement (MSD=$|r(t)-r(0)|^2$) and diffusion time t are calculated from ensemble average of all the trajectories. A linear relationship between MSD and diffusion time t, indicating Brownian diffusion (MSD= $4Dt$), is found for both single particle and dimer trajectories as shown in Figure 5.5B. Interestingly,

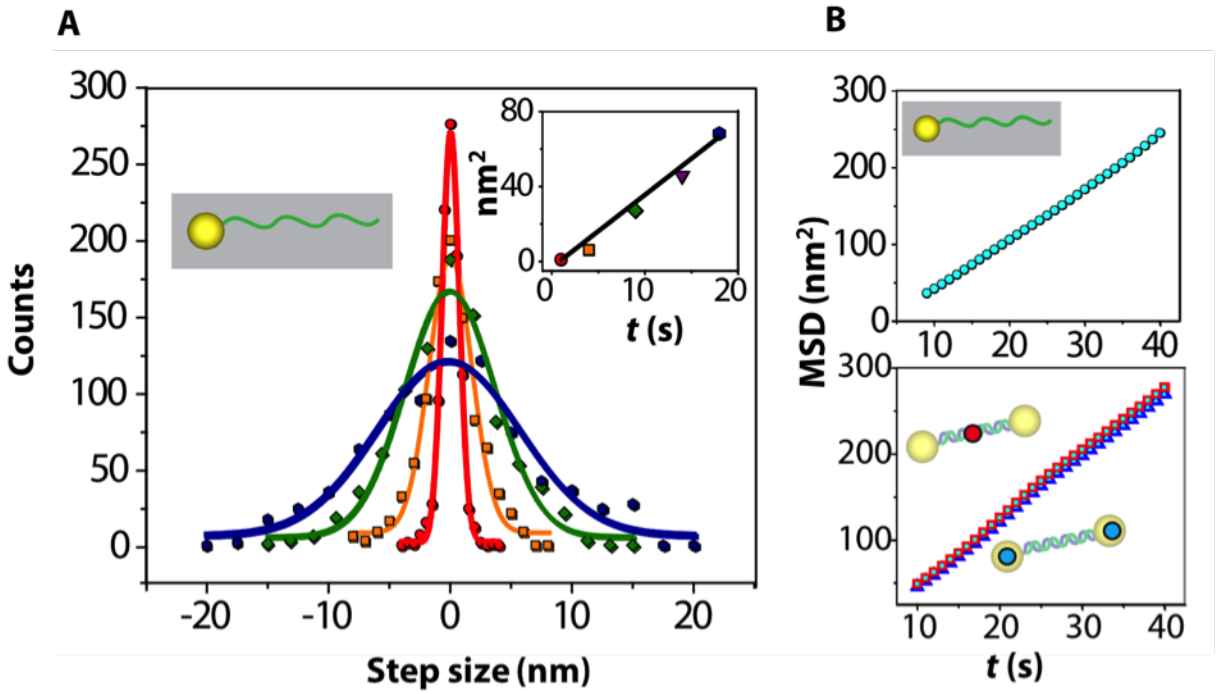

Figure 5.5: Diffusional statistics of Au-single strand DNA and Au-42 bp dsDNA trajectories. (A) Step size, i.e. diffusional displacement, distribution of ensemble averaged single particle trajectories for different time ?steps?: red circles for 1 s, orange squares for 4 s, green diamonds for 9 s, and blue hexagons for 18 s. The connecting lines, with the same coloring theme, are the Gaussian fittings. The inset shows the linear relationship between the fitted Gaussian widths for each curve with time. (B) The MSD-t plot for single particles (above), and dimers (below). In the plot for dimers, we show two ways of describing its motion, center-of-mass of the dimer (red squares), and ends of the dimer (blue triangles).

the diffusivity D, one fourth of the measured MSD-t curve slope, are the same for single particles and dimers tracked by either center-of-mass or end motions. This convergence in diffusivities can be explained by modeling a dimer as two single particles connected by an elastic spring, which relaxes at a time scale much faster than our observation time scale so as to smear out possible constraints in motion felt by the two component particles (see further discussion in Supplementary Information). Thus, we see a constant linker length from this averaging. The measured abnormally sluggish diffusivity D=1.7 nm^2/s agrees with values determined in previous reports on slowed nanocrystal diffusions (12, 16, 17) in various liquid cell configurations. More importantly, this slowed motion in a liquid cell configuration allows observation of nanoscale objects within the instrument capability; in contrast, these objects, if suspended in a bulk environment, exhibit ultrafast Brownian diffusion that overwhelms data collection capability.

It is also inferred from another statistical measure, the step-size distribution of ensemble free nanocrystal trajectories, that no localized attraction between the nanocrystal and the substrate is observed. The single Gaussian shape of the distribution contrasts with the multiple Gaussians in Si_3N_4 liquid cell studies (17), and echoes our observation of a rotating dimer. Evidently, the force of attraction between the nanocrystals and the graphene is much smaller than with the silicon nitride, so that the graphene does not perturb the trajectories, while the silicon nitride does. The width of the Gaussian is linearly related to step size, which in return demonstrates the Brownian nature of the particle motions in this liquid pocket, the basis for our comparative study above.

Three dimensional configuration and motions of trimers

Now that we have demonstrated that nanoconjugates rotate freely with structural rigidity in the liquid pocket, we extract the configuration and motion of dsDNA-Au nanoconjugates in three dimensions from time elapsed TEM images. Such information, though critical to their plasmonic coupled properties (30, 31), has been previously inaccessible from conventional TEM because drying samples on a grid flattens any 3D structure through evaporation. Our frame-based iterative optimization method does not require a priori knowledge of the linker lengths but uses reasonably arbitrary values as initial numbers. These initially assigned linker lengths are iterated until they converge towards one rigid structure in three dimensions for all the frames in the continuous trajectory.

Figure 5.6 demonstrates the validity of this iterative method: from the raw TEM images, both the rotational (color-coded arrows) and translational (color-coded dots) motions are as shown in Figure 5.6B, reestablished from one converged 3D trimer structure. We use a trimer to show how our iterative reconstruction works, but the principles we introduce here can be applied extensively to other types of 3D frameworks. The iteration starts from a set of linker lengths, l_1 and l_2 . The ratio between the linker length $l_{1,2}$ and projected length $d_{1,2}$ generates the z coordinates, while the projected positions read x and y coordinates directly.

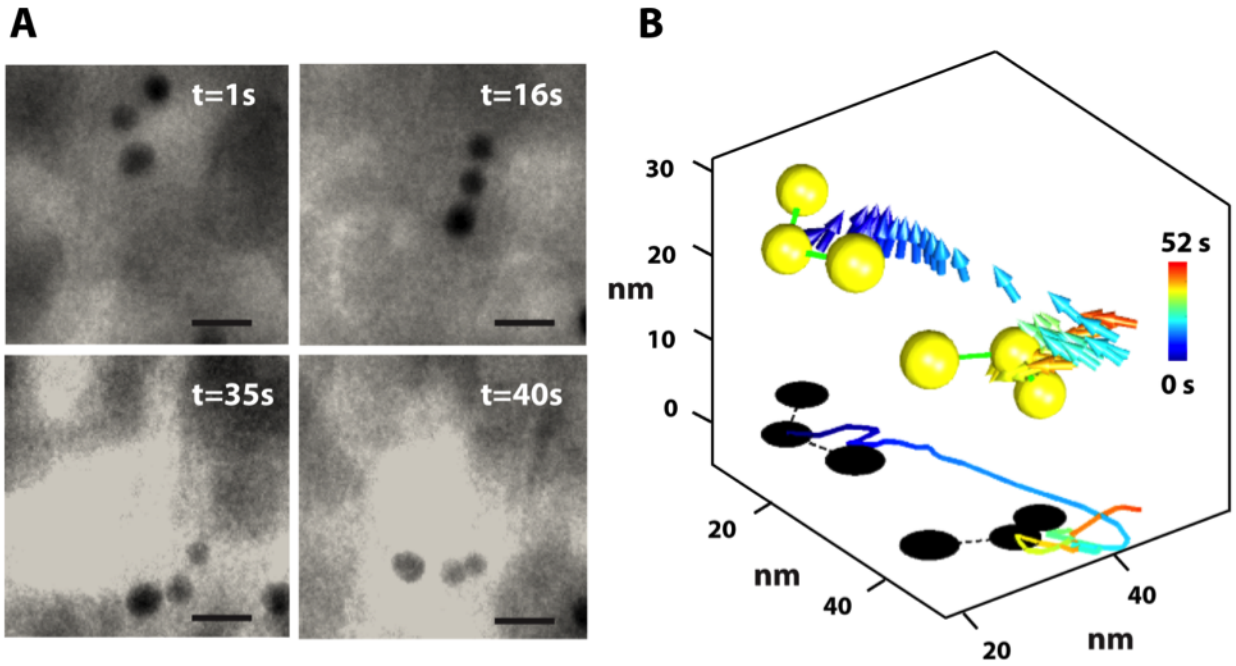

Figure 5.6: The 3D configuration and motion of a trimer. (A) Time elapsed TEM images of a trimer with viewing position fixed. The background fluctuation due to the liquid is in position with previous liquid cell TEM studies. (B) The reconstructed rotational (color coded arrows) and translational (color coded dots for the central nanocrystal) motion of the trimer in three dimensions. The two representative 3D trimer (yellow spheres linked by green lines) show their configuration as well as configuration at t = 1s, 40 s respectively. Their projections (black circular shapes) match with TEM images well. Scale bar is 10 nm.

Each frame thus generates one set of 3D positions for each particle, i.e. 3D configuration of the trimer. The iteration continues, with the inputs being adaptive, until the trimers constructed from all the frames, continuous yet independent from each other, converge into one structure. Mathematically, we use the standard deviation of the inter-particle distance l_3 calculated from the obtained 3D coordinates of the trimer in each frame as the handle to fine-tune the initial values. The final set of l_1 and l_2 values are obtained after the calculated standard deviation of the set of l_3 is minimized, i.e. after l_3 converges to a constant value for different image frames. The final converged structure is now endowed with all degrees of freedom, following a four-dimensional trajectory matching with the continuous 2D movie we captured. Here the principle of reconstructing 3D structure and motion from 2D projections is demonstrated, with details retrieved at high fidelity from a dynamic movie from liquid cell TEM. This principle and the technique can be easily extended to other structures in order

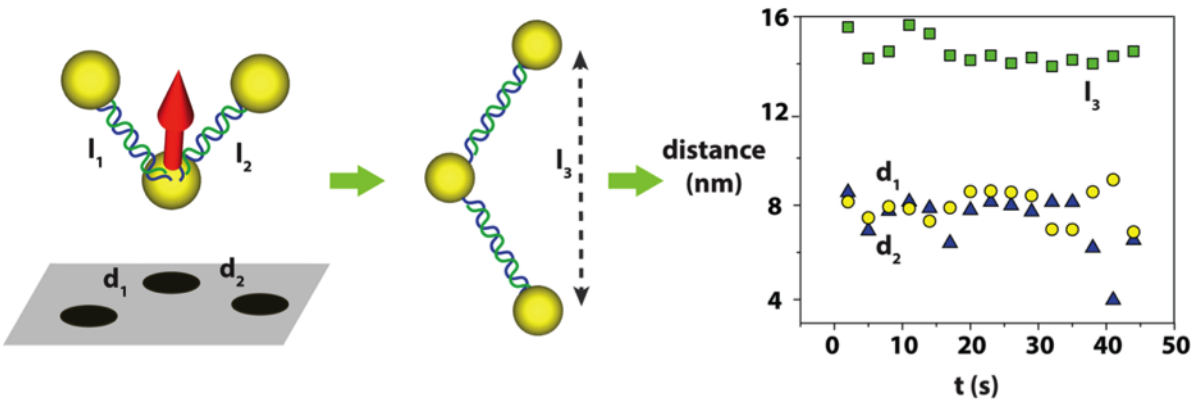

Figure 5.7: The iterative construction for the trimer shown in Figure 5.6. From left to right: a trimer in a 3d space, with inter particle linker lengths l_1 and l_2, and red arrow showing its orientation. For each frame one trimer is reconstructed with l_3. l_3 (green squares) remains constant throughout the 42 s of observation time, while the projected interparticle distances d_1 and d_2 fluctuate significantly more due to rotation.

to relate their 3D configuration and motions in solution to their function. One extension will be to image the 3D conformation dynamics of low contrast proteins using attached Au nanoparticles as high contrast agents (26, 28, 34).

Radiation damage and DNA viability

A surprising result here is the stability of dsDNA linkers throughout the obesrvation under the electron microscope. The Au nanocrystal components of the nanoconjugates are retained for a prolonged time under an estimated dosage rate onto the graphene liquid cell as a whole: 60-100 $e^-/(\mathring{A}^2 s)$, which is more than the critical dosage previously reported for biological molecules (4). Several observations from our experiment demonstrating the continued action of the linkers are discussed above: the retention of the expected projected inter-particle distance for a time far longer than that for which free particles would diffuse far apart, the correlated motions in paired trajectories, the rigid linker indicated from motion analysis, and the convergence of reconstructed structure into one single 3d configuration.

Since the conservation of dsDNA linkers is significant to biomolecule imaging, we performed more experiments to confirm it based upon intentional manipulation via the electron beam. We focus the electron beam to induce huge convection or likely drill a hole in the liquid pocket membrane. All the particles, no matter whether they are originally bridged by dsDNA or not, now move towards one direction, as the random Brownian motion is overwhelmed by solvent-driven convection. This directional, or superdiffusional, motion can

be seen clearly from the MSD-t curve with a slope of 1.9. Still dimers differentiate themselves from single particles by maintaining a small inter-particle distance during the violent convection process.

The DNA linkers are vulnerable to the electron beam when the radiation exceeds manageable dosages. In the experiments when we exposed sample to the electron beam continuously over a prolonged imaging time, particles originally clustered and moving together are sometimes swept apart at a later time, which in turn demonstrates that the linker has suddenly been broken.

We are aware that it is still an open question whether the existence of bridging linkers between Au nanocrystals corresponds to complete structural integrity of dsDNA in molecular level, and how the graphene wrap together with liquid environment strive to stabilize dsDNA. More quantitative and comparative evaluation of radiation damage for a graphene liquid cell EM and normal EM is required and currently in progress. But the experimental facts promise dynamic trajectories including both position and 3D configurations for biological molecules brought by graphene liquid cell.

Conclusions

We show the in situ observation of 3D dynamics of nanocrystal-DNA nanoconjugates, and we develop the 3D reconstruction of both the configuration and motions, which are inaccessible with a conventional TEM technique. Looking forward, this work opens many opportunities to study the dynamics of biological macro molecular assemblies and artificial nanostructures as they evolve and function in time.

5.3 Electron tomography of single 84bp DNA

The dynamic personalities and structural heterogeneity of biomolecules are essential for proper functioning. Structural determination of dynamic/heterogeneous proteins is limited by conventional approaches of X-ray and electron microscopy (EM) of single-particle reconstruction that require an average from thousands to millions different molecules. Cryo-electron microscopy has been used to determine the 3D structure of DNA objects with high symmetry by averaging together many images [137, 167]. Single molecules and complexes with high molecular weight can be reconstructed as well, including circular DNA [168] and transcription factors bound to promoter sequences [169].

Cryo-electron tomography (cryoET) is an approach to determine three-dimensional (3D) reconstruction of a single and unique biological object such as bacteria and cells, by imaging the object from a series of tilting angles. High resolution imaging (less than 2nm) of biological material by electron tomography has been limited by reconstruction resolution. Image distortion, tilt axis, and tilt angle errors all contribute to the low reconstruction reso-

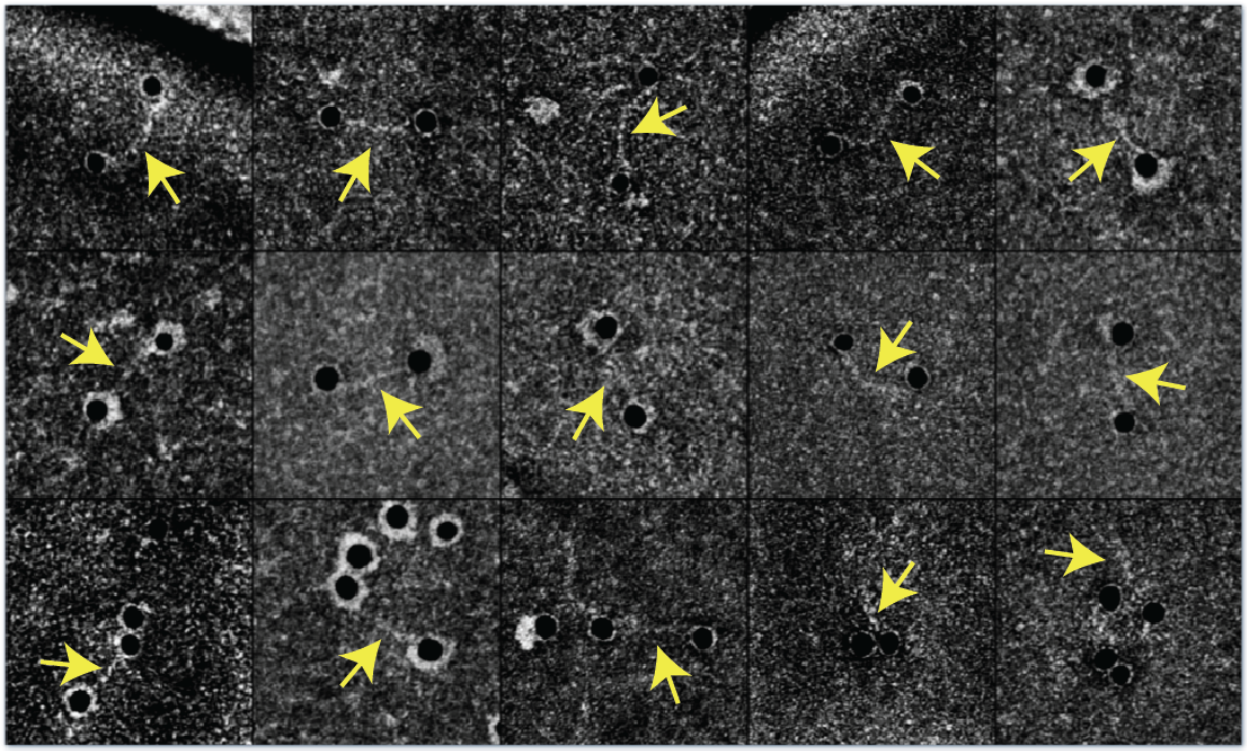

Figure 5.8: Electron micrographs of a number of DNA-nanoparticle conformations revealed by optimized negative stain.

lution. A focused electron tomography reconstruction (FETR) algorithm has recently been developed by Ren and coworkers [170] to decrease the size of the reconstructing image and therefore increase the resolution. The FETR algorithm can tolerate measuring tilt-errors, and determine the translational parameters via an iterative refinement process. To date, the method has been used to examine heterogeneity in populations of globular, high molecular weight proteins [145]. Toward the goal of visualizing a biological structure with a dimension smaller than 2nm, double stranded DNA labeled on either end with gold nanoparticles was characterized by IPET.

Nanoparticle dimers linked by a DNA double helix were synthesized. The nanoparticles were prepared with the appropriate surface chemistry to react with thiolated oligonucleotides. These DNA-nanoparticle conjugates were purified to isolate monoconjugated nanoparticles from bare nanoparticles and higher order conjugates using HPLC. These monoconjugates were reacted with the complement. Dimers were isolated by gel electrophoresis. In order to minimized background, dimer samples were transferred from tris-borate-EDTA to distilled water. DNA-nanoparticle samples were imaged within three hours of transfer into buffer to prevent DNA degradation. Samples were diluted to .1μM and deposited on plasma cleaned carbon-coated TEM grids. The grids were stained with uranyl formate and allowed to dry.

The dried grids were loaded into a TEM grid holder (tiltable Gatan holder) and imaged with electron tomography at high magnification (Zeiss Libra 120 TEM) under low electron flux to minimize degradation of the sample. The resulting data was analyzed using IPET, SPIDER, and EMAN software to recreate a 3D density map of the DNA double helix.

In order to study the conformations (from a 3D view instead of a 2D projection) of the DNA-nanoparticle dimer, it was imaged from a series of tilted-angles. By tracking a targeted individual complex, we reconstructed its 3D density map from tilted image views via IPET. Since the 3D density map is from a single flash-fixed particle kept in the same conformation during ET imaging, the 3D map shows the structure of this targeted particle which is dynamic-free, conformational-free, and heterogeneity-free. Electron micrographs of negative stained DNA-nanoparticle dimers show that the nanoparticle dimers exist in two conformations. Many particles are extended the maximum distance the DNA will allow, resulting in a fairly straight double helix. A sizable minority of assemblies show the gold particles immediately next to each other while the DNA appears to have supercoiled into a hairpin structure. Preliminary electron tomography data agrees with a molecular model of DNA, though without sufficiently high resolution to elucidate the major and minor groove of the double helix. These preliminary results indicate that gold nanoparticle labels can be used to probe the conformations of short DNA strands used in nanotechnology.

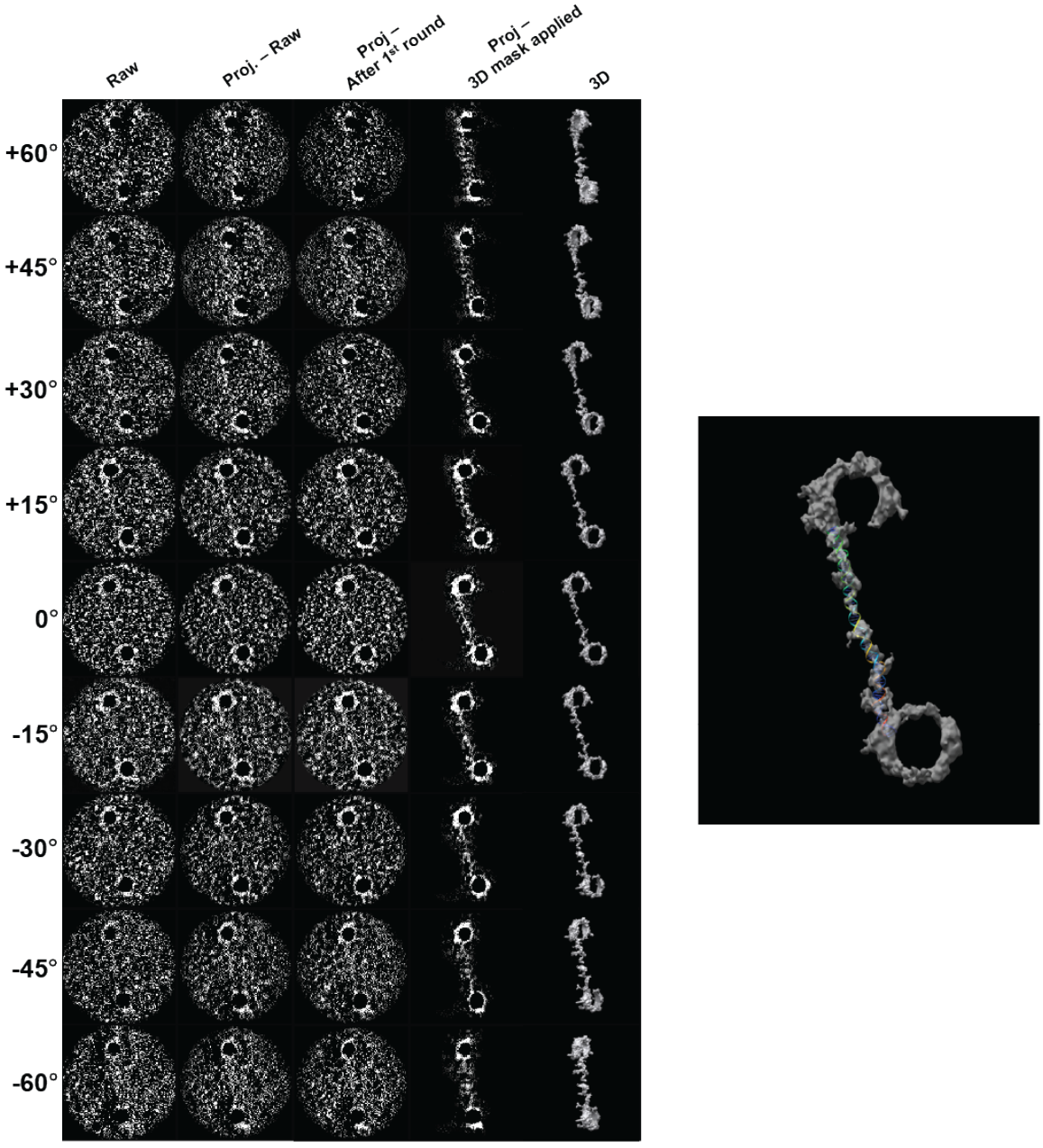

Figure 5.9: (Left) An individual DNA-NG complex was imaged by OpNS-ET. Nine tilted views of the same individual complex were selected from 81 tilt micrographs and displayed in the leftmost column. By means of the FETR algorithm, the 3D reconstruction was iterated and converged. The corresponding tilting projections of the 3D reconstruction from major iterations are displayed beside the raw images in next to four columns. (Right) The final 3D reconstruction of a targeted individual complex (resolution is 1.9nm). Fitting the 84-bp DNA model into this density map shows a good match. Scale bars: 5nm.

Chapter 6

Conclusions

In this dissertation, anisotropies have been introduced into DNA-assembled gold nanoparticle structures. To synthesize discrete structures with defined geometry, careful attention has been paid to the design of DNA sequences, nanoparticle surface chemistry, and nanoparticle conjugate separations. Gold nanorods have been incorporated into plasmon rulers with DNA containing a restriction enzyme recognition sequence. By tuning the conditions of separation, the relative orientation of nanorods can be controlled. DNA-assembled nanorod dimers were characterized by TEM image analysis and optical coupling was measured by ensemble visible spectroscopy. Chiral assemblies create a circular dichroism based plasmon ruler. This structure was designed with the aid of coupled dipole approximation calculations and the consideration of the tertiary structure of the DNA double helix. The optical coupling of gold nanoparticles in a chiral arrangement was observed via circular dichroism spectroscopy and represents a substrate for a solution phase switchable metamaterial. The structure of DNA-nanoparticle assemblies was elucidated in three dimensions using individual particle electron tomography and grapheme liquid cell transmission electron microscopy. The efforts described in this dissertation represent progress toward the synthesis and characterization of a three-dimensional plasmon ruler.

References

(1) Kelly, K. L.; Coronado, E.; Zhao, L. L.; Schatz, G. C. The Optical Properties of Metal Nanoparticles: The Influence of Size, Shape, and Dielectric Environment. *The Journal of Physical Chemistry B* **2003**, *107*, 668–677.

(2) Bohren, C. F.; Huffman, D. R., *Absorption and Scattering of Light by Small Particles*; John Wiley & Sons: 2008.

(3) Kunz, K. F.; J, L. R., *The Finite Difference Time Domain Method for Electromagnetics*; CRC Press: 1993.

(4) Yang, W.-H.; Schatz, G. C.; Van Duyne, R. P. Discrete dipole approximation for calculating extinction and Raman intensities for small particles with arbitrary shapes. *The Journal of Chemical Physics* **1995**, *103*, 869.

(5) Grabar, K. C.; Freeman, R. G.; Hommer, M. B.; Natan, M. J. Preparation and Characterization of Au Colloid Monolayers. *Analytical Chemistry* **2002**, *67*, 735–743.

(6) Pham, T.; Jackson, J. B.; Halas, N. J.; Lee, T. R. Preparation and characterization of gold nanoshells coated with self-assembled monolayers. *Langmuir* **2002**, *18*, 4915–4920.

(7) Millstone, J. E.; Park, S.; Shuford, K. L.; Qin, L.; Schatz, G. C.; Mirkin, C. A. Observation of a Quadrupole Plasmon Mode for a Colloidal Solution of Gold Nanoprisms. *Journal of the American Chemical Society* **2005**, *127*, 5312–5313.

(8) Gou, L.; Murphy, C. J. Fine-Tuning the Shape of Gold Nanorods. *Chemistry of Materials* **2005**, *17*, 3668–3672.

(9) Alivisatos, A. P.; Johnsson, K. P.; Peng, X.; Wilson, T. E.; Loweth, C. J.; Bruchez, M. P.; Schultz, P. G. Organization of 'nanocrystal molecules' using DNA. *Nature* **1996**, *382*, 609–611.

(10) Mirkin, C. A.; Letsinger, R. L.; Mucic, R. C.; Storhoff, J. J. A DNA-based method for rationally assembling nanoparticles into macroscopic materials. **1996**, *382*, 607–609.

(11) Tan, S. J.; Campolongo, M. J.; Luo, D.; Cheng, W. Building plasmonic nanostructures with DNA. *Nature Publishing Group* **2011**, *6*, 268–276.

(12) Smith, J. M. Controlling the orientation of DNA-assembled gold nanorod dimers. *in preparation.*

(13) Jones, M. R.; Macfarlane, R. J.; Lee, B.; Zhang, J.; Young, K. L.; Senesi, A. J.; Mirkin, C. A. DNA-nanoparticle superlattices formed from anisotropic building blocks. *Nature Materials* **2010**, *9*, 913–917.

(14) Sönnichsen, C.; Reinhard, B. M.; Liphardt, J.; Alivisatos, A. P. A molecular ruler based on plasmon coupling of single gold and silver nanoparticles. *Nature Biotechnology* **2005**, *23*, 741–745.

(15) Reinhard, B. M.; Sheikholeslami, S.; Mastroianni, A.; Alivisatos, A. P.; Liphardt, J. Use of plasmon coupling to reveal the dynamics of DNA bending and cleavage by single EcoRV restriction enzymes. *Proceedings of the National Academy of Sciences of the United States of America* **2007**, *104*, 2667–2672.

(16) Jun, Y.-w.; Sheikholeslami, S.; Hostetter, D. R.; Tajon, C.; Craik, C.; Alivisatos, A. P. Continuous imaging of plasmon rulers in live cells reveals early-stage caspase-3 activation at the single-molecule level. *Proceedings of the National Academy of Sciences* **2009**, *106*, 17735–17740.

(17) Liu, N.; Hentschel, M.; Weiss, T.; Alivisatos, A. P.; Giessen, H. Three-Dimensional Plasmon Rulers. *Science* **2011**, *332*, 1407–1410.

(18) Zhang, L.; Ren, G. IPET and FETR: Experimental Approach for Studying Molecular Structure Dynamics by Cryo-Electron Tomography of a Single-Molecule Structure. *PloS one* **2012**, *7*, e30249.

(19) Yuk, J. M.; Park, J.; Ercius, P.; Kim, K.; Hellebusch, D. J.; Crommie, M. F.; Lee, J. Y.; Zettl, A.; Alivisatos, A. P. High-Resolution EM of Colloidal Nanocrystal Growth Using Graphene Liquid Cells. *Science* **2012**, *336*, 61–64.

(20) Faraday, M. The Bakerian lecture: experimental relations of gold (and other metals) to light. *Philosophical Transactions of the Royal Society of ...* **1857**, *147*, 145–181.

(21) Frens, G. Controlled Nucleation for the Regulation of the Particle Size in Monodisperse Gold Suspensions. *Nature* **1973**, *241*, 20–22.

(22) WILCOXON, J. P.; WILLIAMSON, R. L.; BAUGHMAN, R. Optical-Properties of Gold Colloids Formed in Inverse Micelles. *Journal of Chemical Physics* **1993**, *98*, 9933–9950.

(23) Mozyrsky, D.; Privman, V. Diffusional growth of colloids. *Journal of Chemical Physics* **1999**, *110*, 9254–9258.

(24) Xia, Y.; Xiong, Y.; Lim, B.; Skrabalak, S. E. Shape-Controlled Synthesis of Metal Nanocrystals: Simple Chemistry Meets Complex Physics? *Angewandte Chemie International Edition* **2009**, *48*, 60–103.

(25) Gou, L.; Murphy, C. J. Fine-Tuning the Shape of Gold Nanorods. *Chemistry of Materials* **2005**, *17*, 3668–3672.

(26) Sau, T. K.; Murphy, C. J. Seeded High Yield Synthesis of Short Au Nanorods in Aqueous Solution. *Langmuir* **2004**, *20*, 6414–6420.

(27) Sau, T. K.; Murphy, C. J. Room Temperature, High-Yield Synthesis of Multiple Shapes of Gold Nanoparticles in Aqueous Solution. *Journal of the American Chemical Society* **2004**, *126*, 8648–8649.

(28) Wang, Z. L.; Gao, R. P.; Nikoobakht, B.; El-Sayed, M. A. Surface reconstruction of the unstable 110 surface in gold nanorods. *Journal of Physical Chemistry B* **2000**, *104*, 5417–5420.

(29) Smith, D. K.; Miller, N. R.; Korgel, B. A. Iodide in CTAB Prevents Gold Nanorod Formation. *Langmuir* **2009**, *25*, 9518–9524.

(30) Ha, T. H.; Koo, H.-J.; Chung, B. H. Shape-controlled syntheses of gold nanoprisms and nanorods influenced by specific adsorption of halide ions. *Journal of Physical Chemistry C* **2007**, *111*, 1123–1130.

(31) Millstone, J. E.; Wei, W.; Jones, M. R.; Yoo, H.; Mirkin, C. A. Iodide Ions Control Seed-Mediated Growth of Anisotropic Gold Nanoparticles. *Nano Letters* **2008**, *8*, 2526–2529.

(32) Zanchet, D.; Micheel, C. M.; Parak, W. J.; Gerion, D.; Alivisatos, A. P. Electrophoretic Isolation of Discrete Au Nanocrystal/DNA Conjugates. *Nano Letters* **2001**, *1*, 32–35.

(33) Claridge, S. A.; Goh, S. L.; Fréchet, J. M. J.; Williams, S. C.; Micheel, C. M.; Alivisatos, A. P. Directed Assembly of Discrete Gold Nanoparticle Groupings Using Branched DNA Scaffolds. *Chemistry of Materials* **2005**, *17*, 1628–1635.

(34) Claridge, S. A.; Liang, H. W.; Basu, S. R.; Fréchet, J. M. J.; Alivisatos, A. P. Isolation of Discrete Nanoparticle DNA Conjugates for Plasmonic Applications. *Nano Letters* **2008**, *8*, 1202–1206.

(35) Schroedter, A.; Weller, H. Ligand Design and Bioconjugation of Colloidal Gold Nanoparticles. *Angewandte Chemie International Edition* **2002**, *41*, 3218–3221.

(36) Jhaveri, S. D.; Foos, E. E.; Lowy, D. A.; Chang, E. L.; Snow, A. W.; Ancona, M. G. Isolation and characterization of trioxyethylene-encapsulated gold nanoclusters functionalized with a single DNA strand. *Nano Letters* **2004**, *4*, 737–740.

(37) Foos, E. E.; Snow, A. W.; Twigg, M. E.; Ancona, M. G. Thiol-terminated Di-, Tri-, and tetraethylene oxide functionalized gold nanoparticles: A water-soluble, charge-neutral cluster. *Chemistry of Materials* **2002**, *14*, 2401–2408.

(38) Kanaras, A. G.; Wang, Z.; Bates, A. D.; Cosstick, R.; Brust, M. Towards Multistep Nanostructure Synthesis: Programmed Enzymatic Self-Assembly of DNA/Gold Systems. *Angewandte Chemie* **2003**, *115*, 201–204.

(39) Ghosh, P.; Han, G.; De, M.; Kim, C. K.; Rotello, V. M. Gold nanoparticles in delivery applications. *Advanced Drug Delivery Reviews* **2008**, *60*, 1307–1315.

(40) Herne, T. M.; Tarlov, M. J. Characterization of DNA probes immobilized on gold surfaces. *Journal of the American Chemical Society* **1997**, *119*, 8916–8920.

(41) Li, H. X.; Rothberg, L. J. Label-free colorimetric detection of specific sequences in genomic DNA amplified by the polymerase chain reaction. *Journal of the American Chemical Society* **2004**, *126*, 10958–10961.

(42) Storhoff, J. J.; Elghanian, R.; Mirkin, C. A.; Letsinger, R. L. Sequence-Dependent Stability of DNA-Modified Gold Nanoparticles. *Langmuir* **2002**, *18*, 6666–6670.

(43) Sandstrom, P.; Boncheva, M.; Akerman, B. Nonspecific and thiol-specific binding of DNA to gold nanoparticles. *Langmuir* **2003**, *19*, 7537–7543.

(44) Micheel, C. M. Biomolecular Assembly of Gold Nanocrystals., Ph.D. Thesis, University of California - Berkeley, 2005.

(45) Warner, M. G.; Hutchison, J. E. Linear assemblies of nanoparticles electrostatically organized on DNA scaffolds. *Nature Materials* **2003**, *2*, 272–277.

(46) Rogers, Y. H.; Jiang-Baucom, P.; Huang, Z. J.; Bogdanov, V.; Anderson, S.; Boyce-Jacino, M. T. Immobilization of oligonucleotides onto a glass support via disulfide bonds: A method for preparation of DNA microarrays. *Analytical Biochemistry* **1999**, *266*, 23–30.

(47) Letsinger, R. L.; Elghanian, R.; Viswanadham, G.; Mirkin, C. A. Use of a Steroid Cyclic Disulfide Anchor in Constructing Gold Nanoparticle-Oligonucleotide Conjugates. *Bioconjugate Chemistry* **2000**, *11*, 289–291.

(48) Li, Z.; Jin, R.; Mirkin, C. A.; Letsinger, R. L. Multiple thiol-anchor capped DNA-gold nanoparticle conjugates. *Nucleic acids research* **2002**, *30*, 1558–1562.

(49) Hakkinen, H. The gold-sulfur interface at the nanoscale. *Nature Chemistry* **2012**, *4*, 443–455.

(50) Fu, A.; Micheel, C. M.; Cha, J.; Chang, H.; Yang, H.; Alivisatos, A. P. Discrete Nanostructures of Quantum Dots/Au with DNA. *Journal of the American Chemical Society* **2004**, *126*, 10832–10833.

(51) Sheikholeslami, S.; Jun, Y.-w.; Jain, P. K.; Alivisatos, A. P. Coupling of Optical Resonances in a Compositionally Asymmetric Plasmonic Nanoparticle Dimer. *Nano Letters* **2010**, *10*, 2655–2660.

(52) Zanchet, D.; Micheel, C. M.; Parak, W. J.; Gerion, D.; Williams, S. C.; Alivisatos, A. P. Electrophoretic and Structural Studies of DNA-Directed Au Nanoparticle Groupings. *The Journal of Physical Chemistry B* **2002**, *106*, 11758–11763.

(53) Rodbard, D.; Chrambach, A. Unified Theory for Gel Electrophoresis and Gel Filtration. *Proceedings of the National Academy of Sciences* **1970**, *65*, 970–977.

(54) Pernodet, N.; Maaloum, M.; Tinland, B. Pore size of agarose gels by atomic force microscopy. *ELECTROPHORESIS* **1997**, *18*, 55–58.

(55) Fritz, J. S. Early milestones in the development of ion-exchange chromatography: a personal account. *Journal of Chromatography A* **2004**, *1039*, 3–12.

(56) Wiesel, A.; Schmidt-Traub, H.; Lenz, J.; Strube, J. Modelling gradient elution of bioactive multicomponent systems in non-linear ion-exchange chromatography. *Journal of Chromatography A* **2003**, *1006*, 101–120.

(57) Zadeh, J. N.; Wolfe, B. R.; Pierce, N. A. Nucleic acid sequence design via efficient ensemble defect optimization. *Journal of computational ...* **2011**, *32*, 439–452.

(58) Min, Y.; Akbulut, M.; Kristiansen, K.; Golan, Y.; Israelachvili, J. The role of interparticle and external forces in nanoparticle assembly. *Nature Materials* **2008**, *7*, 527–538.

(59) Nikoobakht, B.; Wang, Z. L. Self-assembly of gold nanorods. *The Journal of Physical Chemistry B* **2000**, *104*, 8635–8640.

(60) Micheel, C. M.; Zanchet, D.; Alivisatos, A. P. Correlation Analysis of TEM Images of Nanocrystal Molecules. *Langmuir* **2008**, *24*, 10084–10088.

(61) Maxwell, J. C. XXV. On physical lines of force: Part I. - The Theory of Molecular Vortices applied to Magnetic Phenomena. *The London* **1861**, *25*, 161–175.

(62) Mie, G. Articles on the optical characteristics of turbid tubes, especially colloidal metal solutions. *Annalen Der Physik* **1908**, *25*, 377–445.

(63) Rayleigh, L. LVI. On the influence of obstacles arranged in rectangular order upon the properties of a medium. *Philosophical Magazine* **1892**, *34*, 481–502.

(64) Kreibig, U.; Fragstein, C. The limitation of electron mean free path in small silver particles. *Zeitschrift für Physik* **1969**, *224*, 307–323.

(65) Link, S.; El-Sayed, M. A. Spectral Properties and Relaxation Dynamics of Surface Plasmon Electronic Oscillations in Gold and Silver Nanodots and Nanorods. *The Journal of Physical Chemistry B* **1999**, *103*, 8410–8426.

(66) Jain, P. K.; Lee, K. S.; El-Sayed, I. H. Calculated absorption and scattering properties of gold nanoparticles of different size, shape, and composition: applications in biological imaging and biomedicine. *The Journal of Physical Chemistry B* **2006**, *110*, 7238–7248.

(67) Papavassiliou, G. C. Size effects on the raman excitation profiles of mixed valence compounds with metal-halide chain. *Progress in Solid State Chemistry* **1980**, *12*, 185.

(68) Sweatlock, L.; Maier, S.; Atwater, H.; Penninkhof, J.; Polman, A. Highly confined electromagnetic fields in arrays of strongly coupled Ag nanoparticles. *Physical Review B* **2005**, *71*, 235408.

(69) Xiao, J. J.; Huang, J. P.; Yu, K. W. Optical response of strongly coupled metal nanoparticles in dimer arrays. *Physical Review B* **2005**, *71*, 045404.

(70) Su, K. H.; Wei, Q. H.; Zhang, X.; Mock, J. J.; Smith, D. R.; Schultz, S. Interparticle Coupling Effects on Plasmon Resonances of Nanogold Particles. *Nano Letters* **2003**, *3*, 1087–1090.

(71) Gunnarsson, L.; Rindzevicius, T.; Prikulis, J. Confined plasmons in nanofabricated single silver particle pairs: experimental observations of strong interparticle interactions. *The Journal of Physical Chemistry B* **2005**, *109*, 1079–1087.

(72) Aizpurua, J.; Bryant, G. W.; Richter, L. J.; de Abajo, F.; Kelley, B. K.; Mallouk, T. Optical properties of coupled metallic nanorods for field-enhanced spectroscopy. *Physical Review B* **2005**, *71*, 235420.

(73) Mucic, R. C.; Storhoff, J. J.; Mirkin, C. A.; Letsinger, R. L. DNA-directed synthesis of binary nanoparticle network materials. *Journal of the American Chemical Society* **1998**, *120*, 12674–12675.

(74) Storhoff, J. J.; Lazarides, A. A.; Mucic, R. C.; Mirkin, C. A.; Letsinger, R. L.; Schatz, G. C. What controls the optical properties of DNA-linked gold nanoparticle assemblies? *Journal of the American Chemical Society* **2000**, *122*, 4640–4650.

(75) Jain, P. K.; Huang, W.; El-Sayed, M. A. On the Universal Scaling Behavior of the Distance Decay of Plasmon Coupling in Metal Nanoparticle Pairs: A Plasmon Ruler Equation. *Nano Letters* **2007**, *7*, 2080–2088.

(76) Nordlander, P.; Oubre, C.; Prodan, E.; Li, K.; Stockman, M. I. Plasmon Hybridization in Nanoparticle Dimers. *Nano Letters* **2004**, *4*, 899–903.

(77) Valev, V. K.; Baumberg, J. J.; Sibilia, C.; Verbiest, T. Chirality and Chiroptical Effects in Plasmonic Nanostructures: Fundamentals, Recent Progress, and Outlook. *Advanced Materials* **2013**, *25*, 2517–2534.

(78) Vignolini, S.; Yufa, N. A.; Cunha, P. S.; Guldin, S.; Rushkin, I.; Stefik, M.; Hur, K.; Wiesner, U.; Baumberg, J. J.; Steiner, U. A 3D Optical Metamaterial Made by Self-Assembly. *Advanced Materials* **2012**, *24*, OP23–OP27.

(79) Wang, J.; Feringa, B. L. Dynamic Control of Chiral Space in a Catalytic Asymmetric Reaction Using a Molecular Motor. *Science* **2011**, *331*, 1429–1432.

(80) Yan, W.; Xu, L.; Xu, C.; Ma, W.; Kuang, H.; Wang, L.; Kotov, N. A. Self-Assembly of Chiral Nanoparticle Pyramids with Strong R/S Optical Activity. *Journal of the American Chemical Society* **2012**, *134*, 15114–15121.

(81) Shen, X.; Asenjo-Garcia, A.; Liu, Q.; Jiang, Q. Three-dimensional plasmonic chiral tetramers assembled by DNA origami. *Nano ...* **2013**, *13*, 2128–2133.

(82) Fan, Z.; GOVOROV, A. O. Plasmonic Circular Dichroism of Chiral Metal Nanoparticle Assemblies. *Nano Letters* **2010**, *10*, 2580–2587.

(83) Hentschel, M.; Schaeferling, M.; Weiss, T.; Liu, N.; Giessen, H. Three-Dimensional Chiral Plasmonic Oligomers. *Nano Letters* **2012**, *12*, 2542–2547.

(84) Lowry, T. M. The Origin of Optical Rotatory Power. *Nature* **1935**, *136*, 191–192.

(85) Condon, E. U. Theories of Optical Rotatory Power. *Reviews of modern physics* **1937**, *9*, 432–457.

(86) Moffitt, W. Optical rotatory dispersion of helical polymers. *The Journal of Chemical Physics* **1956**, *25*, 467.

(87) El-Sayed, I. H.; Huang, X. H.; El-Sayed, M. A. Surface plasmon resonance scattering and absorption of anti-EGFR antibody conjugated gold nanoparticles in cancer diagnostics: Applications in oral cancer. *Nano Letters* **2005**, *5*, 829–834.

(88) Qiu, L.; Larson, T. A.; Vitkin, E.; Guo, L.; Hanlon, E. B.; Itzkan, I.; Sokolov, K. V.; Perelman, L. T. Gold nanorod light scattering labels for biomedical imaging. *Biomedical Optics Express* **2010**, *1*, 135–142.

(89) Huang, X.; El-Sayed, I. H.; Qian, W.; El-Sayed, M. A. Cancer Cell Imaging and Photothermal Therapy in the Near-Infrared Region by Using Gold Nanorods. *Journal of the American Chemical Society* **2006**, *128*, 2115.

(90) Zharov, V. P.; Mercer, K. E.; Galitovskaya, E. N.; Smeltzer, M. S. Photothermal nanotherapeutics and nanodiagnostics for selective killing of bacteria targeted with gold nanoparticles. *Biophysical Journal* **2006**, *90*, 619–627.

(91) Lee, S. E.; Sasaki, D. Y.; Park, Y.; Xu, R.; Brennan, J. S.; Bissell, M. J.; Lee, L. P. Photonic Gene Circuits by Optically Addressable siRNA-Au Nanoantennas. *ACS Nano* **2012**, *6*, 7770–7780.

(92) Lee, S. E.; Liu, G. L.; Kim, F.; Lee, L. P. Remote Optical Switch for Localized and Selective Control of Gene Interference. *Nano Letters* **2009**, *9*, 562–570.

(93) Yu, C.; Irudayaraj, J. Multiplex biosensor using gold nanorods. *Analytical Chemistry* **2007**, *79*, 572–579.

(94) Sudeep, P. K.; Joseph, S.; Thomas, K. G. Selective detection of cysteine and glutathione using gold nanorods. *Journal of the American Chemical Society* **2005**, *127*, 6516–6517.

(95) Wang, X.; Li, Y.; Wang, H.; Fu, Q.; Peng, J.; Wang, Y.; Du, J.; Zhou, Y.; Zhan, L. Gold nanorod-based localized surface plasmon resonance biosensor for sensitive detection of hepatitis B virus in buffer, blood serum and plasma. *Biosensors & Bioelectronics* **2010**, *26*, 404–410.

(96) Oyelere, A. K.; Chen, P. C.; Huang, X.; El-Sayed, I. H.; El-Sayed, M. A. Peptide-conjugated gold nanorods for nuclear targeting. *Bioconjugate Chemistry* **2007**, *18*, 1490–1497.

(97) Liao, H. W.; Hafner, J. H. Gold nanorod bioconjugates. *Chemistry of Materials* **2005**, *17*, 4636–4641.

(98) Rayavarapu, R. G.; Petersen, W.; Ungureanu, C.; Post, J. N.; van Leeuwen, T. G.; Manohar, S. Synthesis and bioconjugation of gold nanoparticles as potential molecular probes for light-based imaging techniques. *Journal of Biomedical Imaging* **2007**, *2007*, 5–5.

(99) Li, J. L.; Day, D.; Gu, M. Ultra-Low Energy Threshold for Cancer Photothermal Therapy Using Transferrin-Conjugated Gold Nanorods. *Advanced Materials* **2008**, *20*, 3866–3871.

(100) Millstone, J. E.; Georganopoulou, D. G.; Xu, X.; Wei, W.; Li, S.; Mirkin, C. A. DNA-Gold Triangular Nanoprism Conjugates. *Small* **2008**, *4*, 2176–2180.

(101) Yasun, E.; Gulbakan, B.; Ocsoy, I.; Yuan, Q.; Shukoor, M. I.; Li, C.; Tan, W. Enrichment and Detection of Rare Proteins with Aptamer-Conjugated Gold Nanorods. *Analytical Chemistry* **2012**, *84*, 6008–6015.

(102) Shi, D.; Song, C.; Jiang, Q.; Wang, Z.-G.; Ding, B. A facile and efficient method to modify gold nanorods with thiolated DNA at a low pH value. *Chemical Communications* **2013**, *49*, 2533–2535.

(103) Wijaya, A.; Schaffer, S. B.; Pallares, I. G.; Hamad-Schifferli, K. Selective release of multiple DNA oligonucleotides from gold nanorods. *ACS Nano* **2008**, *3*.

(104) Joo, J. H.; Lee, J.-S. Library Approach for Reliable Synthesis and Properties of DNA-Gold Nanorod Conjugates. *Analytical Chemistry* **2013**, *85*, 6580–6586.

(105) Pal, S.; Deng, Z.; Wang, H.; Zou, S.; Liu, Y.; Yan, H. DNA Directed Self-Assembly of Anisotropic Plasmonic Nanostructures. *Journal of the American Chemical Society* **2011**, *133*, 17606–17609.

(106) Dujardin, E.; Hsin, L. B.; Wang, C.; Mann, S. DNA-driven self-assembly of gold nanorods. *Chemical Communications* **2001**, *14*, 1264–1265.

(107) Chen, C. C.; Lin, Y. P.; Wang, C. W.; Tzeng, H. C.; Wu, C. H.; Chen, Y. C.; Chen, C. P.; Chen, L. C.; Wu, Y. C. DNA-gold nanorod conjugates for remote control of localized gene expression by near infrared irradiation. *Journal of the American Chemical Society* **2006**, *128*, 3709–3715.

(108) Li, Z.; Zhu, Z.; Liu, W.; Zhou, Y.; Han, B.; Gao, Y.; Tang, Z. Reversible Plasmonic Circular Dichroism of Au Nanorod and DNA Assemblies. *Journal of the American Chemical Society* **2012**, *134*, 3322–3325.

(109) Xiao, Z.; Ji, C.; Shi, J.; Pridgen, E. M.; Frieder, J.; Wu, J.; Farokhzad, O. C. DNA Self-Assembly of Targeted Near-Infrared-Responsive Gold Nanoparticles for Cancer Thermo-Chemotherapy. *Angewandte Chemie* **2012**, *124*, 12023–12027.

(110) Ma, W.; Kuang, H.; Xu, L.; Ding, L.; Xu, C.; Wang, L.; Kotov, N. A. Attomolar DNA detection with chiral nanorod assemblies. *Nature Communications* **2013**, *4*.

(111) Xu, L.; Kuang, H.; Xu, C.; Ma, W.; Wang, L.; Kotov, N. A. Regiospecific Plasmonic Assemblies for in Situ Raman Spectroscopy in Live Cells. *Journal of the American Chemical Society* **2012**, *134*, 1699–1709.

(112) Mastroianni, A. J.; Claridge, S. A.; Alivisatos, A. P. Pyramidal and Chiral Groupings of Gold Nanocrystals Assembled Using DNA Scaffolds. *Journal of the American Chemical Society* **2009**, *131*, 8455–8459.

(113) Cheng, W.; Hartman, M. R.; Smilgies, D. M. Probing in Real Time the Soft Crystallization of DNA-Capped Nanoparticles. *Angewandte Chemie International Edition* **2010**, *49*, 380–384.

(114) Jain, P. K.; Eustis, S.; El-Sayed, M. A. Plasmon coupling in nanorod assemblies: Optical absorption, discrete dipole approximation simulation, and exciton-coupling model. *Journal of Physical Chemistry B* **2006**, *110*, 18243–18253.

(115) Mastroianni, A. J.; Sivak, D. A.; Geissler, P. L.; Alivisatos, A. P. Probing the Conformational Distributions of Subpersistence Length DNA. *Biophysical Journal* **2009**, *97*, 1408–1417.

(116) Willingham, B.; Brandl, D. W.; Nordlander, P. Plasmon hybridization in nanorod dimers. *Applied Physics B-Lasers and Optics* **2008**, *93*, 209–216.

(117) Funston, A. M.; Novo, C.; Davis, T. J.; Mulvaney, P. Plasmon Coupling of Gold Nanorods at Short Distances and in Different Geometries. *Nano Letters* **2009**, *9*, 1651–1658.

(118) Pramod, P.; Thomas, K. G. Plasmon Coupling in Dimers of Au Nanorods. *Advanced Materials* **2008**, *20*, 4300–4305.

(119) Nepal, D.; Park, K.; Vaia, R. A. High-Yield Assembly of Soluble and Stable Gold Nanorod Pairs for High-Temperature Plasmonics. *Small* **2012**, *8*, 1013–1020.

(120) Grzelczak, M.; Vermant, J.; Furst, E. M.; Liz-Marzán, L. M. Directed Self-Assembly of Nanoparticles. *ACS Nano* **2010**, *4*, 3591–3605.

(121) Mühlig, S.; Farhat, M.; Rockstuhl, C.; Lederer, F. Cloaking dielectric spherical objects by a shell of metallic nanoparticles. *Physical Review B* **2011**, *83*, 195116.

(122) Fan, J. A.; Wu, C.; Bao, K.; Bao, J.; Bardhan, R.; Halas, N. J.; Manoharan, V. N.; Nordlander, P.; Shvets, G.; Capasso, F. Self-Assembled Plasmonic Nanoparticle Clusters. *Science* **2010**, *328*, 1135–1138.

(123) De La Rica, R.; Stevens, M. M. Plasmonic ELISA for the ultrasensitive detection of disease biomarkers with the naked eye. *Nature Nanotechnology* **2012**, *7*, 821–824.

(124) Maye, M. M.; Kumara, M. T.; Nykypanchuk, D. Switching binary states of nanoparticle superlattices and dimer clusters by DNA strands. *Nature* **2010**, *5*, 116–120.

(125) Pendry, J. B. A Chiral Route to Negative Refraction. *Science* **2004**, *306*, 1353–1355.

(126) Gansel, J. K.; Thiel, M.; Rill, M. S.; Decker, M.; Bade, K.; Saile, V.; von Freymann, G.; Linden, S.; Wegener, M. Gold Helix Photonic Metamaterial as Broadband Circular Polarizer. *Science* **2009**, *325*, 1513–1515.

(127) Tang, Y.; Cohen, A. E. Enhanced Enantioselectivity in Excitation of Chiral Molecules by Superchiral Light. *Science* **2011**, *332*, 333–336.

(128) Kuzyk, A.; Schreiber, R.; Fan, Z.; Pardatscher, G.; Roller, E. M. DNA-based self-assembly of chiral plasmonic nanostructures with tailored optical response. *Nature* **2012**, *483*, 311.

(129) Murata, K.; Aoki, M.; Suzuki, T.; Harada, T. Thermal and light control of the sol-gel phase transition in cholesterol-based organic gels. Novel helical aggregation modes as detected by circular dichroism and ... *Journal of the ...* **1994**, *116*, 6664–6676.

(130) Ikeda, K.; Liu, W. T.; Shen, Y. R.; Uekusa, H.; Ohashi, Y.; Koshihara, S. Photoinduced chirality switching in a cobaloxime complex crystal. *Journal of Chemical Physics* **2005**, *122*, 141103.

(131) Zhang, S.; Zhou, J.; Park, Y. S.; Rho, J.; Singh, R. Photoinduced handedness switching in terahertz chiral metamolecules. *Nature* **2012**, *3*.

(132) Auguié, B.; Alonso-Gómez, J. L.; Guerrero-Martínez, A.; Liz-Marzán, L. M. Fingers Crossed: Optical Activity of a Chiral Dimer of Plasmonic Nanorods. *The Journal of Physical Chemistry Letters* **2011**, *2*, 846–851.

(133) Fan, Z.; GOVOROV, A. O. Helical Metal Nanoparticle Assemblies with Defects: Plasmonic Chirality and Circular Dichroism. *Journal of Physical Chemistry C* **2011**, *115*, 13254–13261.

(134) Johnson, P. B.; Christy, R. W. Optical Constants of the Noble Metals. *Physical Review B* **1972**, *6*, 4370–4379.

(135) Goodman, R. P.; Heilemann, M.; Doose, S.; Erben, C. M.; Kapanidis, A. N.; Turberfield, A. J. Reconfigurable, braced, three-dimensional DNA nanostructures. *Nature Nanotechnology* **2008**, *3*, 93–96.

(136) Goodman, R. P. Rapid Chiral Assembly of Rigid DNA Building Blocks for Molecular Nanofabrication. *Science* **2005**, *310*, 1661–1665.

(137) Kato, T.; Goodman, R. P.; Erben, C. M.; Turberfield, A. J.; Namba, K. High-Resolution Structural Analysis of a DNA Nanostructure by cryoEM. *Nano Letters* **2009**, *9*, 2747–2750.

(138) Zheng, J.; Constantinou, P. E.; Micheel, C.; Alivisatos, A. P.; Kiehl, R. A.; Seeman, N. C. Two-Dimensional Nanoparticle Arrays Show the Organizational Power of Robust DNA Motifs. *Nano Letters* **2006**, *6*, 1502–1504.

(139) Evans, J. E.; Browning, N. D. Enabling direct nanoscale observations of biological reactions with dynamic TEM. *Microscopy* **2013**, *62*, 147–156.

(140) Kourkoutis, L. F.; Plitzko, J. M.; Baumeister, W. Electron Microscopy of Biological Materials at the Nanometer Scale. *Annual Review of Materials Research, Vol 42* **2012**, *42*, 33–58.

(141) Hui, S. W.; Parsons, D. F. Electron Diffraction of Wet Biological Membranes. *Science* **1974**, *184*, 77–78.

(142) Isaacson, M.; Johnson, D.; Crewe, A. V. Electron Beam Excitation and Damage of Biological Molecules; Its Implications for Specimen Damage in Electron Microscopy. *Radiation research* **1973**, *55*, 205.

(143) Lorenz, U. J.; Zewail, A. H. Biomechanics of DNA structures visualized by 4D electron microscopy. *Proceedings of the National Academy of Sciences* **2013**, *110*, 2822–2827.

(144) Xu, K.; Zhong, G.; Zhuang, X. Actin, Spectrin, and Associated Proteins Form a Periodic Cytoskeletal Structure in Axons. *Science* **2013**, *339*, 452–456.

(145) Jones, S. A.; Shim, S.-H.; He, J.; Zhuang, X. Fast, three-dimensional super-resolution imaging of live cells. *Nature Publishing Group* **2011**, *8*, 499–505.

(146) Warshel, A.; W Parson, W. Dynamics of biochemical and biophysical reactions: insight from computer simulations. *Quarterly reviews of biophysics* **2001**, *34*, 563–679.

(147) Berendsen, H. Collective protein dynamics in relation to function. *Current opinion in structural biology* **2000**, *10*, 165–169.

(148) Onuchic, J. N.; Wolynes, P. G. Theory of protein folding. *Current opinion in structural biology* **2004**, *14*, 70–75.

(149) De Jonge, N.; Ross, F. M. Electron microscopy of specimens in liquid. *Nature Nanotechnology* **2011**, *6*, 695–704.

(150) Li, D.; Nielsen, M. H.; Lee, J. R. I.; Frandsen, C.; Banfield, J. F.; De Yoreo, J. J. Direction-Specific Interactions Control Crystal Growth by Oriented Attachment. *Science* **2012**, *336*, 1014–1018.

(151) Liao, H.-G.; Cui, L.; Whitelam, S.; Zheng, H. Real-Time Imaging of Pt3Fe Nanorod Growth in Solution. *Science* **2012**, *336*, 1011–1014.

(152) Radisic, A.; Ross, F. M.; Searson, P. C. In situ study of the growth kinetics of individual island electrodeposition of copper. *The Journal of Physical ...* **2006**, *110*, 7862–7868.

(153) White, E. R.; Mecklenburg, M.; Shevitski, B.; Singer, S. B. Charged nanoparticle dynamics in water induced by scanning transmission electron microscopy. *Langmuir* **2012**, *28*, 3695–3698.

(154) Zheng, H.; Claridge, S. A.; Minor, A. M.; Alivisatos, A. P. Nanocrystal diffusion in a liquid thin film observed by in situ transmission electron microscopy. *Nano ...* **2009**, *9*, 2460–2465.

(155) Woehl, T. J.; Evans, J. E.; Arslan, I.; Ristenpart, W. D. Direct in situ determination of the mechanisms controlling nanoparticle nucleation and growth. *ACS Nano* **2012**, *6*, 8599–8610.

(156) White, E. R.; Singer, S. B.; Augustyn, V.; Hubbard, W. A.; Mecklenburg, M.; Dunn, B.; Regan, B. C. In Situ Transmission Electron Microscopy of Lead Dendrites and Lead Ions in Aqueous Solution. *ACS Nano* **2012**, *6*, 6308–6317.

(157) Evans, J. E.; Jungjohann, K. L.; Browning, N. D.; Arslan, I. Controlled growth of nanoparticles from solution with in situ liquid transmission electron microscopy. *Nano Letters* **2011**, *11*, 2809–2813.

(158) Mirsaidov, U. M.; Zheng, H.; Casana, Y.; Matsudaira, P. Imaging protein structure in water at 2.7 nm resolution by transmission electron microscopy. *Biophysical Journal* **2012**, *102*, 15–17.

(159) Peckys, D. B.; Mazur, P.; Gould, K. L.; de Jonge, N. Fully hydrated yeast cells imaged with electron microscopy. *Biophysical Journal* **2011**, *100*, 2522–2529.

(160) Sugi, H.; Minoda, H.; Inayoshi, Y.; Yumoto, F.; Miyakawa, T.; Miyauchi, Y.; Tanokura, M.; Akimoto, T.; Kobayashi, T.; Chaen, S.; Sugiura, S. Direct demonstration of the cross-bridge recovery stroke in muscle thick filaments in aqueous solution by using the hydration chamber. *Proceedings of the National Academy of Sciences* **2008**, *105*, 17396–17401.

(161) Liu, K.-L.; Wu, C.-C.; Huang, Y.-J.; Peng, H.-L.; Chang, H.-Y.; Chang, P.; Hsu, L.; Yew, T.-R. Novel microchip for in situ TEM imaging of living organisms and bio-reactions in aqueous conditions. *Lab on a Chip* **2008**, *8*, 1915–1921.

(162) Dukes, M. J.; Peckys, D. B.; de Jonge, N. Correlative Fluorescence Microscopy and Scanning Transmission Electron Microscopy of Quantum-Dot-Labeled Proteins in Whole Cells in Liquid. *ACS Nano* **2010**, *4*, 4110–4116.

(163) Peckys, D. B.; de Jonge, N. Visualizing Gold Nanoparticle Uptake in Live Cells with Liquid Scanning Transmission Electron Microscopy. *Nano Letters* **2011**, *11*, 1733–1738.

(164) Mohanty, N.; Fahrenholtz, M.; Nagaraja, A.; Boyle, D.; Berry, V. Impermeable Graphenic Encasement of Bacteria. *Nano Letters* **2011**, *11*, 1270–1275.

(165) Krueger, M.; Berg, S.; Stone, D. A.; Strelcov, E.; Dikin, D. A. Drop-casted self-assembling graphene oxide membranes for scanning electron microscopy on wet and dense gaseous samples. *ACS Nano* **2011**, *5*, 10047–10054.

(166) Hu, M.; Qian, L.; Briñas, R. P.; Lymar, E. S. Gold nanoparticle-protein arrays improve resolution for cryo-electron microscopy. *Journal of Structural Biology* **2008**, *161*, 83–91.

(167) Ko, S. H.; Su, M.; Zhang, C.; Ribbe, A. E.; Jiang, W.; Mao, C. Synergistic self-assembly of RNA and DNA molecules. *Nature Chemistry* **2010**, *2*, 1050–1055.

(168) Demurtas, D.; Amzallag, A.; Rawdon, E. J.; Maddocks, J. H.; Dubochet, J.; Stasiak, A. Bending modes of DNA directly addressed by cryo-electron microscopy of DNA minicircles. *Nucleic acids research* **2009**, *37*, 2882–2893.

(169) Cianfrocco, M. A.; Kassavetis, G. A.; Grob, P.; Fang, J.; Juven-Gershon, T.; Kadonaga, J. T.; Nogales, E. Human TFIID Binds to Core Promoter DNA in a Reorganized Structural State. *Cell* **2013**, *152*, 120–131.

(170) Zhang, L.; Ren, G. IPET and FETR: Experimental Approach for Studying Molecular Structure Dynamics by Cryo-Electron Tomography of a Single-Molecule Structure. *PloS one* **2012**, *7*, e30249.

Appendix A

Gold nanoparticle synthesis

Two syntheses are described. The first reliably produces 5nm particles while the second produces 13nm particles.

Citrate reduction for 13nm particles

Equipment

- 500mL one-neck round bottom flask
- Condenser with water jacket
- Stir bar (football)
- 250mL volumetric flask
- 25mL volumetric flask
- Heating mantle
- 25mL syringe

Chemicals

- $HAuCl_4$
- Sodium citrate
- MilliQ water

Notes

Glassware was cleaned by aqua regia or base bath. Best results were achieved with aqua regia-cleaned glassware.

Reagents were used as received without further purification. Best results were achieved with sodium citrate purchased from Alfa Aesar.

Solutions were prepared by weighing chemicals directly onto weigh paper and adding

MilliQ water to volumetric flasks which were filled with water and allowed to equilibrate for 10-60 minutes.

Preparation

In a 500mL round-bottom flask equipped with a condenser, 250 mL of 1mM $HAuC_4$ was brought to a rolling boil with vigorous stirring. The solution will come to a boil after about 15 minutes with the heating mantle on high. The citrate solution was injected to the vortex of the solution. The solution immediately changed from pale yellow to deep burgundy. Heat was applied for an additional 10 minutes with vigorous stirring. The heating mantle was removed and the solution was stirred for another 10 minutes.

Citrate reduction for 5nm particles

Equipment

250mL round bottom flask
Stir bar (football)
100mL volumetric flask
1 mL pipettor
pipet tips
ice bucket

Chemicals

$HAuCl_4$
K_2CO_3
$NaBH_4$
MilliQ water
ice

Notes

Glassware was cleaned by aqua regia or base bath. Best results were achieved with aqua regia-cleaned glassware.

Reagents were used as received without further purification. Best results were achieved with sodium borohydride purchased from Alfa Aesar and used immediately after purchase.

Solutions were prepared by weighing chemicals directly into glass vials and adding ice-cold water to the vials using a digital pipettor. Solutions were kept on ice for the duration of the reaction.

Preparation

Cool 500mL MilliQ water in refrigerator or on ice for 30 minutes. To 100mL water,

add 375μL %4 $HAuCl_4$ and 500μL .2M K_2CO_3. Allow solution to cool on ice while 10mL of .5mg/mL $NaBH_4$ is prepared. While gold solution stirs on ice, add five 1 mL aliquots of $NaBH_4$. Continue to stir on ice for 5 minutes. To remove impurities, centrifuge at 1200 rpm for 10 minutes and discard pellet.

Appendix B

Gold nanorod synthesis

The success of a gold nanorod synthesis depends dramatically on the quality of the CTAB used. Encountering a good batch of CTAB should be treated with appropriate seriousness.

Equipment

- Volumetric flasks
- Small magnetic stirbar
- Stirplate
- Ice bucket
- Foil
- Parafilm
- 50 mL Falcon tubes

Chemicals

- $HAuCl_4$
- CTAB
- MilliQ water
- Ascorbic acid
- $NaBH_4$
- Silver nitrate

Notes

Glassware was cleaned by aqua regia or base bath. Best results were achieved with aqua regia-cleaned glassware.

Reagents were used as received without further purification. Best results were achieved with all reagents purchased from Alfa Aesar and stored in a vacuum-sealed desiccator hidden from the view of coworkers.

Stock solutions

Solution 2

In a volumetric flask, prepare 0.2 M CTAB in water
(final volume: 100 mL, MW: 364.46 g)
Using weighing paper, each person will weigh between 0.8 g-1.5 g and add to volumetric flask.
When completed, place lid on flask. Parafilm lid.
In secondary containment, sonicate until dissolved.

Solution 3

In a 50 mL centrifuge tube, prepare 0.01M HAuCl4 in water
(final volume: 20 mL, MW: 393.83 g)
Vortex.
Cover tube with foil.
In a 50 mL centrifuge tube, prepare 0.00050 M HAuCl4 in water from 0.01M HAuCl4 stock solution.
Vortex.
Cover with foil.

Solution 4

In a 50 mL centrifuge tube, prepare 0.10 M ascorbic acid in water (final volume: 20 mL, MW: 176.12 g)
In secondary containment, sonicate until dissolved.
Cover tube with foil.

Solution 1

In a 50 mL centrifuge tube, prepare 0.01 M AgNO3 in water (final volume: 40 mL, MW: 169.87 g)
Vortex.

Solution 5

In a 50 mL centrifuge tube, prepare 0.01 M NaBH4 in cold water. (final volume: 40 mL, MW: 37.83 g)
Vortex. Keep on ice.
In two 50 mL centrifuge tubes, prepare 0.1 M CTAB in water from 0.2 M CTAB stock solution (step 1). (final volume: 40 mL per tube).
In secondary containment, sonicate until dissolved.

Seed solution (1) To a glass vial, add magnetic stir bar.
(2) Place vial on stir plate and turn on stir plate.
(3) Add 5 mL of 0.2 M CTAB stock solution.
(4) Add 5 mL of 0.00050 M $HAuCl_4$ stock solution.
(5) Add 0.60 mL of 0.010 M $NaBH_4$ stock solution.
(6) Stir 2 minutes.

Gold nanorods

(1) To a glass vial, add 9.5 mL 0.1 M CTAB stock solution.
(2) Add between 55 - 65 μL 0.01 M $AgNO_3$ stock solution.
(3) Add 0.5 mL 0.01 M $HAuCl_4$ stock solution.
(4) Add 55 μL 0.1 M ascorbic acid stock solution.
(5) Add 12 μL seed solution.
(6) Age solution for 24 - 48 hours at room temperature.

Appendix C

DNA conjugation

This procedure for the conjugation of thiolated DNA to gold nanoparticles makes a reaction suitable for separation by HPLC.

Concentration of gold nanoparticles

1. To 100 ml of Au nanoparticle solution (citrated stabilized from synthesis or Ted Pella) in a screw-top bottle add 50 mg of BSPP. Stir vigorously overnight.

2. Spin down the nanoparticles by centrifugation. For particles larger than 10nm, spin down in 50mL Falcon tubes at 9000rpm for 10 minutes or until the supernatant is clear. [For 13-20nm particles, it may be necessary to divide the solution into 1.5mL Eppe tubes and spin at 14000rpm.] Remove the supernatant to resuspend pellets in (ideally) .5-1mL final volume.

3. For smaller particles, add NaCl .5g at a time until the particles form aggregates. Spin in 50mL Falcon tubes at 4000rpm for 10 minutes. Resuspend pellet in 1mg/mL BSPP to a final volume of .5-1mL.

Conjugation of DNA to gold nanoparticles

1. (Optional) Reduce trithiolated ssDNAs by reacting them with TCEP beads for 30 min. Remove DNA from beads by centrifugation.

2. DNA stock concentrations are 100μM. Add DNA to 80μL of nanoparticles stoichiometrially. Nanoparticle concentrations can be determined by optical density at 520nm while DNA concentration can be determined by optical density at 260nm. Stoichiometry of DNA to is length, particle size, and sequence dependent and must be determined

experimentally. For small particles, 2:1 or 1:1 DNA:nanoparticles is a good starting point, 5:1 for 20nm particles, and 10:1 for larger particles.

3. If DNA has not been previously reduced, add 1/10 volume 1mg/mL BSPP. Adjust the solution to 30 mM NaCl concentration by adding appropriate amounts of .5M NaCl solution. Avoid direct addition which causes aggregation. Place NaCl solution drops to the e-tube wall and vortex.

4. React overnight.

5. Add 1/20 volume of 50mM HS-(OCH2CH2)6-COOH to each nanoparticle solution.

6. After 1hr, add NaCl solution to a concentration of 60 mM. React 30 minutes more and add NaCl solution again to the final concentration of 100 mM.

7. React for additional 30 min.

8. Filter through 2 micron PFTE syringe filter before separating by HPLC.

Appendix D

DNA sequences

DNA was purchased from Fidelity Systems, Inc with a 5′ Letsinger trithiol modification. In general, oligonucleotides were ordered at 1 μmol with PAGE purification. Pellets were resuspended in Tris-EDTA (10mM Tris, .5mM EDTA) to a final concentration of 100μM.

D.1 Nanorod dimer sequences

The first two sequences are fully complementary.

63 bp full hybridization

5′ - CCG GGC GCG GAC AGA TCA CTG CTA CAC TGA GAG TCT CTC CAG CTC ATG CAC ACG GGC CGC CGG - 3′

63 bp complement

5′ - CCG GCG GCC CGT GTG CAT GAG CTG GAG AGA CTC TCA GTG TAG CAG TGA TCT GTC CGC GCC CGG - 3′

The sequences below are all 60 bp long. They have 10, 20, and 30 bp of complementarity.

10 bp overlap

5′ - GCG ATA TCG GCC TTT ACC TAC CTC ACC CTC ATC CCT ACC ACT CAC CAT CCA TCA CTC CCA - 3′

10 bp complement

5′ - CCG ATA TCG CAA CTT CAA CTC TAC CAT CCT CAC CCT ACT CCC ACT CAC CTA CCT CAC CCC - 3′

20 bp overlap

5′ - CCT CAC ATC CAT CCT TAC TAC CCT CAC CCT ACT TTA CTC ACG GTA CAG ATA TCC TGA ACG - 3′

20 bp complement

5′ - ACT TCC ACT TAC TCA CTT TAC CTC CAC TTT ACT TTA CTT ACG TTC AGG ATA TCT GTA CCG - 3′

30bp overlap

5′ - GCG TCT AAC GAC GAT ATC GCG TTC AGA CGC TCC TAC TTT ACC ATC CCA CTC AAT CCA CTC - 3′

30 bp complement

5′ - GCG TCT GAA CGC GAT ATC GTC GTT AGA CGC TCC ATC CCT ACT TAA CTC CAC TCA CCT CAC - 3′

D.2 Pyramid sequences

These sequences are complementary to approximately one third of each other sequence. Stand 1 and 4 form the short side of the pyramid.

Strand 1

5′ - TTT GCC TGG C ATT ACG GC TTTC CCT ATT AGA AGG TCT CAG GTG CGC GTT TCG GTA AGT AGA CGG GAC CAG TTC GCC - 3′

Strand 2

5′ - TTT CGC GCA CCT GAG ACC TTC TAA TAG GGT TTG CGA CAG TCG TTC AAC TAG AAT GCC CTT TGG GCT GTT CCG GGT GTG GCT CGT CGG - 3′

Strand 3

5′ - TTT GGC CGA GGA CTC CTG CTC CGC TGC GGT TTG GCG AAC TGG TCC CGT CTA CTT ACC GTT TCC GAC GAG CCA CAC CCG GAA CAG CCC - 3′

Strand 4

5′ - TTT GCC GTA ATG C CAG GCT TTC CGC AGC GGA GCA GGA GTC CTC GGC CTT TGG GCA TTC TAG TTG AAC GAC TGT CGC - 3′

D.3 Graphene liquid cell sequences

42 bp sequence

5′ - CCG GCG GCC CAC CAC ATC CTC TCA AGT GAC CAC CGC GCC CGG - 3′

42 bp complement

5′ - CCG GGC GCG GTG GTC ACT TGA GAG GAT GTG GTG GGC CGC CGG - 3′

84 bp sequence

5′ - CCG GCG GCC CAG GTG TAT CAG TGT TCG TTG CAA GCT CCA ACA TCT GAG TAC CAC GCA TAC TAT ACT TGA AAT ATC CGC GCC CGG - 3′

84 bp complement

5′ - CCG GGC GCG GAT ATT TCA AGT ATA GTA TGC GTG GTA CTC AGA TGT TGG AGC TTG CAA CGA ACA CTG ATA CAC CTG GGC CGC CGG - 3′

D.4 IPET sequences

84 bp sequence

5′ - CCG GCG GCC CAG GTG TAT CAG TGT TCG TTG CAA GCT CCA ACA TCT GAG TAC CAC GCA TAC TAT ACT TGA AAT ATC CGC GCC CGG - 3′

84 bp complement

5′ - CCG GGC GCG GAT ATT TCA AGT ATA GTA TGC GTG GTA CTC AGA TGT TGG AGC TTG CAA CGA ACA CTG ATA CAC CTG GGC CGC CGG - 3′